Structural and electronic characterization of hetero-organic NTCDA-CuPc adsorbate systems on Ag(111)

Sonja Schröder

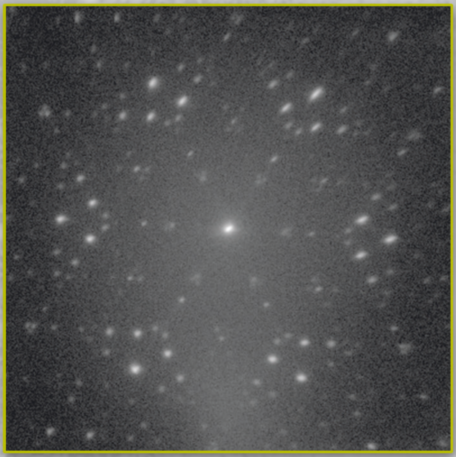

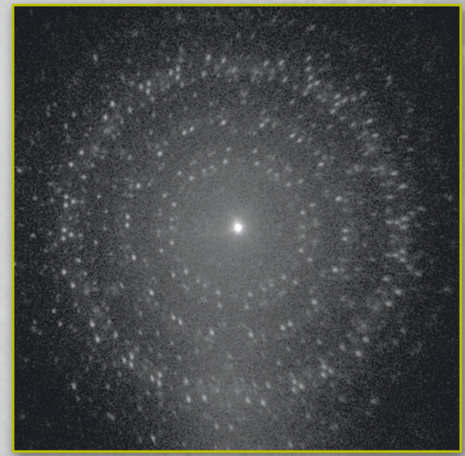

Schlüsseltechnologien /
Key Technologies
Band / Volume 144
ISBN 978-3-95806-239-9

JÜLICH
FORSCHUNGSZENTRUM

Schriften des Forschungszentrums Jülich
Reihe Schlüsseltechnologien / Key Technologies Band / Volume 144

Forschungszentrum Jülich GmbH
Peter Grünberg Institut (PGI)
Functional Nanostructures at Surfaces (PGI-3)

Structural and electronic characterization of hetero-organic NTCDA-CuPc adsorbate systems on Ag(111)

Sonja Schröder

Schriften des Forschungszentrums Jülich
Reihe Schlüsseltechnologien / Key Technologies Band / Volume 144

ISSN 1866-1807 ISBN 978-3-95806-239-9

Bibliographic information published by the Deutsche Nationalbibliothek.
The Deutsche Nationalbibliothek lists this publication in the Deutsche Nationalbibliografie; detailed bibliographic data are available in the Internet at http://dnb.d-nb.de.

Publisher and Distributor: Forschungszentrum Jülich GmbH
Zentralbibliothek
52425 Jülich
Tel: +49 2461 61-5368
Fax: +49 2461 61-6103
Email: zb-publikation@fz-juelich.de
www.fz-juelich.de/zb

Cover Design: Grafische Medien, Forschungszentrum Jülich GmbH

Printer: Grafische Medien, Forschungszentrum Jülich GmbH

Schriften des Forschungszentrums Jülich
Reihe Schlüsseltechnologien / Key Technologies, Band / Volume 144

D 82 (Diss. RWTH Aachen University, 2015)

ISSN 1866-1807
ISBN 978-3-95806-239-9

Contents

1. Introduction

Ching Tang and Steven van Slyke invented the first organic light emitting diode (OLED) in 1987 after they discovered that light can be emitted by passing current through a carbon-based material [TV87]. Since then organic molecules have been used additionally in organic field transistors (OFETs) [KTA03] and photovoltaic cells (OPVC) [YSF05]. Organic solar cells are very promising as they have many advantages compared to inorganic devices: 10 times thinner active layers are sufficient, the costs are much less and the production is easier. To compete with inorganic solar cells however the efficiency of the organic solar cells has to be increased by a factor of 2-3 [Kie07]. For further development and an increase of the efficiency of these devices, different materials have been studied as small organic molecules and polymers. This should lead to deeper knowledge of fundamental mechanisms at organic-metal and organic-organic interfaces, in order to find the material of choice. Many different homomolecular prototype systems of semiconducting molecules on metals have therefore been investigated extensively in the last decade [Tau07], [For97], [EBST04], [BLC$^+$10], [SHK$^+$09], [KSS$^+$10], [DGS$^+$07]. Studying the formation of the first layer is necessary as it is crucial for the growth of the subsequent layers [BCK05], in the end defining the properties of the organic device.

Recently, heteromolecular thin films have moved into the focus of interest, as in particular the understanding of acceptor-donor interfaces, where the photo-generation of charges occurs, is the main requirement for efficient two-layer organic devices. An organic electron acceptor is characterized by its ability to take up electrons in its lowest unoccupied molecular orbital (LUMO), in contrast to a donor where electrons are released from the highest occupied molecular orbital (HOMO), which creates an electron hole. In the case of planar π-conjugated molecules as they are subject of this work, and in contrast to inorganic devices the charge transfer of the positive (holes) and negative (electrons) charge carriers occurs preferably in the vertical direction of the delocalized π-electron system by hopping processes between the molecules. The charge transport depends strongly on the arrangement of the molecules to each other, as in well ordered molecular structures a higher charge mobility is reached than in amorphous solids [Kie07]. It is thus very important to investigate differently ordered heteromolecular systems of laterally or stacked mixed layers, consisting of two types of molecules, one acting as an electron acceptor and the other as an electron donor. In this work both kinds of mixed systems were investigated to study the influence of the structure formation on the electronic properties.

Firstly, the lateral mixing of different molecules within one monolayer on nobel substrates is discussed which allows for the tuning of the size and shape of these unit cells by using different molecular ratios [HCL$^+$10], [SHS$^+$15], [GMES$^+$14]. Surfaces of nobel metals with a (111) orientation are highly interesting as the interaction between the adsorbed molecules and the substrate and the intermolecular interactions are similarly strong. The interplay of both interactions determines therefore the structure formation and leads to very complex phase diagrams [SHS$^+$15]. Whether molecules mix with each other or stay separated on the substrate provides therefore information about the interaction strength between the substrate and the molecules and the intermolecular interaction [SLW$^+$14]. For example the fullerene C_{60} and copper-II-phthalocyanine (CuPc) on Au(111) [SWG$^+$01] form only phase separated structures, in contrast to CuPc and 3,4,9,10-perylene-tetra-carboxylic-dianhydride (PTCDA) on Cu(111) [BWBM03] and Ag(111) [SHS$^+$15], where well ordered mixed structure appear. It seems thus to be likely that the stronger molecules-substrate interaction on copper and silver compared to gold causes the differently arranged structures.

A more direct way to reveal the molecule-substrate interaction strength is to study the vertical structure, in particular the bonding height of the molecules above the surface [SGP$^+$14], as it is known from chemistry that smaller bond lengths go along with a stronger bonding. For molecules adsorbed on metal surfaces, the molecular binding strength is reflected by a down-shift of the former lowest occupied orbital (LUMO) in energy. This happens as charge is transferred to the molecules upon adsorption on the surface, consequently leading to a partially filling of the former LUMO, which can be interpreted as a weak chemisorption of the molecules [GSS$^+$05]. This charge transfer reduces the charge spill out of the substrate underneath the molecules (so called push back effect) and hence allows for a closer approach of the molecules to the surface (reduced adsorption height).

Stadtmüller et al. studied the lateral mixing of the charge acceptor PTCDA and the weak charge acceptor CuPc, which turns into a charge donor upon mixing of both molecules on Ag(111). From literature it is known that PTCDA has a lower adsorption height than CuPc in their homolecular structures [KSS$^+$10], [HKC$^+$05]. Stadtmüller et al. observed that the adsorption height of the PTCDA molecules increased and the adsorption height of CuPc was lowered upon mixing, leading to an alignment of both molecules at the same adsorption height. Although both molecules adsorb at the same adsorption height, the LUMO of PTCDA is completely filled in contrast to the LUMO of CuPc which is depopulated. This indicates the unexpected finding that the bonding distance of the molecules to the substrate in these heteromolecular structures is "decoupled" from the binding strength, as reflected by the binding energies of the LUMOs. It can be explained by the assumption that charge is transferred from the CuPcs via the substrate to the PTCDA molecules. The increased (lowered) charge spill out underneath the PTCDA (CuPc) molecules leads to the alignment of the molecules [SLW$^+$14].

It should be mentioned that a contrary result was observed by Goiri et al. [GMES$^+$14] for a similar heteromolecular structure of CuPc with perfluoropentacene (PFP), where no adsorption height alignment, but a separation of the molecules observed. But also here, the adsorption height of the acceptor (donor) increases (decreases) upon mixing. The separation of the molecules is a consequence of a higher adsorption height of the donor compared to the acceptor in the homomolecular phase (in contrast to the CuPc + PTCDA phase). Consequently it is not contradicting to Stadtmüller et al., as it shows the same trend for the acceptor and donor molecules and indicates that the fluorination of the acceptor is the reason for the different behaviour.

The results of the PTCDA-CuPc heterostructures are the basis for the present work. The acceptor PTCDA was exchanged by the weaker electron acceptor 1,4,5,8-naphthalene-tetracarboxylic-dianhydride (NTCDA). It should be determined whether NTCDA is also able to accept the charge donated by the CuPcs or the CuPcs have to accept the residual charge which consequently leads to a partially filled LUMO. The lateral structure was investigated for different molecular ratios of CuPc and NTCDA, as this provides information how the geometric structure influences the vertical and electronic properties. The vertical structure determined by the X-ray standing waves technique revealed an adsorption height alignment between NTCDA and CuPc for two mixed phases, but at different heights for the different NTCDA + CuPc phases. The investigation of the electronic properties by AR(UPS) proved that the weak charge accepter NTCDA is able to accept the whole charge donated by the CuPc molecules. The related adsorption heights of NTCDA and CuPc in combination with the corresponding filling of the former LUMO confirms the general model of charge reorganisation at metal-organic interfaces and the relation between bonding distance and binding strength determined by Stadtmüller et al.

Secondly, we have studied the structure formation in stacked acceptor-donor systems, as only little is known about the interaction of organic-organic interfaces [SPL+99], [HGS+10],[SWS+15]. Stadtmüller et al. studied bilayer systems of PTCDA and CuPc on Ag(111). They observed that CuPc on top of PTCDA forms a commensurate superstructure [SSK+12]. In addition, the adsorption heights of both molecules indicate that the interaction between the organic layers is dominated by electrostatic and van der Waals forces. The adsorption height of PTCDA decreases upon CuPc adsorption, leading to an enhanced charge transfer into the PTCDA molecules [SWS+15]. For the bilayer system of the non-planar tin phthalocyanin (SnPc) / PTCDA on Ag(111) a noncovalent interaction between the organic layers was found as well [HGS+10].

For the inverse stacked system of PTCDA/CuPc/Ag(111), a molecular exchange between heteromolecular layers was observed [SGP+14]. PTCDA molecules diffuse into the CuPc monolayer and replace CuPc molecules by pushing them in the second layer. The PTCDA and remaining CuPc molecules arrange in the following in randomly arranged structures in the first layer. Nevertheless an adsorption height alignment between the molecules in the first layer occurs which is connected to a charge reorganization as explained above. The residual molecules form ordered PTCDA and disordered CuPc islands in the second layer.

In addition to the characterization of the bilayer systems, their desorption behaviour upon annealing is interesting to study. This is based on earlier findings that CuPc molecules in the second layer on top of a PTCDA layer enable a desorption of PTCDA molecules from the first organic layer at elevated temperatures, which is not possible for the homomolecular structure of PTCDA on Ag(111) [Sta13]. Obviously, the energy barrier for the desorption of PTCDA molecules is in this case split into two steps: (1)

molecular exchange of PTCDA and CuPc and (2) the desorption of PTCDA from the second layer.
In the present work PTCDA was exchanged by NTCDA to study whether the molecules in the second layer arrange in well ordered structures or even exchange with the molecules in the first layer, as it was earlier observed for stacked PTCDA-CuPc systems on Ag(111). A further point in our investigation was to study the interaction strength between the NTCDA-CuPc layers and whether the molecules in the second layer influence the charge transfer from the substrate into the first organic layer. It was found that molecular exchange occurs between the layers of a loosely packed relaxed monolayer of NTCDA with CuPc on top. This is hindered in the more densely packed compressed monolayer of NTCDA with CuPc in the second layer. In this case the CuPc molecules align their wings along the high symmetry directions of the substrate, although they form on pristine Ag(111) only a disordered phase [KSS+10]. Annealing causes a molecular exchange and activates the formation of well ordered laterally mixed heterostructures. For the inverse system of a monolayer of CuPc with NTCDA in the second layer, the long-range order of the CuPc layer disappears at RT. After annealing the ordered structure of the CuPc monolayer reappeared, as only the NTCDA molecules desorbed.

We combined many different experimental techniques in order to gain this complex information about the adsorption geometry and the corresponding electronic properties of the organic-metal interface. In the second chapter a short introduction to all applied experimental methods is given. Additionally, the sample preparation and the data processing for some methods is described.

The earlier results about the lateral and vertical geometry of the homomolecular structures of NTCDA on Ag(111) are summarized in the third chapter [KSK+08], [SKZ+10], [SHS+07]. New results about the electronic properties of the relaxed and compressed monolayer of NTCDA recorded by angle-resolved photoelectron spectroscopy are discussed, as they act as a precondition for the investigation of the mixed NTCDA-CuPc systems.

Laterally mixed molecular systems are of interest in the fourth chapter. In the first part a summary of the already mentioned reference system CuPc and PTCDA on Ag(111) is given [Sta13]. In the following the lateral and vertical structures and their related electronic properties of mixed NTCDA-CuPc phases at different coverages on Ag(111) are presented.

In chapter five three differently stacked systems of NTCDA and CuPc were investigated on Ag(111). The molecular order was determined by low energy electron diffraction (LEED) and corresponding electronic properties by UPS and ARPES.

2. Experimental techniques

Various experimental methods have been used in this work for studying the lateral and vertical geometry of organic adsorbates on metal substrates. The lateral structure was analysed by (SPA)-LEED and scanning tunnelling microscopy (STM). The vertical adsorption geometry was determined by the X-ray standing waves technique. In addition the electronic structure has been investigated by ultraviolet photoelectron spectroscopy (UPS), angle resolved UPS (ARPES) and scanning tunnelling spectroscopy (STS). The physical principles of these methods are well established and within this work technical improvements have not been developed, therefore only the basic principles of all methods are summarized. At the beginning of the chapter the sample preparation of the homomolecular and hetero-organic monolayers will be described.

2.1. Sample preparation

2.1.1. Cleaning of Ag(111) crystal

The Ag(111) crystal was sputtered and annealed after each measurement at least two times. For sputtering Argon ions were accelerated to 0.5 keV towards the sample with an incident angle of ± 55°, each angle for 20 min, with a sample current of $I_{sample} = 4\mu$A. Subsequently the crystal was annealed to 725 K for around 30 minutes.

2.1.2. Deposition of organic monolayers

Monolayers of NTCDA and CuPc on Ag(111)

The preparation of all monolayer structures of NTCDA and CuPc on Ag(111) starts with the deposition of a NTCDA or a CuPc multilayer on the clean crystal. The multilayer of NTCDA (CuPc) can be easily transformed into a compressed monolayer of NTCDA (monolayer of CuPc) by annealing to 360 K (555 K). The amount of deposited molecules can be either determined by recording the diffraction pattern with SPA-LEED or by monitoring the ion current of different molecular fragments with a quadropole mass spectrometer (QMS) during deposition. As the LEED patterns of the relaxed and compressed monolyer of NTCDA (CuPc monolayer) are well known and can easily distinguished, the coverage can be determined precisely. In addition the ion current of NTCDA with 74 amu and 124 amu (CuPc with 62 and 128 amu) can be recorded for identifying the exact amount of deposited molecules. Furthermore a mass close to the molecule fragments was always displayed as a background signal and was subtracted from the molecular signal. The integration of the QMS signal over the deposition time represents a measure for the deposited amount of molecules. Higher heating to 390 K leads to the desorption of further NTCDA molecules and the rearrangement of the remained molecules to the structure of the relaxed monolayer.

Lateral mixed films on Ag(111)

The two molecules NTCDA and CuPc were deposited after each other while the amount of deposited molecules was determined by recording the ion current of different molecular fragments with a quadropole mass spectrometer (QMS). At the SPA-LEED chamber, the evaporator configuration allowed for the deposition of the molecules while SPA-LEED scans are recorded. This enabled us to track the change of the diffraction pattern in real time in dependence on the coverage and therefore to determine phase changes immediately. The molecules were deposited with a constant deposition rate of ≈ 0.1 ML/min. Different coverage ratios of both molecules were deposited in several experiments, but with a total coverage of up to one complete monolayer.

In contrast, at the STM chamber the success of the preparation was only verified after deposition by a conventional LEED and by STM. The LEED instrument at the STM chamber offered us as well the opportunity to assign the observed STM diffraction pattern to structures known from the SPA-LEED chamber. The samples at the XSW chamber at the beamline I09 at Didcot were identically prepared as at the STM chamber, but the diffraction patterns were recorded with a MCP LEED.

At the chamber at the Bessy II, where we performed ARPES experiments, the amount of deposited molecules was determined with a quartz crystal microbalance (QCM). The resonance frequency of the quartz crystal changes by the addition of small masses, which allows for a precise determination of the deposited molecules. The lateral structure of the phases was confirmed with a MCP LEED.

2.2. Low energy electron diffraction (LEED)

For any system knowledge of the geometric structure of its surface is paramount for the understanding of its physical and chemical properties. Low energy electron diffraction (LEED) is one of the most common methods to determine this relevant information. Monochromatic electrons are accelerated onto a sample under normal incidence and are diffracted by the first few layers of the sample. The elastically scattered electrons are detected by a fluorescent screen where the diffraction pattern becomes visible, while the inelastically scattered electrons are blocked by a grid system.

The surface sensitivity of this method is caused by the low kinetic energy of the electrons; between 20 to 500 eV, leading to a mean free path of less than 10 Å, which corresponds to 2-3 monolayers. The electron wavelength λ is on the order of inter atomic

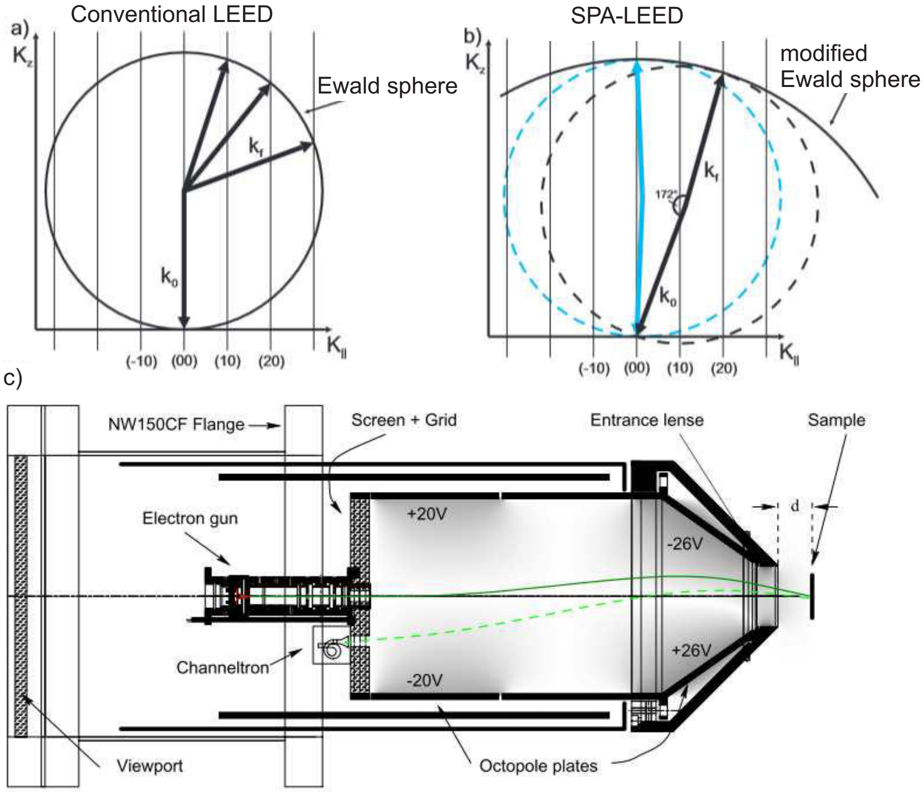

Figure 2.1.: Ewalds sphere for the visualization of the 2D scattering condition in (a) a conventional LEED and in (b) a SPA-LEED [Kle13]. (c) Horizontal cut through a SPA-LEED instrument from Omicron with a conical shape. The main parts are signed and the path of the electron beam is indicated in green [HvH99].

distances (0.6-2.7 Å) and the arrangement of the surface unit cell can thus be quantified [vHWC86], [HvH99].

The diffraction pattern can be explained based on kinematic and dynamic diffraction theory. In the simpler kinematic approximation, the electrons are scattered only once in contrast to dynamic theory which considers multiple scattering events. For the determination of the positions of the diffraction spots in reciprocal space the geometrical diffraction theory is however sufficient. In the case of scattering on a 3-dimensional crystal diffraction spots can only occur at discrete points of the reciprocal lattice G related to the Laue condition. In contrast at a single atomic layer the so-called Ewalds rods arranged perpendicular to the surface are relevant due to the missing periodicity in the direction perpendicular to the sample. The translation vectors $\vec{a_i}^*$ of the 2D reciprocal lattice are directly connected to the lattice parameters in real space $\vec{a_i}$ by the equation $\vec{a_i} \cdot \vec{a_j}^* = 2\pi\delta_{ij}$ [vHWC86]. The condition for the presence of diffraction spots can be visualized in the Ewald construction, as shown for a conventional LEED in Fig. 2.1 (a). The wave vector $\vec{k_0}$ of the incident beam points to the (0,0) point located on the Ewald sphere with the radius $|\vec{k}|$, which is defined by the electron energy. The scattering condition $\vec{K}_{||} = \vec{k}_{f||} - \vec{k}_{0||} = \vec{G}_{||}$ for the vector components parallel to the surface is fulfilled for each vector $\vec{k_f}$ which crosses the Ewald sphere at a lattice rod.

The intensity of the Ewald rods is in reality modulated due to the penetration depth of slow electrons, which is with 2-3 atomic layers between the aforementioned cases of a single atomic layer and a bulk material. This allows for the investigation of additional properties, for example the adsorption height and the exact position of each scatterer inside the surface unit cell, which can be accessed by LEED-IV [BRdAHK04]. The intensity distribution of the spots of the LEED pattern is recorded in dependence on the energy of the electrons. Comparison of the recorded intensity profile with curves based on calculations, which include dynamic scattering, leads to the precise determination of the atomic positions.

SPA-LEED

A spot profile analysis LEED has several advantages over a conventional LEED instrument, which will be explained in the following together with the instrumental set-up. A horizontal cut through a SPA-LEED instrument is shown in 2.1 (c), which consists mainly of a fine focus electron gun, octopole deflection plates, an entrance lens and a single electron detector (channeltron). The LEED pattern can not be obtained by one shoot as for a conventional LEED due to the zero-dimensional detector. The diffraction patterns are therefore recorded by scanning the reciprocal space. For this purpose the angle of the incoming beams to the surface is varied by the octopole plates and only the electrons which pass almost the same way as the incoming electrons can be detected by the channeltron. The incoming and reflected beam include therefore a constant angle of 7°. In the Ewald construction this leads to a turning of the entire Ewald sphere, its enfold is called "modified Ewald" sphere, as shown in 2.1 (b), which has twice the radius of a conventional Ewald sphere.

A further advantage of SPA-LEED is the high sensitivity of the channeltron detector, which allows for measurements with low beam intensities of only 0.1-10 nA, reducing beam damage to the organic layers. Additionally, the coherent transfer width $T_c = \lambda * \frac{R}{b}$ determines the resolution Δk, as this is given by $\Delta k \approx \frac{2\pi}{T_c} = \frac{2\pi b}{\lambda R}$. b is the radius of the detector aperture and R the distance between sample and detector. The high resolution of the SPA-LEED is thus obtained by a small aperture (LEED $\approx$ 0.5 mm and SPA-LEED $\approx$ 0.2 mm) in front of the detector and a large sample-detector distance (LEED $\approx$ 75 mm and SPA-LEED $\approx$ 300 mm) [Sta09],[Hen82]. The SPA-LEED instrument used within this work has a resolution of Δk = 0.01 Å^{-1}.

Superstructure matrix

The periodic order of surfaces, in particular the size and shape of the unit cell can be obtained by LEED. The SPA-LEED scans are however originality scaled by units of the deflection voltage. For the study of the surface unit cell, a scaling factor for a conversion of the voltage into k-values has to be determined by normalizing them using the diffraction pattern of a well-known commensurate structure, for example a monolayer of PTCDA [KUS04] or the relaxed monolayer of NTCDA [SGS$^+$98] on Ag(111) at different electron energies. This LEED pattern can be simulated by Spot-Plotter [Bay08] and the scaling factor is changed until the simulated and the measured diffraction pattern are identical. Based on the calibrated images, the superstructure of the organic adsorbates with the reciprocal basis vectors $\vec{b_i}$ can then be expressed by the matrix **M** and the basis vectors of the surface unit cell $\vec{a_i}$ of the substrate:

$$\begin{pmatrix} b_1 \\ b_2 \end{pmatrix} = \mathbf{M} * \begin{pmatrix} a_1 \\ a_2 \end{pmatrix} = \begin{pmatrix} m_{11} & m_{12} \\ m_{21} & m_{22} \end{pmatrix} * \begin{pmatrix} a_1 \\ a_2 \end{pmatrix} \tag{2.1}$$

To determine the molecule-substrate relation, the elements of the matrix **M** are changed until the simulated diffraction pattern fits the LEED image.

2.3. Photoemission spectroscopy

Photoemission spectroscopy is a well established method for investigating the electronic properties of molecules, solids and surfaces. It is based on the photoelectric effect found by Hertz [Her87] and by Hallwachs [Hal88], and explained in 1905 by Einstein [Ein05].

During photoemission photons with energy $\hbar\omega$ are absorbed by the sample and excite electrons from the initial state i with a wave function Ψ_i to a final state f above the vacuum level with a wave function Ψ_f, as shown in Fig. 2.2 (a) and (b). The photoelectrons are therefore emitted from the sample. The kinetic energy of the photoelectrons is recorded by an electron analyser. Depending on the photon energy the method is called UPS (ultraviolet PES) or XPS (X-ray PES), where either valance band or core-level states are analysed.

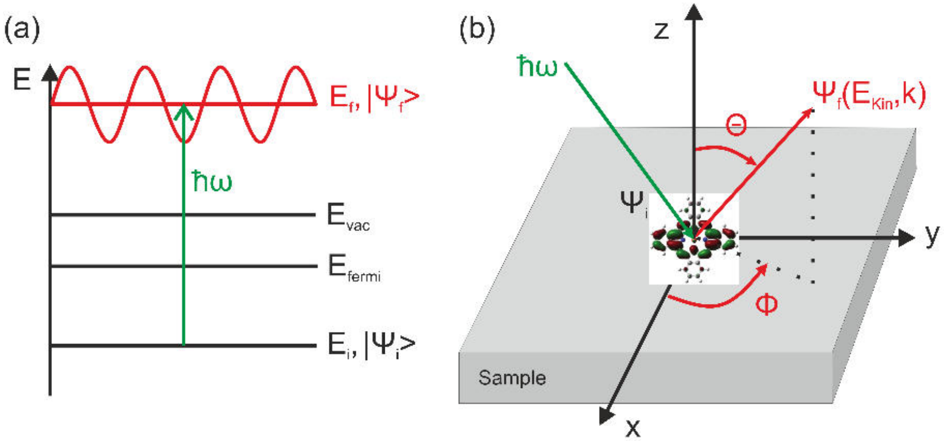

Figure 2.2.: (a) Schematic diagram of the positions in energy of the initial state E_i, the final state E_f, the vacuum level E_{vac} and the Fermi level E_F. (b) In a photoemission experiment an electron in the initial state Ψ_i becomes excited by a photon with the energy $\hbar\omega$ into the final state Ψ_f. Conventionally only the polar angle Θ is recorded, but in an angle resolved measurement the sample is rotated and the dependency of the electron intensity on the azimuthal angle Φ is also considered (related to [PKDR13]).

In the sudden approximation the photoemission process is described in an one-step model where the excited electron leaves the sample immediately and therefore does not undergo an energy loss by scattering with other electrons, phonons or impurities [Alm06]. The photoelectron intensity $I(\Theta, \phi, E_{kin})$ is given by a sum over all transitions from occupied states i to the final state f by the formula of Fermi‘s Golden rule [PKDR13]:

$$I(\Theta, \phi, E_{kin}) = \sum_i |\langle \Psi_f(\Theta, \phi, E_{kin})|\boldsymbol{A} * \boldsymbol{p}|\Psi_i(\Theta, \phi, E_{kin})\rangle|^2 \times \delta(E_F - E_i - \hbar\omega) \quad (2.2)$$

Here, Θ and ϕ reflect the polar and azimuthal angles of the emitted electrons, as shown in Fig. 2.2 (b). The transition matrix element is given by the momentum operator $\boldsymbol{p}$ and the vector potential $\boldsymbol{A}$ of the incident electro-magnetic wave in the dipole approximation. The energy conversation of the photo-exciting process is included by the δ function.

For the calculation and simplification of the transition matrix, it can be assumed that the initial state wave function can be expressed by a product of the orbital Φ_k (k=quantum number) from which a photoelectron can be excited and the wave function of the remaining (R) electrons $\Psi^k_{i,R}(N-1)$. In analogy the final state can be written as the product of the wave function of the emitted electron $\Phi_{f,kin}$ and the wave function of the electron system $\Psi^k_{f,R}(N-1)$. This leads to a simplified matrix element

$$\langle \Psi_f|\boldsymbol{A} * \boldsymbol{p}|\Psi_i\rangle = \langle \Phi_{f,E_{kin}}|\boldsymbol{A} * \boldsymbol{p}|\Phi_{i,k}\rangle \langle \Psi^k_{f,R}(N-1)|\Psi^k_{i,R}(N-1)\rangle \quad (2.3)$$

which consists of a one-electron matrix and an (N-1) overlap integral. In the frozen-orbital approximation it is assumed that the remaining orbitals are identical in the initial and final state which means that $\Psi^k_{f,R}(N-1) = \Psi^k_{i,R}(N-1)$. The overlap integral is therefore unity and the transition matrix simply consists of the one-electron matrix element [Hö3]. The argument of the delta function vanishes in this case if this condition is fulfilled:

$$E_{kin} = \hbar\omega - E_b - \Phi \tag{2.4}$$

where the work function of the sample Φ has to be included for photoemission from metal substrates. This simplified model does not hold for orbitals of molecules on metal surfaces, as the remaining N-1 charges can immediately relax to optimise the energy gain. The binding energies of the molecular orbitals can therefore differ due to screening effects of the environment.

In this work the valence band structure of organic adsorbates on Ag(111) at room temperature was determined by UPS, performed at the BESSY II storage ring in Berlin at beamline U125/2 SGM. The same beamline was used for ARPES and orbital tomography experiments. The samples were illuminated under an incident angle of 40° and the photoelectrons were recorded with a toroidal electron analyser with an acceptance angle of ±80°. The monolayers of NTCDA and CuPc and the CuPc-rich phase were recorded at a photon energy of 35 eV. In contrast, the NTCDA-rich and the annealed intermediate phase were investigated at a photon energy of 30 eV. The pass energy was 10 eV for all measurements.

The frontier orbitals of the molecules at low temperatures were investigated at the Diamond light source in Oxford at beamline I09 in context with the XSW experiments. The measurements were performed with a monochromatized UV-light source which provides photons with an energy of 21.2 eV. The kinetic energy distribution was recorded with a hemispherical electron analyser (VG Scienta R4000). The pass energy was 10 eV with an energy resolution of 10 meV. The energy scale was zeroed to the Fermi level E_F for all spectra.

Angle-resolved UPS and orbital tomography

Angle-resolved UPS allows for the additional determination of the angular momentum of the photoelectrons by rotating the sample in the direction of the azimuthal angle ϕ, see Fig. 2.2. This is based on the channel plates which enable an angle-resoled detection of the photoelectrons. We want to fit the molecular orbitals in momentum space to the intensity resolved in the energy regime of the PES resonance of interest.

The molecular contribution to each orbital can be therefore obtained by a least square fitting routine, called orbital tomography. The photoemisson intensity described by formula 2.2 can be simplified by treating the final state as a plane wave. The photoemission intensity Ψ_i is in this case proportional to the square modulus of the Fourier transform of the initial state wave function:

$$I(\Theta, \phi, E_{kin}) \propto |\tilde{\Psi}_i(k)|^2 * |\boldsymbol{Ak}|^2 \tag{2.5}$$

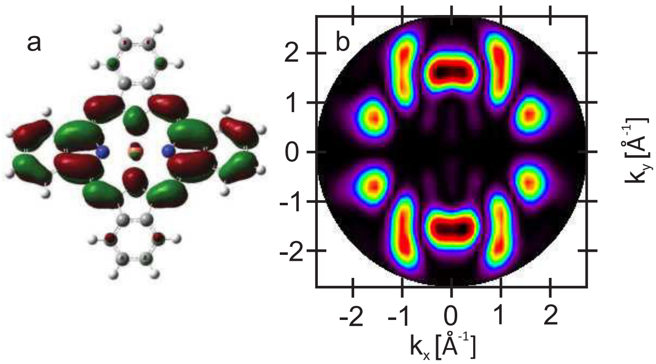

Figure 2.3.: (a) Wave function of the LUMO for a free CuPc molecule (DFT calculation B3LYP: Basis set LANL2DZ). (b) Calculated momentum map $\Phi(k_x, k_y)$ of the CuPc LUMO.

The plane-wave approximation is a good assumption when (1) π orbital emission from large planar molecules is given, (2) the angle between polarization vector $\vec{A}$ and the emitted electron is small and (3) the molecules contain light atoms [PKDR13]. This approximation was applied successfully for describing the photoemission intensity of many organic molecules on metals [PKDR13], [SWR+12] and [WSS+13].

In this work, the photoelectron yield was recorded with a toroidal analyser with an acceptance angle of ±80° at Bessy II. To record a 3D data cube $I(\Theta, \phi, E_B)$ for the whole (k_x, k_y) range, the sample was rotated around its surface normal in 1° steps in a range of at least 120°. A data cube was obtained for the energy region of each resonance observed in the UPS spectrum. The emission data depending on the azimuthal (ϕ) and polar (Θ) angles were converted to parallel momentum maps k_x and k_y by [PRU+11]:

$$k_x = \sqrt{2\mathrm{m}_e E_{kin}/\hbar^2}\,\sin\Theta cos\phi \tag{2.6}$$

$$k_y = \sqrt{2\mathrm{m}_e E_{kin}/\hbar^2}\,\sin\Theta sin\phi \tag{2.7}$$

Each data cube has an energy width of 1.0 eV at a pass energy of 10 eV and consists of 40 individual slices. Considering the threefold symmetry of the bulk silver crystal we can symmetrise our recorded 120° data cube to a complete three-dimensional data cube $I(k_x, k_y, E_b)$.

For the application of orbital tomography, theoretical momentum maps $\Phi(k_x, k_y)$ of the corresponding orbitals are necessary for a deconvolution of the orbitals. Therefore first the initial state, the wave function of an orbital for a free molecule, is calculated by density functional theory (DFT), as shown in Fig. 2.3 (a) for example for the LUMO of CuPc. Subsequently the three dimensional Fourier transform into momentum space is formed. As a consequence of the plane wave approximation the momentum distribution of the photoemission intensity of a specific orbital can be obtained from a hemispherical cut through this three dimensional Fourier transform of the molecular wave function at a certain radius k. In Fig. 2.3 (b) the result, the intensity distribution of the theoretical momentum map of the CuPc LUMO, is shown. The comparison of such theoretical maps $\Phi(k_x, k_y)$ for all relevant molecular orbitals with the measured ARPES data cube allows for a direct assignment of the orbitals and a deconvolution for superimposed orbitals by orbital tomography. All theoretical maps $\Phi(k_x, k_y)$ used in this work were calculated by Daniel Lüftner.

Although the plane wave assumption is claimed to be too rough to describe the angle dependent photoemission current properly and should only be valid for large organic molecules, momentum maps of different organic molecules on metal surfaces have been calculated successfully and were in good agreement to the measured ARPES maps [PRU$^+$11], [PKDR13], [SWR$^+$12] and [WSS$^+$13].

Consequently, Stadtmüller [Sta13] established a function similar to Puschnig et al. [PRU$^+$11] for a least square fit of the measured ARPES data cube $I(k_x, k_y, E_b)$:

$$\begin{aligned} I(k_x, k_y, E_B) = \sum_i a_i(E_B)\Phi_i(k_x, k_y) \\ +b(E_B)I_{sub}(k_x, k_y, E_B) + c(E_B) \end{aligned} \tag{2.8}$$

It consists of a linear combination of all calculated momentum maps $\Phi_i(k_x, k_y)$ that may contribute to the ARPES data cube and a summand that includes $k_x - k_y$ slices for each binding energy measured for the clean Ag(111) substrate $I_{sub}(k_x, k_y, E_B)$. It is necessary for a proper fit because of the clear presence of the sp-band features of the substrate in the ARPES data in many measurements. A offset function $c(E_B)$ is also added. The parameters $a_i(E_B)$, $b(E_B)$ and $c(E_B)$ are adjusted during the fitting procedure, which is performed for each binding energy (E_B) separately. This finally results in E_B-dependent coefficients, whereby $a_i(E_B)$ can be understood as the density of states projected onto the molecular orbital i (PDOS). This is valid for all entirely filled orbitals. For partially filled orbitals, e.g. for an former LUMO of chemisorbed molecules on metal surface it has to be considered that $a_i(E_B)$ reflects the occupied density of states and has to be divided by the Fermi distribution to reveal the PDOS. The parameter $b(E_B)$ reflects the contribution of the bare silver substrate to the ARPES data cube.

Two different methods were used to determine the experimental uncertainty of this method by Stadtmüller et al. [SWR$^+$12]. The first approach is based on a Monte Carlo simulation of the statistical error bars of the ARPES count rates, while the second method uses the linear regression of the orbital tomography approach. They determined an uncertainty of 2 % for both methods for the dataset of PTCDA on Ag(111). Since similar settings were used for the fits of the datasets recorded in this work, it can be assumed that the error bars are in the same range.

2.4. X-ray standing wave technique (XSW)

X-ray standing waves is a method based on synchrotron light, to determine the adsorption heights of different chemical species above the substrate surface with an accuracy of less than 0.05 Å. This provides information about the bonding strength between the adsorbate and the substrate. If the measured distance is in the range of the sum of the van der Vaals radii of the species, the atom is physisorbed. In contrast if the measured distance is smaller than the van der Vaals radii, this indicates that the adsorbate [Sta09] is chemisorbed. As the binding character of molecules can be directly accessed by this method it was applied in the last decade to investigate many homomolecular systems on metal substrates [KSS$^+$10], [SHK$^+$09], [GSS$^+$05], but also heteromolecular systems e.g. [GMES$^+$14], [SGP$^+$14], [SLW$^+$14].

A brief introduction of the technique is given based on reviews from Zegenhagen [Zeg93], Woodruff [Woo98] and Batterman [BC64]. The standing wave field is generated in and above the substrate by the interference of an incoming wave with the electric field vector $\mathbf{E_0}$ and a Bragg-reflected wave from the substrate $\mathbf{E_H}$, as long as the Bragg condition

$$\lambda_{Bragg} = 2d_{hkl}\sin(\Theta_{Bragg}) \tag{2.9}$$

is fulfilled.

This is the case within a small photon energy range, since the Bragg reflection has however a certain width called the Darwin width, which is a consequence of dynamic scattering theory [BC64]. The reflectivity curve, which can be measured by scanning the photon energy through the Bragg condition, is shown in Fig. 2.4 (a) and (c). The asymmetric shape occurs due to photon absorption by the crystal. The normalized intensity of the standing wave field can be expressed by

$$\frac{I}{I_0} = \frac{|\mathbf{E_0} + \mathbf{E_H}|^2}{E_0^2} = 1 + \left|\frac{E_H}{E_0}\right|^2 + 2\left|\frac{E_H}{E_0}\right|\cos(\nu - 2\pi\mathbf{H} * \mathbf{r}) \tag{2.10}$$

whereby the intensity ratio of the reflected and incoming wave can be expressed by the reflectivity R

$$R = \frac{I_H}{I_0} = \frac{|E_H|^2}{|E_0|^2} \tag{2.11}$$

.

H represents the reciprocal lattice vector, oriented normal to the wave field planes, and **r** is the real-space vector defining the position where the intensity is measured. The scalar product can be written as $\frac{z}{d_H}$ due to the perpendicular distance z of the adsorber to the scattering planes, which have a distance of d_H to each other. The phase ν defines the relationship between $\mathbf{E_0}$ and $\mathbf{E_H}$. They are coherent if ν is time and space independent. Equation 2.11 can consequently be simplified to:

$$\frac{I}{I_0} = 1 + R(E) + 2\sqrt{R(E)}\cos(\nu(E) - 2\pi\frac{z}{d^H}) \tag{2.12}$$

In Fig.2.4 the situation of an particle (shown in blue) located at $\frac{3 * d_{hkl}}{2}$ above the surface is considered and the photon energy is scanned in the following through the Bragg condition: (a) when the photon energy reaches the Bragg energy, the incident wave is reflected (reflectivity is shown in red) and the standing wave field is formed. (b) The nodes (intensity minima shown in white) of the wave field are located at the crystal planes and the antinodes (intensity maxima highlighted in red) at the plane of the particle. (c) If the photon energy is shifted further through the Bragg condition, the phase ν changes by π (shown in green). (d) The nodes and antinodes are shifted in this case by the value of $\frac{d_{hkl}}{2}$. The atom is now located at a minimum of the wave field and can absorb fewer photons than in Fig. 2.4 (b). The amount of absorbed photons differs therefore for atoms at inequivalent adsorption heights, as their position relative to the nodes and antinodes of the modulated X-ray interference field is inequivalent.

In the XSW experiment, XPS spectra are measured at different photon energies while scanning the photon energy through the Bragg condition to record the number of emitted photoelectrons, as it is proportional to the number of absorbed photons. This can be done specifically for each atomic species. The integrated XPS signal versus the photon energy, the so-called yield curve Y(E-E$_{Bragg}$), then describes the amount of absorbed photons. As the intensity of the wave field (in equation 2.12) is assumed to be proportional to the photon absorption Y(E-E$_{Bragg}$), the vertical adsorption position of each species relative to the Bragg planes can be determined by fitting the yield curve with the reflectivity R and the phase ν.

In all experiments performed in this work the incidence direction of the X-ray beam was chosen perpendicular to the crystal planes, as the full width of the reflectivity curve depends on this angle and is the largest for normal incidence which is therefore called normal incidence X-ray standing wave (NIXSW). The main advantage of NIXSW is that the width of the curve is in this case not dominated by the mosaicity of the crystal.

Coherent position and fraction

Inequivalent adsorption heights of the atoms can be expressed by a normalised distribution function f(z) which describes the spread of the atoms around their average position. This spread occurs due to vertical disorder based on surface defects and different adsorption sites in complex unit cells and by thermally induced vibrations. Equation 2.12 is then replaced by [Woo98]:

$$\frac{I}{I_0} = 1 + R(E) + 2\sqrt{R(E)} \int_0^{d_{hkl}} f(z) \cos(\nu(E) - 2\pi \frac{z}{d_{hkl}}) dz \tag{2.13}$$

which can also be written as:

$$\frac{I}{I_0} = 1 + R(E) + 2F^H \sqrt{R(E)} \cos(\nu(E) - 2\pi \frac{D^H}{d_{hkl}}) \tag{2.14}$$

D^H reflects the coherent distance and the fraction D^H/d_{hkl} represents the coherent position P^H. It describes the average height of one species above the nearest Bragg

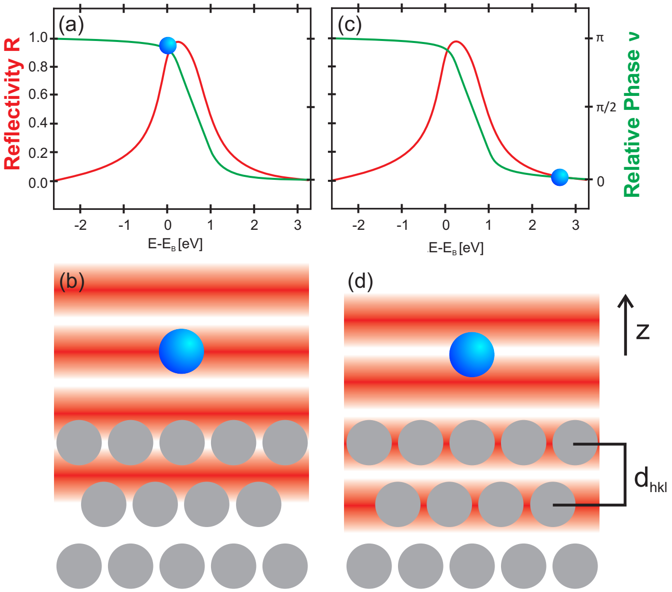

Figure 2.4.: Schematic diagram of the XSW eyperiment. (a) Reflectivity curve and relative phase for an atom located on an intensity antinode as shown in (b). (c) During scanning through the Bragg condition the phase changed by π and the wave field is shifted by d$_{hkl}/2$. The atom lies therefore at an intensity node as shown in (d).

plane. F^H is the coherent fraction and has a value between 0 and 1, as it reflects the vertical order of the measured atoms. It is zero if the atoms are homogeneously distributed at different vertical positions and it is one if all atoms are located at exactly the same position above the crystal.

In cases where several well defined adsorption heights for one species occur, the so-called Argand diagram is helpful for interpreting the XSW results, as shown in Fig. 2.5. The coherent fraction and position are drawn as a vector in a polar diagram. The vector length reflects the coherent fraction and the polar angle represents $2\pi P^H$. If one species is located at two different adsorption heights 1 and 2, as shown in Fig. 2.5, the resulting vector $\mathbf{V}_{total}$ consists of the sum of the vectors of the single components $\mathbf{V}_1$ and $\mathbf{V}_2$ with the corresponding parameters P_j^H and F_j^H [Woo98]:

$$F_{total}^H * \exp(2\pi i P_{total}^H) = \sum_j F_j^H * \exp(2\pi i P_j^H) \tag{2.15}$$

The Argand diagram allows for a deconvolution of all contributing signals by a vector analysis. Additionally it can be need for visualizing the accuracy of the individual scans of one species.

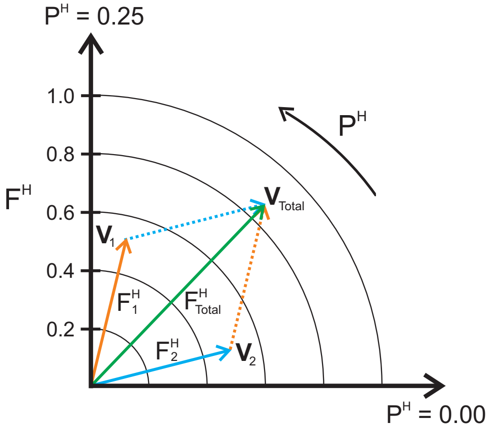

Figure 2.5.: Argand diagram containing hypothetical data for two different adsorption sites 1 and 2, but equally occupied (related to [Sta13]).

Experimental set up

All NIXSW measurements described in this section were performed at the Diamond light source in Didcot at beamline I09. An Ag(111) crystal was used, which showed a low mosaic spread. Each NIXSW data set was measured on one spot for less than 20 minutes in order to avoid beam damage. We tested if the coherent fraction decreased in this time significantly, which would be a indication of beam damage, but this was not the case.

We recorded the C1s, O1s, N1s and Cu2p core level signal off Bragg for the establishment of a proper fitting model for all XPS data without any standing wave field effects. Uncertainties were reduced by carrying out the measurement of each species up to six times. The spectra were all measured at room temperature and 60 K.

2.5. Scanning tunnelling microscopy

The basic principles of scanning tunnelling microscopy (STM) were demonstrated by Binnig and Rohrer in 1982 [BRGW82a],[BRGW82b]. The method is based on the quantum mechanical tunnel effect (as shown in Fig. 2.6 (b)), as particles are not able to tunnel through a vacuum gap in classical mechanics. This technique allowed for the imaging of conducting surfaces with atomic resolution in real space for the first time. A sharp metal tip is scanned above a surface at a distance of a few Ångstrom, as shown in Fig. 2.6 (a). A bias voltage U is applied between tip and sample and consequently a tunnelling current I can be recorded in the vacuum gap. The potential barrier Φ arises mainly from the work function of the material. The wave function decays exponentially

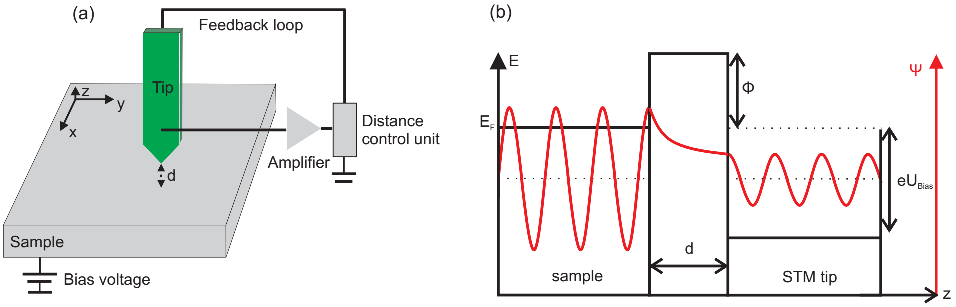

Figure 2.6.: (a) Schematic diagram of a scanning tunnelling microscope. (b) Potential diagram of the quantum mechanic tunneling effect. The wave function of a particle is displayed in red.

with a decay constant κ in the vacuum gap with the width d between sample and tip as shown in Fig. 2.6 (b) by:

$$\Psi(d) = \Psi(0) * e^{-\kappa d} \tag{2.16}$$

Electrons can cross the barrier, as the probability that a electron is located at a distance d is $|\Psi(0)|^2 * e^{-2\kappa d}$, which is larger than zero. This is possible as the applied bias induces a energy shift of eU$_{Bias}$ between the Fermi levels of the tip and the sample, which allows for tunnelling in one direction, as shown in Fig. 2.6 (b).
For atomic resolution a very sharp tip is essential, where ideally only one single tip atom contributes to the tunnelling current. This leads to the measurement of very localized tunnelling, which consequently enables a very high resolution. The precise motion of the tip is controlled by three piezoelectric elements, which enable two different scanning modes. In the constant current mode a feedback loop keeps the tunnelling current constant by changing the vertical position of the tip, which leads to a topographic image of the surface. In contrast in the constant height mode the distance between tip and sample is hold constant and the tunnelling current in dependence on the lateral tip position is displayed in an image.

Scanning tunnelling spectroscopy

Besides imaging the surface topography, the set-up can be extended to study the local density of states (LDOS) by scanning tunnelling spectroscopy (STS). In this method the tunnelling current between the metallic tip and the sample is recorded in dependence on the applied bias U$_{Bias}$. This gives access to the occupied and unoccupied states, as the tunnelling current and the first derivative dI/dU, which is proportional to the LDOS as shown below, are recorded. The interpretation of the measured signal becomes complicated as the current I depends additionally on the local density of the tip states ρ_T, as $I \propto \rho_S * \rho_T$. This was proven by Bardeen 1961 [Bar61] who calculated the tunnelling current by Fermi‘s Golden rule. The current I can expressed in time-dependent perturbation theory by the following:

$$I = \frac{2\pi e}{\hbar} \sum_{t,s} [f(E_t) - f(E_s - eU_{Bias})] |M_{t,s}|^2 \delta(E_t - E_s) \tag{2.17}$$

where f(E) is the Fermi function, $M_{\mu\nu}$ is the tunnelling matrix element between the states Ψ_t (tip) and Ψ_s (surface), U_{Bias} is the applied bias between the electrodes and $E_{t/s}$ is the energy of the state $\Psi_{t/s}$ in the absence of tunnelling.

Tersoff and Hamann [TH85] simplified the model by treating the probe as a sharp tip, which exhibits only s-wave functions:

$$I = \frac{2\pi e^2 U_{Bias}}{\hbar} \sum_{t,s} |M_{t,s}|^2 \delta(E_t - E_F) \delta(E_s - E_F) \tag{2.18}$$

The matrix element can be estimated under the assumption that the tip exhibits only s-wave functions. These simplifications allow one to reach the following integral:

$$I \propto \int_{-E_F}^{E_F + eU_{Bias}} \rho(\vec{r_0}, \epsilon) d\epsilon \tag{2.19}$$

where $\rho(\vec{r_0})$ represents the local density of states (LDOS) at the position $\vec{r_0}$ of the tip. If all assumptions are fulfilled, the tunnelling current is proportional to the local density of states close to the Fermi level and therefore STS allows for the investigation of these states. In addition, the findings of this section indicate that the contrast of STM images does not in first place reflect the topology of the surface, but mainly delivers information related to the electronic properties.

Semiconducting molecules adsorbed on a metal surface lead to additional electronic states which stem from molecular orbitals. For negative bias, the electrons tunnel from occupied molecular states to the tip or the inverse for positive bias, where the unoccupied molecular states contribute to the tunnelling contrast.

Experimental set-up

In this work, the lateral order of mixed heterostructures was determined using an Omicron STM system at room temperature. For the NTCDA-rich and annealed intermediate phases, images were recorded by a Createc STM at 5 K, which enables a more precise determination of the in-plane orientation of the molecules in relation to the silver substrate due to fewer movements and vibrations of the molecules at low temperatures. In addition, STS measurements were obtained for all molecules in the unit cells of these two phases. A lock in amplifier was used to receive a better signal quality of the dI/dU curves. It modulates the bias voltage U_{Bias} with a high frequency sinusoidal signal, the reference signal, in our case with a frequency of 912 Hz. This induces a sinusoidal response to the tunnelling current. The reference signal is multiplied with the current and integrated to remove all other frequency components. The tunnelling contrast of the occupied molecular levels, which are of special interest in this work, is obtained for a negative sample bias voltage U_{Bias}.

Distortion correction of STM images

The distortion of the STM images was corrected by the software WSxM. This was necessary due to a drift of the STM tip at room temperature. Strong distortions of the unit cell were clearly visible especially in scanning direction. This effect can be corrected if the unit cell parameters, (the vector length and the included angle), are known, as it is the case here from SPA-LEED images. The effectivity of the correction could be checked by analysing the shape of the CuPc molecules. The CuPcs should have a cross like shape with symmetric lobes, which was the case after the image correction.

3. Homomolecular structures of NTCDA on Ag(111)

Many different organic molecules adsorbed on metal substrates have been studied in the last few decades because of their crucial role for applications in electronic devices or sensors. Since it was found that the physical properties of the organic layers are strongly influenced by their structural properties, many studies have been focused on the preparation and characterization of well-ordered homomolecular films [USF96], [EBST04], [NRGR$^+$06], [KUS06], [GSS$^+$05], [HWCW11]. In this chapter a study of the π- conjugated molecule 1,4,5,8-naphthalene-tetracarboxylic-dianhydride (NTCDA) on the Ag(111) surface is shown. First, we summarize what is already known about the lateral and vertical structure and subsequently new results about the electronic properties, obtained from angle-resolved UPS (ARPES) and orbital tomography, are discussed.

3.1. Introduction

The long range order of NTCDA on the Ag(111) surface was studied by low-energy diffraction (SPA)-LEED and scanning tunneling microscopy (STM) by Kilian et al. Two different superstructures, depending on the molecular coverage on the substrate, were detected [KSK$^+$08], [SGS$^+$98]. In the coverage regime below 90 % of a monolayer the so-called relaxed monolayer (RML) or α- structure is formed (see Fig. 3.1 (a)). Upon additional NTCDA deposition the relaxed monolayer structure turns into a compressed monolayer (CML), called the β- structure (see Fig. 3.1 (b)). The diffraction patterns are simulated by red spots and the corresponding matrices of the superstructures are also displayed. Apparently some diffraction spots are not covered by the simulated superstructure; Kilian et al. claim that these spots are satellite spots which are shifted by a vector M in respect to the main spots. They assume that the modulation is a Moiré effect [KSK$^+$08]. The integer values in the matrix of the relaxed monolayer structure reflects the commensurate relation of the molecules to the silver substrate in contrast to the compressed monolayer, where the additionally adsorbed molecules force the already present molecules to arrange themselves into an incommensurate phase, which is indicated by the matrix of the compressed monolayer in Fig. 3.1 (b). Between the coverage regimes of relaxed and compressed monolayer of NTCDA, the so-called α_2- phase appears which is also incommensurate and coexists with one of the other two phases [KSK$^+$08].

The different NTCDA structures can also be prepared by annealing a multilayer film of NTCDA. Due to desorption of the molecules at first the compressed and then the

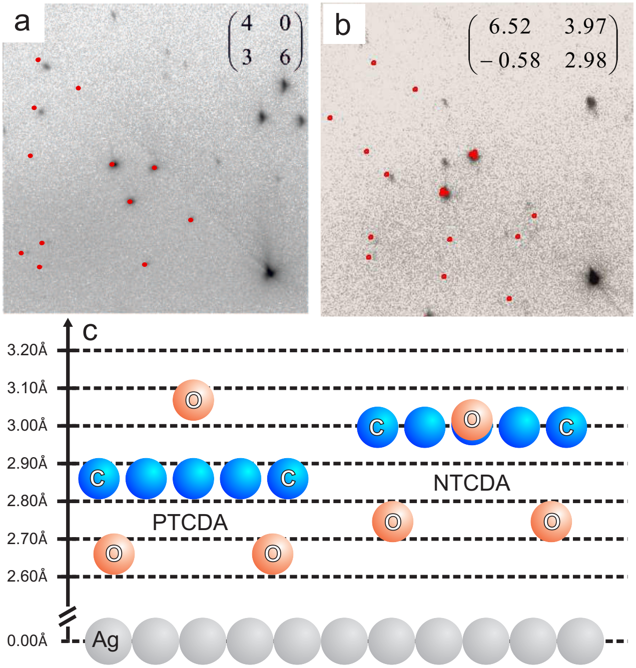

Figure 3.1.: (a) SPA-LEED images of the relaxed monolayer of NTCDA on Ag(111) and in (b) the compressed monolayer of NTCDA. The red dots indicate the simulated spots belonging to the matrix shown in the images. (c) The adsorption heights of PTCDA and NTCDA above the Ag(111) substrate.

relaxed phase appears there. The commensurate-incommensurate phase transition can be passed through in both directions. For the larger PTCDA molecule, which forms only one commensurate superstructure, a thermal desorption in the (sub-) monolayer regime is not possible. This a indication for the PTCDA molecules, having a stronger bonding to the Ag(111) compared to NTCDA, a finding which was confirmed by structural and electronic investigations: This is reflected by a lower adsorption height of PTCDA molecules at 2.86 Å in comparison to NTCDA (3.00 Å) [SHS$^+$07], [HKC$^+$05] (see Fig. 3.1 c), which was determined by normal incidence x-ray standing wave experiments. UPS measurements revealed a chemisorptive bond between the molecules and the Ag(111) substrate, which is stronger for PTCDA than for NTCDA [Tau07],[ZHK$^+$12]. This was proved by the larger partial filling of the former LUMO of PTCDA compared to NTCDA after deposition of the molecules on the silver substrate.

Furthermore, Schöll et al. [SKZ$^+$10] claimed that cooling the crystal leads to the NTCDA molecules becoming disordered on Ag(111). The characteristic diffraction pattern of NTCDA is completely gone at 150 K. This statement is controversial as it was not always reproducible. However the electronic properties reveal a shift to higher binding energies by 0.26 eV of the LUMO orbital to a binding energy of 0.48 eV. Cooling of the sample leads therefore to a stronger binding of the NTCDA molecules to the substrate [SKZ+10].

The NTCDA compressed monolayer was also investigated by UPS. The LUMO is also located above the Fermi level (0.4 eV) and is therefore also partially filled due the molecule‘s adsorption on the substrate. The HOMO of the CML of NTCDA was identified at a binding energy of 2.4 eV in a monolayer and 3.4 eV in a multilayer [BFS+07]. The vertical structure of the compressed monolayer of NTCDA has also been investigated by Stanzel et al. [Sta02]. With the analyser used for the experiment it was not possible to resolve anhydride and carboxylic oxygen. However, the carbon atoms were adsorbed 0.05 Å, and the oxygen atoms on average 0.10 Å higher than in the relaxed monolayer of NTCDA. The laterally denser packing of the compressed monolayer structure of NTCDA therefore goes along with an increased adsorption height.

3.2. Relaxed Monolayer of NTCDA

3.2.1. Lateral structure

In this section the lateral structure of the relaxed monolayer structure of NTCDA shall be discussed in detail. As already mentioned the relaxed monolayer of NTCDA grows in a commensurate structure with a superstructure matrix of:

$$\vec{M} = \begin{pmatrix} 4 & 0 \\ 3 & 6 \end{pmatrix} \tag{3.1}$$

The unit cell has a rectangular shape with vector lengths of $|\vec{A}|$ =11.57 Å and $|\vec{B}|$ =15.04 Å and has a size of 174 Å^2. This unit cell was in 1998 determined with a conventional LEED by Stahl et al. [SGS+98]. They suggested a structure model based on STM measurements at room temperature with two NTCDA molecules per unit cell arranged in parallel rows, which are rotated 60° with respect to the [-110] high symmetry direction of the substrate as shown in Fig. 3.2 (a). New low temperature STM images of Fournier [Fou14], shown in Fig. 3.2 (d), led to a new model. The molecules are oriented with their long molecular axis parallel to the [-110] direction, as shown in Fig. 3.2 (b) and in our room temperature STM image in Fig. 3.2 (c). The STM images at different temperatures confirm that the structure does not change if the sample is cooled rapidly. The misinterpretation of the molecular orientation of Kilian et al. probably arose from a drift of the STM tip and/or the sample during the measurements at room temperature. The same effects led to a distortion of our STM images at room temperature, but the images were corrected by the unit cell known from SPA-LEED.

Furthermore in the low temperature STM images it is clearly visible that the contrast of the two NTCDA molecules in the unit cell is different. Fournier [Fou14] therefore performed STS measurements of the relaxed monolayer of NTCDA on Ag(111). He distinguished between molecule type A and B. At the tummeling conditions chosen for

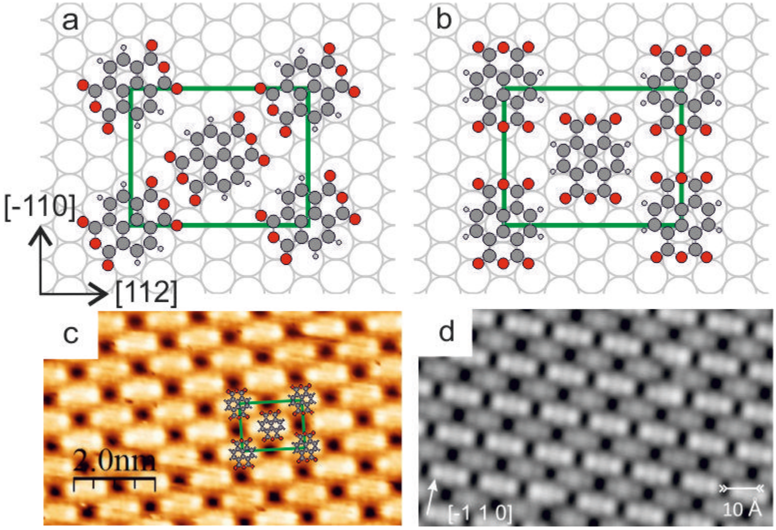

Figure 3.2.: Structure model of the RML of NTCDA on Ag(11): (a) Old structure model of Kilian et al. [KSK+08] where the long molecular axis is rotated by approximately 60° to the [-110] of the silver substrate direction. (b) New structure model where the molecules are aligned parallel to the [-110] direction. (c) Room temperature STM image (1.3 V and 34 pA). (d) STM image of the same system at low temperatures 50 mV and 100 pA [Fou14].

these images type A has a brighter electronic contrast in comparison to type B (see 3.2 (d)). Both molecules show a peak with a width of 400 mV at -30 mV, which is attributed to the former LUMO. In addition it was found that only the molecules of type A show a Kondo resonance at the Fermi level. This indicates a dependency between the adsorption site and the electronic properties.

3.2.2. Electronic structure

The electronic properties of the relaxed monolayer of NTCDA were already investigated by Schöll et al. [SKZ+10] by UPS. The assignment of the measured resonances to certain orbitals from UPS data above is difficult. Therefore we applied ARPES and orbital tomography, which enables us to assign the peaks to the correct orbitals directly, as the photoelectron yield depends on the orientation of the molecules on the substrate. The ARPES measurements were performed at the Bessy II synchrotron at beamline U125/2-SGM in Berlin. Information about the sample preparation and the experimental set up can be found in Chapter 2. The molecular wave functions of the LUMO and HOMO of NTCDA are displayed in Fig. 3.3. They are the basis for calculating the momentum distribution of the photoemission intensity of a specific orbital, which can be obtained from a hemispherical cut through the three-dimensional Fourier transform of the molec-

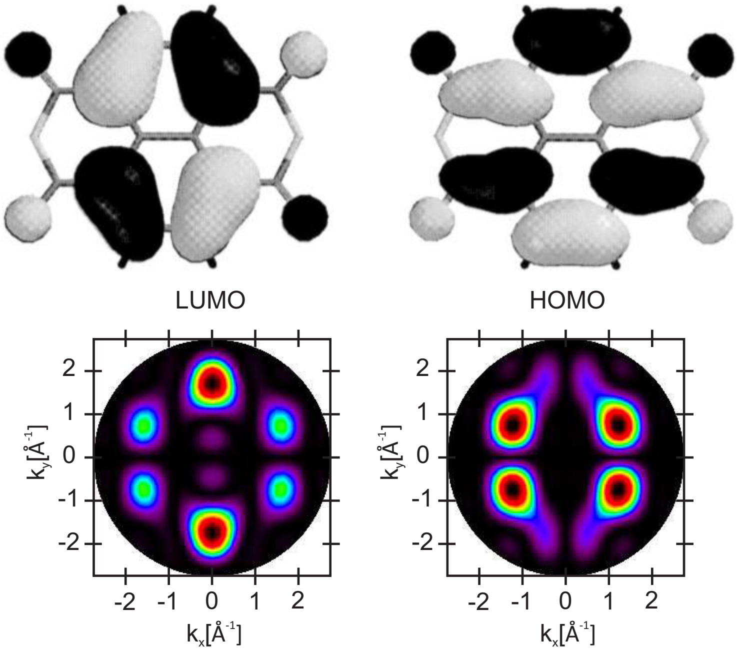

Figure 3.3.: Shape of the LUMO and HOMO of NTCDA calculated for a free molecule in the gas phase (DFT calculation using the semi-empirical MNDO approximation [SPGE98]). The corresponding momentum maps calculated for the LUMO and HOMO are shown underneath.

ular waves function at a certain radius k. These maps for the LUMO and HOMO of a free NTCDA molecule in the gas phase are plotted in the lower part of Fig. 3.3. For the generation of theoretical momentum maps, however, further assumptions have to be considered: firstly the threefold symmetry of the substrate and secondly the in-plane orientation of the molecules to the substrate, as this has a large influence on the intensity distribution of the maps. The resulting theoretical momentum maps of the LUMO (a) and HOMO (b) of NTCDA molecules, which are aligned with their long axis parallel to the [-110] direction of the substrate are shown in Fig. 3.4. A cut through the experimental ARPES data cube of the LUMO energy regime at a constant binding energy (CBE) of 0.2 eV is shown in panel (c). The corresponding CBE map of the HOMO at a binding energy of 2.4 eV is displayed in panel (d). The momentum maps of the LUMO as well as the map of the HOMO have six intensity maxima. The intensity maxima of the LUMO are rather sharp and the maxima are located at a distinct distance $k = 1.8$ Å^{-1} from the $\overline{\Gamma}$-point of the surface Brillouin zone. The intensity maxima of the HOMO are a little less sharp and are located at a smaller k-value $k = 1.5$ Å^{-1}. The theoretical momentum maps of the LUMO and the HOMO are in good agreement with the experimental

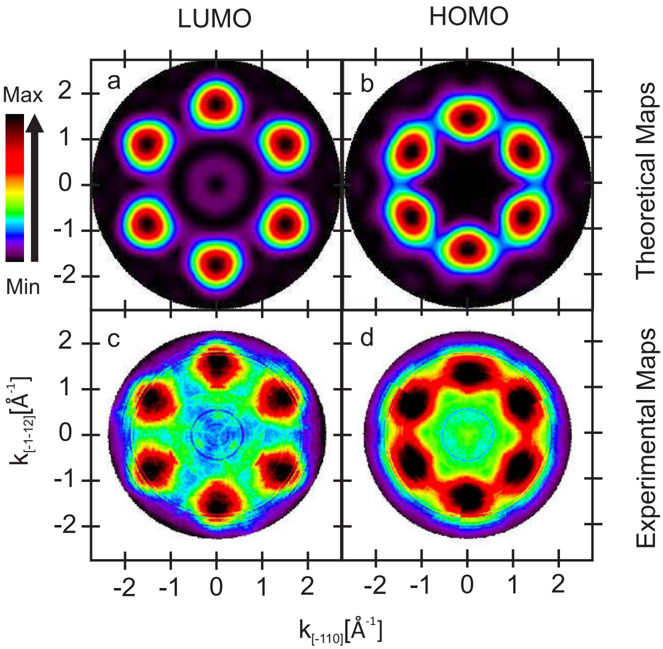

Figure 3.4.: The theoretical momentum maps for the LUMO (a) and HOMO (b) under consideration of the p3m1 symmetry of the substrate. The NTCDA molecules are parallel aligned to the [-110] direction. Underneath the experimental constant binding energy (CBE) maps in the energy regime of the LUMO (c) and HOMO (d).

maps and can therefore be assigned directly to LUMO and HOMO. Due to the sixfold symmetry of the Ag(111) substrate, the momentum maps for all molecular orientations with $n * 60°$ (n=0,1,..4,5) to the substrate have exactly the same intensity distribution. Therefore it can not be determined if the structure model of Kilian et al. or the new model of Fournier [Fou14] is correct.

3.3. Compressed monolayer of NTCDA

3.3.1. Lateral structure

The lateral structure of the compressed monolayer of NTCDA on Ag(111) was also investigated with room temperature STM, as shown in Fig. 3.5. The unit cell has vectors with lengths of $|\vec{A}| = 9.57\,Å$ and $|\vec{B}| = 16.45\,Å$, which enclose an angle of 88.5°. Furthermore, the unit cell has an area of $157.4\,Å^2$. It is indicated by a blue rectangle in Fig. 3.5, which is rotated 38° to the [-110] direction of the Ag(111) substrate. Two

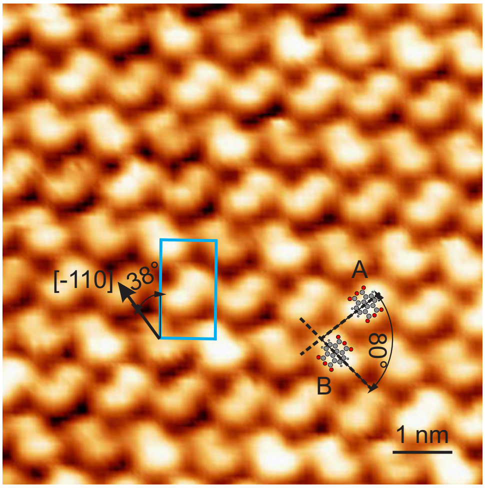

Figure 3.5.: Room temperature STM image of a compressed monolayer NTCDA on Ag(111) at U=-2.0 V and I=0.03 nA. The unit cell is indicated by a blue rectangle and its orientation to the [-110] direction. The unit cell contains two inequivalent molecules A and B which are rotated by 80° to each other.

inequivalent molecules A and B are arranged in a herringbone structure in the unit cell. The long axis of molecule A is aligned with the [-110] silver direction and molecule B is rotated 80° with respect to molecule A. This configuration is very similar to the herringbone monolayer structure of PTCDA on Ag(111) where the molecules are rotated by 78° to each other [KTH+06]. It is likely that this arrangement enables the molecules to establish hydrogen bonds between the oxygen and hydrogen atoms of adjacent molecules [RTT07]. The knowledge about the lateral structure is a basic requirement for the deconvolution of ARPES data by orbital tomography, which we perform in the next section. It allows for the individual determination of the binding energies of the orbitals of both inequivalent NTCDA molecules.

3.3.2. Electronic structure

We performed both, an angle-integrated and angle resolved PES on the compressed monolayer of NTCDA on Ag(111), both in the energy regime of the LUMO and HOMO. The UPS spectrum of the compressed monolayer of NTCDA on Ag(111) is shown in Fig. 3.6. The experimental data are displayed by green circles. The background of inelastically scattered photoelectrons is described by a exponential decay function (shown in red) and the molecular resonances are fitted by Gaussian peaks. The LUMO peak, i.e., the energy region just above the Fermi level, is fitted by of a Gaussian peak with the is fitted by a Fermi distribution function, as the LUMO is partially filled and has a binding energy of $E_{Bind} = 0.1$ eV (orange peak). The HOMO of NTCDA is displayed

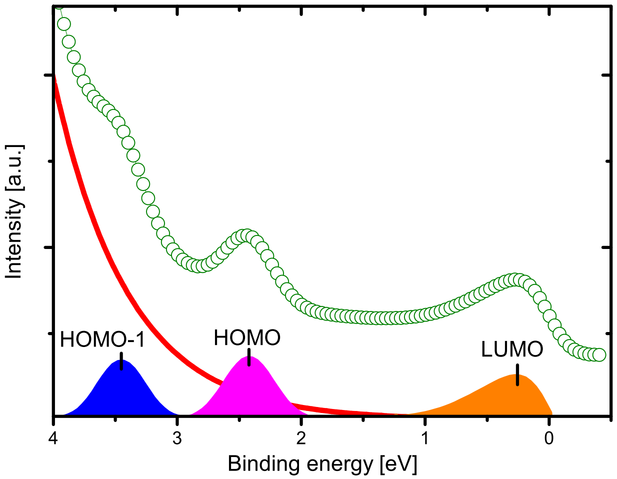

Figure 3.6.: The UPS spectrum of the compressed monolayer of NTCDA on Ag(111). The red line is a background function which decreases exponentially and represents the inelastically scattered photoelectrons. The other three coloured peaks represent the PES signal stemming from the molecular orbitals of NTCDA.

by a magenta coloured Gaussian peak at a binding energy of $E_{Bind} = 2.43$ eV. The HOMO-1 is shown by a blue peak at a binding energy of $E_{Bind} = 3.46$ eV.

The angle-resolved UPS data of the compressed monolayer of NTCDA were investigated to separate the electronic contributions of the two inequivalent NTCDA molecules. This enables us to determine the exact binding energy of both orbitals.

Theoretical and experimental momentum maps of the CML of NTCDA on Ag(111)

For the deconvolution of the ARPES data cubes, theoretical momentum maps have to be calculated for all contributing orbitals. The known in-plane orientation of the molecules is used for the calculation of the corresponding constant binding energy (CBE) maps of a free molecule by density functional theory. Theoretical momentum maps of the HOMO and LUMO for both molecular orientations are shown in Fig. 3.7. The theoretical maps of the HOMO for molecule A (a) and molecule B (c) with six defined intensity maxima are shown. Molecule A has sharp maxima while molecule B has less intense maxima which are broadened. In addition the maxima of molecule B are rotated by 30° with respect to molecule A. Therefore the maxima of molecule B are located in the k-space

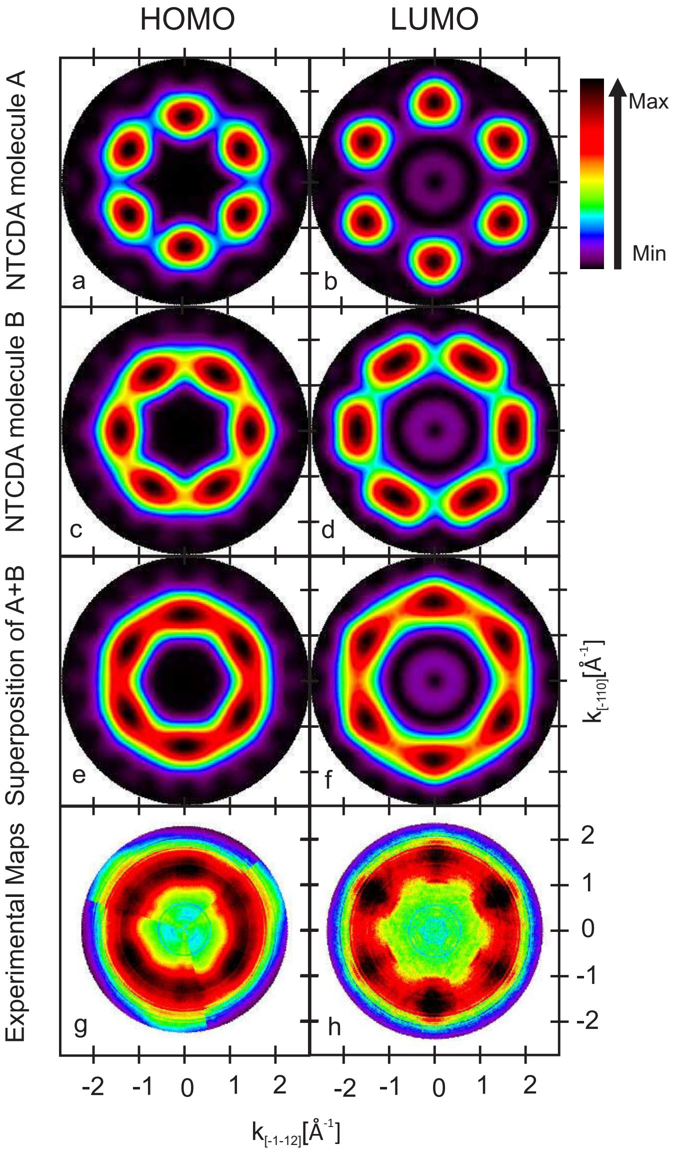

Figure 3.7.: The constant binding energy maps (CBE) for the HOMO and LUMO of a free molecule calculated by density functional theory considering the p3m1 symmetry of the substrate. The HOMO and LUMO for the differently orientated molecules A (0°) (a and b) and B (80°) (c and d) to the [-110] direction. In panel (e) and (f) the CBE maps of the measured HOMO and LUMO of a CML of NTCDA on Ag(111).

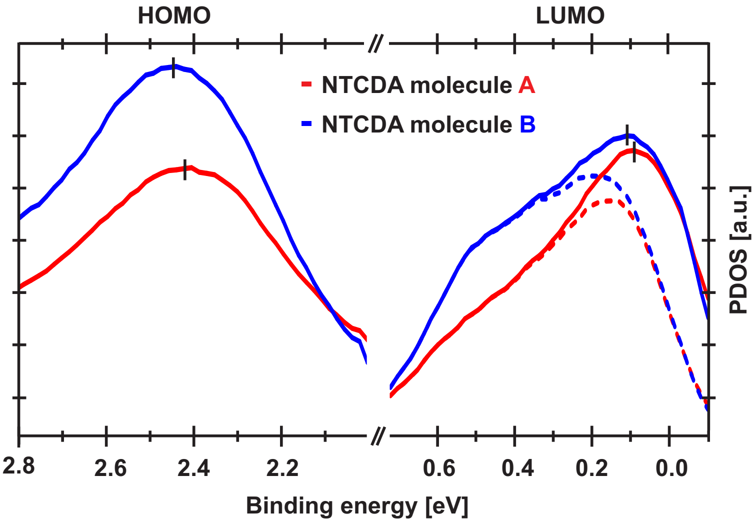

Figure 3.8.: The projected density of states (PDOS) of the HOMO and LUMO energy regime were obtained for both molecules in the compressed monolayer of NTCDA on Ag(111) by the orbital tomography analysis of the ARPES data. The markers indicate the position in energy of the LUMO and HOMO. The solid lines in the LUMO energy regime show the PDOS of the LUMO divided by the Fermi function at T_{eff} =930 K. The dashed lines reflect the PDOS cut by the Fermi level.

regime where molecule A has its intensity minima. This enables us to perform the full deconvolution of the ARPES data cube with rather high reliability.

The situation is similar for the LUMOs of both molecules. The momentum maps of the LUMO of both molecules reveal a sixfold symmetry as well, in panel (b) molecule A is shown and in (d) molecule B. A superposition of both molecular orientations for the HOMO Fig. 3.7 (e) and for the LUMO energy regime (f) would be the result of the measured momentum map, if both molecules contributed to the same extend. The experimental data with its overall emission from the compressed monolayer NTCDA and the underlying Ag(111) substrate are shown in Fig. 3.7 (g) and (h). These maps represent cuts through the experimental data cubes, for the LUMO at a binding energy of $E_b = 0.2$ eV and for the HOMO at $E_b = 2.42$ eV. The comparison of the superposition of the theoretical maps with the experimental ones illustrate that the six intensity maxima stemming from molecule A are still dominant, while the maxima of molecules B disappear and form a ring-like structure. However the intensity between the six visible maxima is higher in the experimental maps compared to the superposition of the theoretical maps, which leads to the conclusion that molecule B contributes more strongly to the measured signal at these particular energies. Furthermore the experimental momentum map of the LUMO has a reduced symmetry. This stems from the contribution of the pure silver substrate which is threefold symmetric. The momentum map of the latter was measured on a clean silver crystal and was considered for the deconvolution of the LUMO.

Orbital tomography deconvolution: CML of NTCDA/Ag(111)

The molecular distribution for the momentum maps of the energy region of the LUMO and HOMO was analysed quantitatively by orbital tomography. This fitting procedure was performed at the corresponding binding energy regimes of the HOMO and LUMO. The result of the fit can be understood as the density of states projected onto its molecular orbital (projected density of states, PDOS). The result of the fit, the PDOS of both molecules A and B contained in the compressed monolayer of NTCDA, is displayed in Fig. 3.8 as a function of the binding energy E_B. The fit reveals the slightly different binding energies for the LUMOs and for the HOMOs of both molecules. The HOMOs of molecules A and B have a binding energies of $E_B = 2.42$ eV and $E_B = 2.44$ eV respectively, which is in good agreement with the fitting result of the UPS spectrum, where the HOMO of NTCDA is located at $E_B = 2.43$ eV. Even so the binding energie difference between the orbitals is small, the curves in Fig. 3.8 are completely shifted to each other, which indicates that the effect is real.

The binding energy of the LUMOs of both molecules was determined from the fitted PDOS peaks after dividing by the Fermi function for an effective temperature $T_{eff}=$ 930 K (see solid lines in Fig. 3.8). Here T_{eff} is not a real temperature but comes from a broadened Fermi distribution function ($T_{sample} = 300$ K) and for an instrumental resolution of 150 meV. The binding energy is determined afterwards by the maximum of the density of states. Thus the LUMO of molecule A is located at a binding energy of 0.09 eV and the LUMO of molecule B at 0.11 eV (UPS: $E_B = 0.1$ eV). The energy difference between the two LUMOs of NTCDA is just 20 meV and is therefore much smaller than for the two inequivalent molecules contained in the herringbone structure of PTCDA, which exhibit an energy splitting of 170 meV [SWR$^+$12]. This indicates a weaker electrostatic potential difference between the NTCDA molecules A and B which arises from the quadrupole moments of the molecules and their induced electric fields [WSS$^+$13]. In addition, for the NTCDA structure both orbitals are less strongly filled than the orbitals of PTCDA. The reduced occupation of the LUMO of NTCDA confirms the weaker charge accepting character of NTCDA in comparison to PTCDA.

3.4. Conclusion

The resonances of the UPS spectrum of the relaxed monolayer of NTCDA on Ag(111) could be directly assigned to the LUMO and HOMO by ARPES measurements. The in-plane orientation of the molecules could not be identified unambiguously due to the symmetry of the (111) surface.

The lateral structure of the inequivalent NTCDA molecules in the compressed monolayer of NTCDA on Ag(111) was identified by STM measurements. The molecules arrange in a herringbone structure, 80° rotated to each other, similar to PTCDA on Ag(111). The molecules have to leave the commensurate adsorptions sites, which they exhibit in the brick wall structure of the RML of NTCDA, for arranging in a 10 % denser packed structure of the compressed ML. This is necessary as the oxygen atoms hinder the molecules in the brick wall structure to arrange in a denser packed structure. In addition hydrogen bridges are established due to the higher packing density of the compressed ML, as they probably lead to an additional attractive intermolecular interaction channel between the molecules.

The knowledge about the in-plane orientation related to the substrate was used for a deconvolution of the ARPES data by orbital tomography. It could be proved that NTCDA is a weaker charge acceptor compared to PTCDA. In addition, the LUMOs of the inequivalent NTCDA molecules are split by 20 meV in contrast to the LUMOs of the inequivalent PTCDA molecules, which are separated by 170 meV.

4. The laterally mixed heteroorganic monolayer system: NTCDA and CuPc on Ag(111)

4.1. Introduction

In this chapter, the lateral structure, the vertical geometry and the electronic properties of different heteroorganic monolayer systems have been studied. First a short overview on the results of the previously studied system PTCDA + CuPc on Ag(111) is given, which was earlier investigated by Stadtmüller et al., and is used as a reference system for the subsequently investigated heterostructures. The coverage ratio dependent mixed phases of PTCDA and CuPc have been already studied by SPA-LEED, NIXSW, LT-STM, UPS and ARPES. Based on these earlier studies, in this work the electron acceptor PTCDA was replaced by 1,4,5,8-naphthalenetetracarboxylic dianhydride (NTCDA), which interacts more weakly with the silver substrate. The electron donor copper-II-phthalocyanine (CuPc) was kept.

PTCDA, NTCDA and CuPc are typical prototype molecules whose homomolecular structures were studied very well by now. Interestingly the molecules have very different adsorption behaviours on a Ag(111) crystal. NTCDA and PTCDA grow in the submonolayer regime in islands, resulting from an attractive interaction between the molecules. In contrast, CuPc forms a dilute phase with isolated molecules due to a repulsive interaction. At a coverage of about 0.9 ML the molecules are sterically forced to accumulate in an ordered pattern [KSS+10]. Moving to the heterostructure, the exchange of the charge accepting molecule PTCDA by its smaller perylene derivate NTCDA should lead to different laterally ordered structures. Firstly, the lateral structure‘s in dependence on the stoichiometric ratio of the molecules was determined by high resolution electron diffraction (SPA-LEED) and scanning tunnelling microscopy (STM). Secondly, the vertical structure which reflects the bonding strength between the molecules and the metal substrate was characterized by normal incidence X-ray standing wave experiments (NIXSW). At the end of this chapter it is explained how the different geometric structures influence the electronic properties of the heteroorganic films. This was studied by angle resolved ultraviolet photoelectron spectroscopy (ARPES). A pre-condition for the performance of this method is that the molecular orientations with respect to the substrate are known. This information was obtained by STM measurements.

4.2. The reference system CuPc + PTCDA

4.2.1. Lateral structure

In this section a short overview of the lateral mixed PTCDA-CuPc phases on Ag(111) is presented because it represents the basis for the subsequent study of NTCDA-CuPc heterostructures. This system was investigated intensively in the dissertation of Benjamin Stadtmüller [Sta13]. SPA-LEED measurements were performed for different PTCDA:CuPc ratios. Depending on the coverage ratio, three different laterally mixed structures, which are shown in Fig. 4.1, were determined. The CuPc:PTCDA ratio increases from left to right in Fig.4.1. The PTCDA-rich phase is called the Mixed Brick Wall (MBW) phase and is found for a coverage of $\Theta_{CuPc} < 0.4$ ML and $\Theta_{PTCDA} > 0.5$ ML Fig.4.1 (a). The unit cell is commensurate and contains two PTCDA molecules and one CuPc molecule. The molecules' arrangement can be seen in the STM inset in Fig 4.1 (a).

Up to a CuPc coverage $\Theta_{CuPc} < 0.75$ ML and $\Theta_{PTCDA} > 0.5$ ML the One-to-One phase arises, which grows in a point-on-line correlation to the silver substrate. This unit cell contains just one CuPc as well as one PTCDA molecule as shown in Fig.4.1 (b).

The Zig-Zag phase appears for a CuPc coverage $\Theta_{CuPc} > 0.75$ and PTCDA below 0.3 ML (see Fig.4.1 (c)). A variety of incommensurate CuPc-rich phases was found. Upon increasing the CuPc coverage the unit cell sizes decrease slightly. Although an STM image of this phase does not exist, a structural model was suggested based on SPA-LEED and pair potential. Two CuPc molecules form rows in this unit cell which

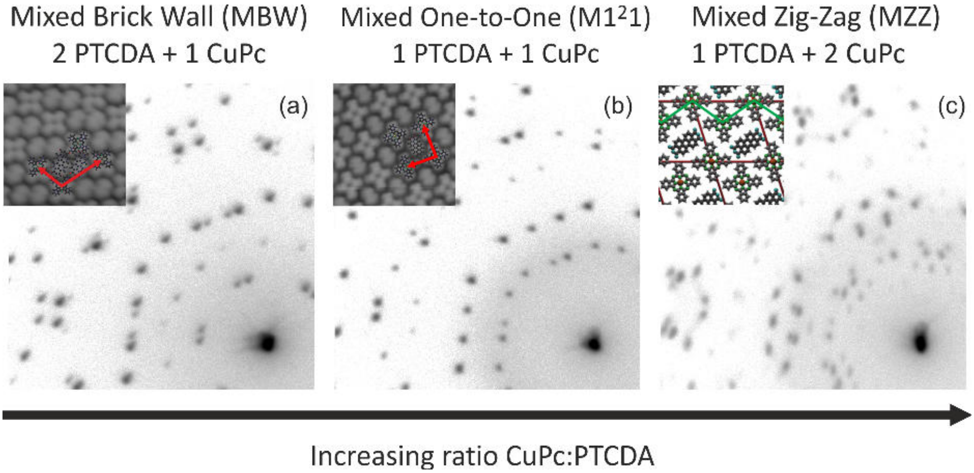

Figure 4.1.: Overview of all coverage-dependent CuPc + PTCDA mixed phases, all measured by SPA-LEED at 27.2 eV. (a) Mixed Brick Wall phase (b) Mixed One-to-One phase (c) Mixed Zig-Zag phase. The insets of (a) and (b) contain STM images of the corresponding phase and in (c) a structure model is shown. (All images from [Sta13]).

are separated by single PTCDA molecules. The continuously changing unit cells are probably caused by the intermolecular repulsion between the CuPc molecules which was also found earlier for the homomolecular CuPc structures [KSS+10]. In general it was ascertained that the unit cell size of the heteromolecular phases decreases with increasing CuPc coverage.

4.2.2. Adsorption geometry

The adsorption heights of CuPc and PTCDA were determined by NIXSW for the Mixed Brick Wall (at 50 K) and the Zig-Zig phases (at room temperature). In both cases an adsorption height alignment of the CuPc and PTCDA was observed (see Fig.4.2). This was a surprising result due to the contradicting electronic properties of this structure, which is explained in detail in chapter 3.2.3. The carbon backbone of PTCDA, in its homomolecular phase, adsorbs 2.86 Å above the silver substrate, in contrast to the CuPc ML where the CuPc backbone exhibits an adsorption height of 3.08 Å. In the mixed phases, the PTCDA backbone gets lifted to 3.00 Å and the CuPc backbone lowered to 3.04 Å. A very similar adsorption behaviour was observed for the Zig-Zag phase. Again an adsorption level alignment of the molecules was observeded with the PTCDA backbone at an adsorption height of 3.01 Å and CuPc backbone at 3.07 Å. This effect is explained by a substrate-mediated charge transfer from the donor molecule CuPc to the charge-accepting molecule PTCDA. The donor is not only able to push back the electron spill-out from the metal substrate towards the surface but also towards the PTCDA molecules. This leads to a decreased charge spill out underneath the donor molecules and consequently to a reduced adsorption height. The opposite mechanism, an increased charge spill-out below the acceptor occurs, which consequently generates an increased adsorption height of the acceptor PTCDA. This explains the height-alignment of the molecules [SSB+14].

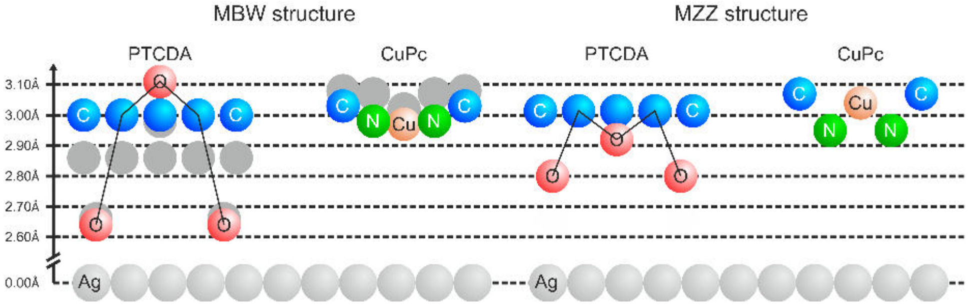

Figure 4.2.: Side view of the adsorption height model determined by XSW of the MBW- and MZZ phase. The different species of the mixed structures are plotted and the adsorption heights of pure CuPc and PTCDA homomolecular films are indicated in grey. [SSB+14]

4.2.3. Electronic properties

The charge transfer between the molecular orbitals and the substrate was determined by UPS. The purpose of this was to deliver an explanation for the vertical adsorption geometry and achieve a deeper understanding of the electronic structure of the mixed structures. It is known of the homomolecular films that the former LUMOs of adsorbed CuPc as well as of PTCDA are partially filled due to charge transfer from the substrate to the molecules [KSS^{+}10]. UPS measurements of the mixed films showed a shift of the heteromolecular LUMO to higher binding energies compared to the homomolecular LUMO. However at this stage it was not clear specifically which molecular orbitals contribute to the charge transfer (see Fig. 4.3 (a)). Therefore, a deconvolution of the molecular distributions was performed by ARPES and orbital tomography. This deconvolution demonstrated that the CuPc LUMO becomes completely depleted in contrast to the PTCDA LUMO which is entirely filled (see Fig. 4.3 (b)). This can be explained by a charge transfer from the CuPc molecules to the PTCDA molecules. This result was confirmed by STS measurements on the mixed films, shown in Fig. 4.3 (c).

The modification of the adsorption heights in the heteromolecular structures indicates a stronger interaction (smaller adsorption height) of the CuPc with the substrate and a weaker one (higher adsorption height) for PTCDA in comparison to their homomolecular phases. However from orbital tomography and STS data apparently the opposite relation is shown. The results from both measurements indicate that the charge transfer in heteromolecular films is no longer coupled to the adsorption height. This can be explained by local work function changes. CuPc increases the local work function at the PTCDA site, while PTCDA reduces it at CuPc sites. Furthermore the global

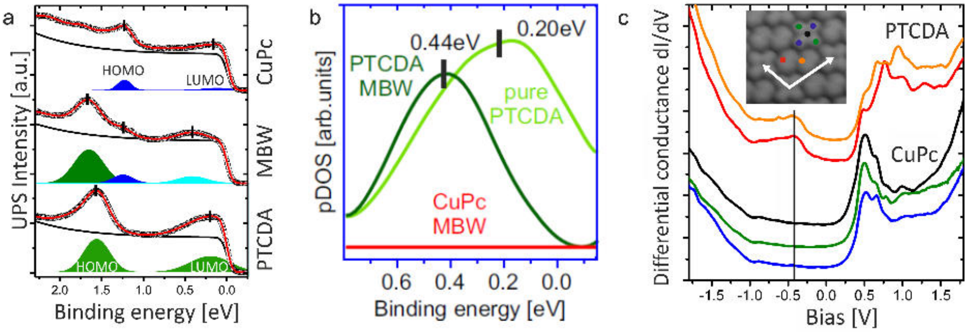

Figure 4.3.: (a) UPS spectra of the hommomolecular structures of PTCDA and CuPc plotted in comparison to the UPS spectrum of the MBW phase. (b) The projected density of states of pure PTCDA islands and PTCDA and CuPc molecules of the MBW phase, resulting from an orbtial tomography fitting procedure of ARPES data. (c) STS spectra of the MBW-structure for different CuPc and PTCDA molecules. [SLW^{+}14]

work function of the mixed heterostrucuture is between the homomolecular structures of CuPc/Ag(111) and PTCDA/Ag(111). This controls the energy level alignment such that CuPc reduces its charge uptake from the substrate and that of PTCDA is increased. [SLW$^+$14].

4.3. Lateral structure of CuPc + NTCDA / Ag(111)

4.3.1. Structure formation

In this section an overview of the structure formation of mixed NTCDA-CuPc films is given. The lateral structure of these films was investigated by SPA-LEED and STM. These methods were performed in two different UHV chambers and therefore the prepared organic samples were not measured on the same sample.

Independent of the deposition sequence of the molecules, long range ordered films were formed. Three different mixed phases arose which depend on the ratio of CuPc and NTCDA molecules. The resulting diffraction pattern of these experiments are shown in Fig 4.4. In the following the coverage regimes in which we observed the different phases are described. For a NTCDA and CuPc coverage of $\Theta_{NTCDA} \geq 0.7$ ML and $\Theta_{CuPc} \leq 0.3$ ML, an NTCDA-rich structure was grown, the LEED pattern of which is shown in Fig. 4.4 (a). An increased CuPc coverage between 0.4 ML$\leq \Theta_{CuPc} \leq 0.6$ ML leads to an intermediate phase with a coverage ratio of 1:1. The corresponding diffraction pattern is visible in Fig. 4.4 (b). The third phase, the CuPc-rich phase, consists of $\Theta_{CuPc} \geq 0.6$ ML and $\Theta_{NTCDA} \leq 0.4$ ML and its LEED image is displayed in Fig. 4.4 (c).

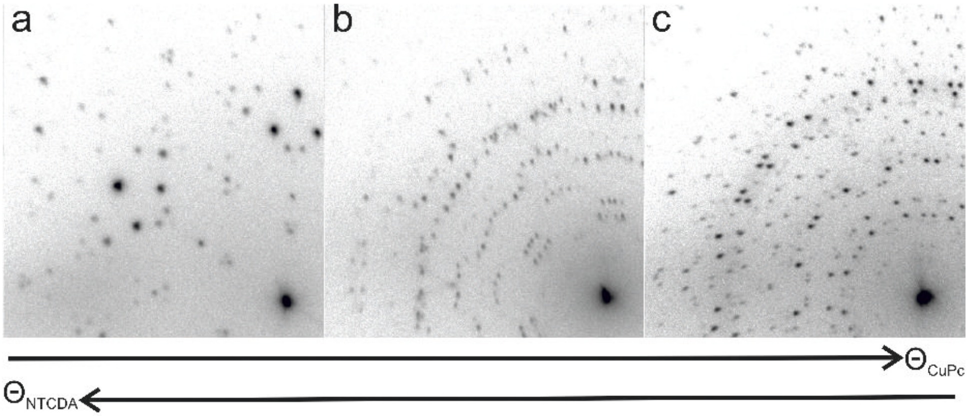

Figure 4.4.: Overview of SPA-LEED images of all coverage dependent CuPc + NTCDA mixed phases, each measured at 27.2 eV. (a) The NTCDA-rich phase (b) the intermediate phase and (c) the CuPc-rich phase.

These three mixed structures were formed without post-annealing, but for a better homogeneity of the films it is desirable. Annealing can however only be performed at a temperature lower than 450 K for 15 min due to the fact that NTCDA molecules desorb at this temperature, which would destroy the well-ordered mixed films. The structural changes which occur due to annealing will be discussed in chapter 5 in detail. At the borderlines between these three coverage regimes, a superposition of two phases can coexist.

A fourth mixed phase exists, the so-called annealed intermediate phase. It arose either when a stacked layer of a relaxed monolayer of NTCDA with approximately 0.5 ML CuPc on top was annealed higher than 550 K or when 0.6 ML of CuPc with 0.6 ML of NTCDA were annealed to 550 K. In the first case, the CuPc molecules in the second layer probably exchange with NTCDA molecules from the first layer due to a slow temperature increase, which subsequently desorb from the second layer. The remaining molecules form a mixed phase. In the second case, the molecules did not arrange in a well-ordered mixed layer by deposition alone. It remains unclear why this effect sometimes occurred. Only subsequent annealing of the deposited molecules led to the formation of the annealed intermediate phase.

In the following subsections, the various mixed structures are described in detail. The size and shape of the unit cells was determined by high resolution low energy electron diffraction (SPA-LEED). These results were confirmed by scanning tunnelling microscopy (STM), which also allows for the determination of the number of molecule and their in-plane orientation to the Ag(111) substrate. At the end of the chapter, the results are summarized and the phases are compared with each other and with the related CuPc-PTCDA heterostructures.

A. The NTCDA-rich phase

In this subsection, first of all the shapes of islands of the mixed NTCDA-CuPc structures are discussed in detail, based on STM measurements. These are compared with heteromolecular mixed islands consisting of PTCDA and CuPc and homomolecular islands of NTCDA. Subsequently the size and shape of the unit cell of the NTCDA-rich phase is determined by SPA-LEED and in the following the number and the orientation of the molecules is obtained by low temperature STM measurements.

Growth of lateral mixed structures

In the following an exemplary preparation of the NTCDA-rich phase is described for a better understanding of the growth mechanisms of the mixed films. For this preparation first NTCDA was deposited on a clean Ag(111) crystal and formed NTCDA islands. The subsequently deposited CuPc molecules are able to dissolve the NTCDA islands and arrange themselves together with the NTCDA in a mixed structure as can be seen in Fig. 4.5 (a). An island of the well ordered NTCDA-rich phase is viable in the middle of the image, surrounded by islands of the homomolecular relaxed monolayer structure of NTCDA. The molecules with the cross-like shape are CuPcs and the elliptical shaped

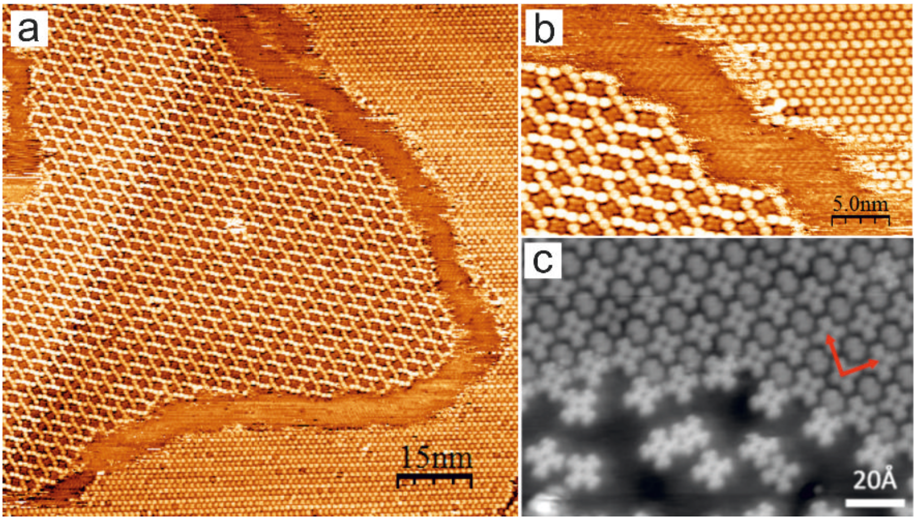

Figure 4.5.: (a) STM image of an island of the NTCDA-rich phase surrounded by a bare substrate strip and an island of the homomolecular NTCDA phase (U=-1.0 V and I=0.06 nA).(b) A magnified section of (a).(c) A heteroorganic layer, consisting of PTCDA and CuPc, measured by a low temperature STM (U=0.15 V and I=0.01 nA) from [Sta13].

molecules are the NTCDA molecules. The electronic contrast of the molecules will be discussed later in detail, but does not play a role in the observations discussed in the following. The mixed and homomolecular structure in Fig. 4.5 (a) do not border on each other directly everywhere on the sample, instead they are separated by a stripe, which looks like as there are not molecules located. This is shown magnified in Fig. 4.5 (b).

The mixing of the molecules indicates firstly that an attractive intermolecular interaction between the NTCDA and CuPc molecules exists, which enables the molecules to arrange in mixed islands, instead of staying in two separated homomolecular structures and secondly that the formation of mixed islands has to be energetically favourable. In this specific preparation, the coverage of CuPc molecules was too low for the formation of a homogeneously mixed film on the whole surface, which leads to remaining homomolecular NTCDA islands.

The appearance of the apparently bare substrate strip between the mixed and the homomolecular structure, which look like two fitting puzzle pieces, is astonishing. The question arises whether this strip really is bare substrate or is covered by a 2D gas of CuPc, which occurs for submonolayer coverages of homomolecular CuPc films on Ag(111), as it was determined by Kröger et al. [KSS^{+}10]. The molecules are not detectable in this case with a room temperature STM due to the large mobility of the molecules at this temperature (see Fig 4.5). The excess of NTCDA molecules and the large tendency of the molecules to arrange in mixed islands leads however to the assumption that the empty substrate area is not covered with a CuPc gas, since the CuPc molecules would then form islands of a mixed structure with the residual NTCDA. The bare substrate strip separates the islands of the NTCDA-rich phase from the homomolecular NTCDA structure. This indicates that it is energetically favourable that both structures are separated from each other if there is sufficient free space on the sample. Additionally the excess of NTCDA molecules proves that an NTCDA-rich phase which contains a higher NTCDA to CuPc ratio does not exist.

This result is even more remarkable due to the fact that each island of the NTCDA-rich mixed phase always terminates with a row of NTCDA molecules (see 4.5 (b)). The terminating NTCDA molecules of the NTCDA- rich phase and the NTCDA molecules of the homomolecular structure should be attracted to each other as it is the case for the homomolecular structures of NTCDA.

The situation is different for heteromolecular structures consisting of PTCDA and CuPc. In Fig. 4.5 (c) an STM image at low temperatures of the One-to-One phase is visible. Here all edges of the mixed structures are terminated by CuPc molecules [Sta13]. Either PTCDA-CuPc islands terminated by CuPc molecules are energetically more favourable or the reduced molecular mobility at low temperatures is responsible for this observation. These observations of different molecular terminations of the mixed island of the heterostructures consisting of either NTCDA-CuPc or PTCDA-CuPc can only be verified by STM measurements of the NTCDA-rich phase at low temperature. Images of the NTCDA-rich phase at low temperatures were recorded, but the edges of the structure could not be determined, as dirt was found at the edges or the islands stopped at step edges. A proper comparison of the two different heterostructures in identical conditions was therefore not possible.

Unit cell of the NTCDA-rich phase

The diffraction pattern of the SPA-LEED image already shown in Fig. 4.4 (a) was analysed by "Spot-Plotter". This is a software for the simulation of diffraction patterns, written by Patrick Bayersdorfer, which enables us to determine the size and shape of unit cells with high accuracy. In Fig. 4.6 (a) a simulation of the LEED pattern of the relaxed monolayer (RML) of NTCDA is indicated with red spots. In Fig. 4.6 (b) the SPA-LEED image of the NTCDA-rich phase with its corresponding simulation of the diffraction pattern plotted in red is shown. Remarkably, it is clearly visible that all spots of the RML of NTCDA are also present in the LEED pattern of the NTCDA-rich phase. This does not arise due to a coexistence of both structures; instead the unit cell of the NTCDA-rich phase is exactly six times the size of the RML of NTCDA and has the same in-plane orientation to the substrate. The basis vectors of the NTCDA-rich phase are multiples of the RML of NTCDA ($2*|\vec{A}|$ and $3*|\vec{B}|$). The short vector of both unit cells is aligned to the [-110] direction of the silver substrate. This results in a unit cell with the following superstructure:

$$\mathbf{M}_{\text{NTCDA-rich}} = \begin{pmatrix} 8 & 0 \\ 9 & 18 \end{pmatrix} \tag{4.1}$$

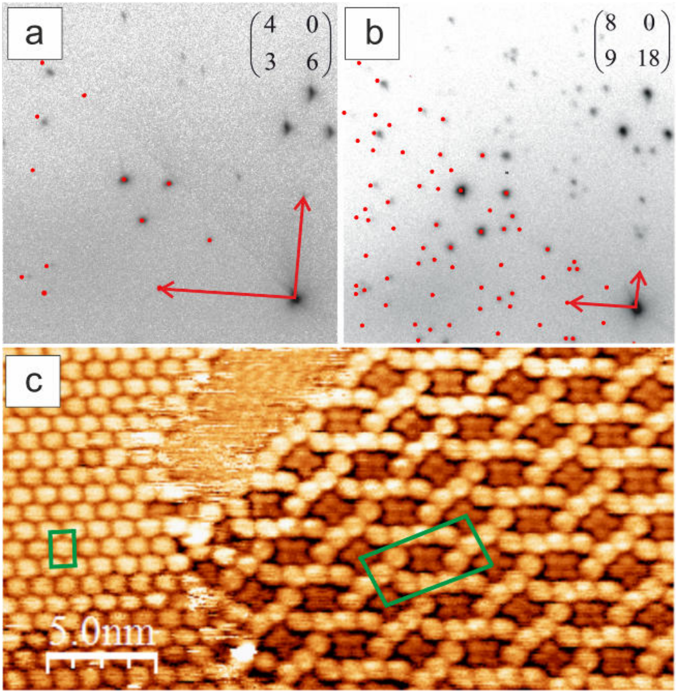

Figure 4.6.: (a) SPA-LEED image of the RML of NTCDA (b) SPA-LEED image of the NTCDA-rich phase, both at 27.2 eV. In both images the diffraction pattern (see matrix)is simulated by red spots.(c) STM image with the homomolecular structure of NTCDA on the left side and the NTCDA-rich heteromolecular phase on the right at U=-2.0 V and I=0.03 nA.

The unit cell is rectangular with a length of $|\vec{A}| = (23.1 \pm 0.1)$ Å and $|\vec{B}| = (45.0 \pm 0.1)$ Å. Further, it has a size of 1024 Å^2. These findings were confirmed by STM measurements. In Fig. 4.6 (c) the homomolecular structure of the relaxed monolayer of NTCDA is visible on the left side of the image and the NTCDA-rich phase on the right side.

The STM image confirms that the unit cell of the NTCDA-rich phase is two times broader and three times longer than the one of the RML of NTCDA. Both unit cells are highlighted by green rectangles. The unit cells are 60° rotated to each other, as two different rotational domains of both structures are shown.

The molecular orientation of NTCDA in the NTCDA-rich phase can be determined due to STM images recorded at 5 K, as shown in Fig. 4.7. In the inset a STM image of the RML of NTCDA is visible. The known molecular orientation of this structure (see chapter 2) proves that the axis which appears shorter in the electronic contrast is in fact the long axis of the molecules at a bias of 0.29 V.

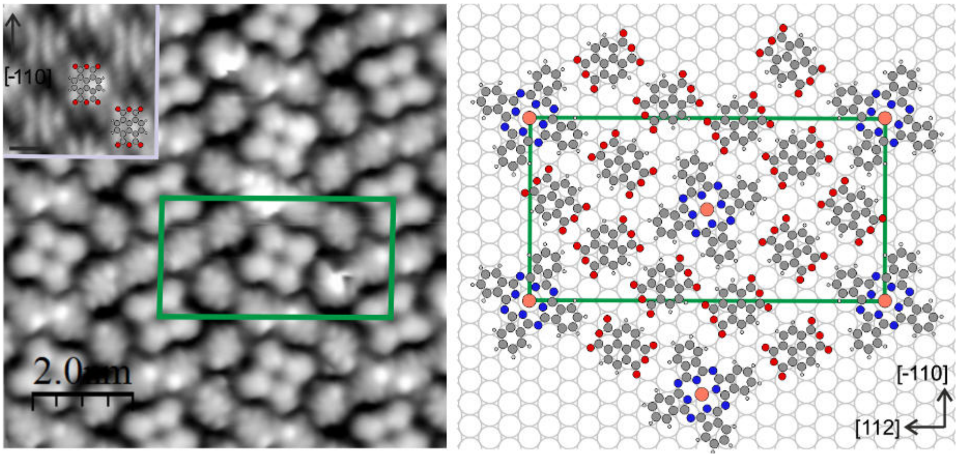

Figure 4.7.: On the left side: Low temperature STM image of the NTCDA-rich phase (U=0.24 V and I=0.6 nA). In the inset: LT-STM image of the RML of NTCDA (U=0.29 V and I=0.6 nA). On the right side: Ball-and-stick-model of the NTCDA-rich phase.

Based on this knowledge about the contrast of the STM image, a ball-and-stick model was established and is shown in Fig. 4.7. The NTCDA-rich phase reveals two CuPc molecules with different orientations to the silver crystal. They are rotated by 20° and 65° to the [-110] direction of the substrate. The NTCDA molecules have (in the NTCDA-rich phase) two different in-plane orientations. Four NTCDAs are aligned at 60° and four NTCDAs are aligned at -45° to the [-110] direction of the substrate. A convincing argument for this molecular orientation is that in this case the oxygen atoms of NTCDA are close to the hydrogen atoms of CuPc as well as to the hydrogens of the neighbouring NTCDA molecules. This allows for the formation of hydrogen bonds between the molecules which enhance the stability of the mixed structure.

Squared NTCDA-rich phase

A further interesting finding is that a different square-shaped NTCDA-rich phase exists simultaneously with the NTCDA-rich phase described above, with the same number and ratio of molecules (see Fig. 4.8 (a)). Unfortunately, there are no spots of this unit cell visible in the LEED images, so that the exact size and shape of the unit cell could not be determined. In the STM image of Fig. 4.8 (b), the squared- as well as the rectangular NTCDA-rich phase are visible. The known structure of the rectangular unit cell enabled us to correct the distortion of the STM image and hence to reveal the unit cell size of the squared phase. It has the dimensions $|\vec{A}| = |\vec{B}| = (32.5 \pm 1)$ Å and an angle of $(90 \pm 2)°$. The unit cells of the squared and the rectangular structures are rotated to each other by 45°. Thus the unit cell of the squared structure is also rotated 45°

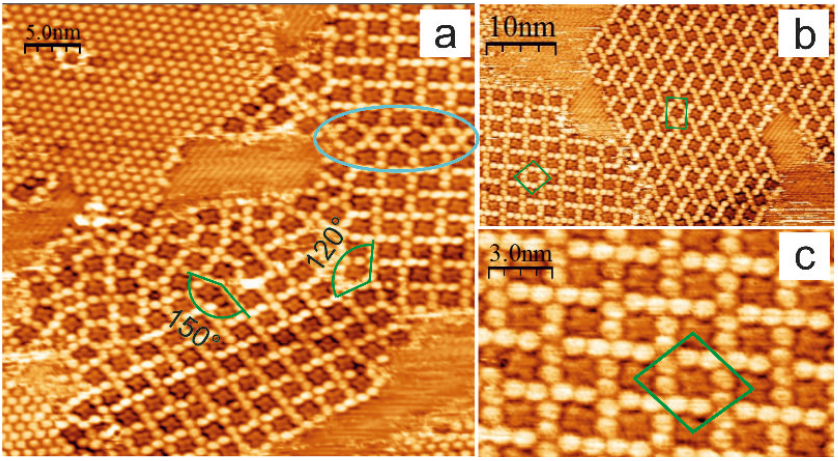

Figure 4.8.: (a) RT-STM image of the squared NTCDA-rich structure (lower and right part of the image) and homomolecular relaxed monolayer structure of NTCDA. The angles of different domains of the squared NTCDA-rich phase are marked in green.(b) STM image with squared and rectangular NTCDA-rich structure. The image was used for the correction of the distortion of the STM images.(c) Magnified part of (b) showing the squared NTCDA-rich structure. All images were measured at U=-1.0 V and I=0.03 nA.

relative to the [-110] direction of the substrate. The orientation of both molecules to the substrate was determined for the squared structure. The molecular orientations are identical within the experimental uncertainty for both unit cells of the NTCDA-rich phase. The magnification of the squared unit cell is displayed in Fig. 4.8 (c) and shows that the CuPc and NTCDA molecules have two different in-plane orientations. In Fig. 4.8 (a) different domains of this phase are visible. The two larger domains on the right side of the image include an angle of 120° which fits to a different high symmetry direction of the (111) surface. In contrast the very small domains in the middle of the image are rotated by 150° to the other domain. This does not fit to the high symmetry directions of the surface. It is however in this area clearly visible that the molecules are more randomly orientated than in the large islands.

The borders between different domains are remarkable, visible in the blue encircled area of Fig. 4.8 (a). Two domains, nucleated at different positions of the sample, are grown together at this border. The border consists of NTCDA molecules which are arranged in circles. Only in every second circle is a CuPc molecule placed. Both domains are identically aligned to the silver surface, thus the formation of the differently ordered border between the domains probably comes from an incommensurate relation between the mixed squared structure and the substrate. When the two domains grow together, the distance between them does not fit for the formation of one well-ordered domain. Therefore a different ordered boarder has to be formed between the two domains.

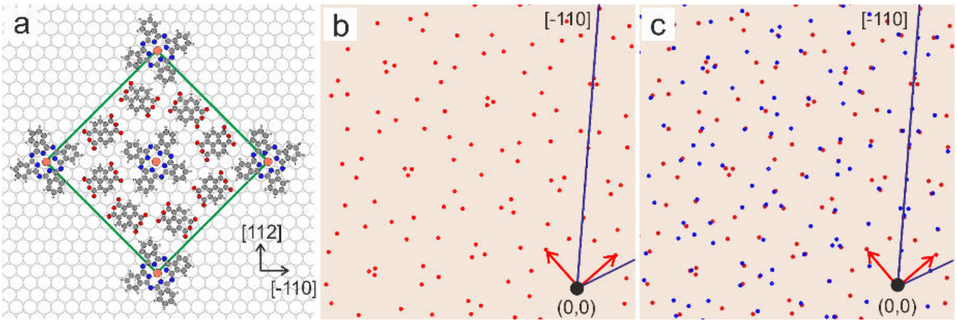

Figure 4.9.: (a) Ball-and-stick model of the squared NTCDA-rich phase. (b) Hypothetical diffraction pattern of this phase. (c) Superposition of the theoretical diffraction patterns corresponding to the squared (red) and experimentally determined rectangular NTCDA-rich phase (blue).

The squared structure was only observed for total coverages of the substrate below one complete monolayer. The unit cell size of the squared phase is around 1060 Å^2, almost identical to the rectangular phase (1042Å^2). The packing density is therefore almost identical. A ball-and-stick model of the squared NTCDA-rich phase is shown in Fig. 4.9 (a).

This unit cell has a incommensurate relation to the substrate with the following matrix:

$$\mathbf{M}_{\text{NTCDA-rich squared}} = \begin{pmatrix} 12.5 & 9.2 \\ -3.4 & 9.2 \end{pmatrix} \tag{4.2}$$

Even under the assumption of large error bars this unit cell is incommensurate. The diffraction pattern of this structure could not be observed by LEED, but due to the knowledge of all parameters of the unit cell, it was simulated by Spot-Plotter as it is shown in Fig. 4.9 (b). In Fig. 4.9 (c) we superimposed the diffraction patterns of the squared (red) and the rectangular NTCDA-rich phase (blue). Surprisingly the diffraction pattern of both structures are very similar. Many spots fit each other and some are close to the spots of the other structure. It is thus difficult to distinguish both diffraction patterns in a conventional LEED. Furthermore, large domains ($\approx$ 700 nm^2) of the rectangular unit cell were observed on the crystal. In contrast only small domains of the squared phase were measured with a size of around 50 nm^2. Due to the similarity of the diffraction patterns and the rare appearance of the squared NTCDA-rich phase on the sample, the diffraction spots are not visible.

B. The intermediate phase

The intermediate phase is visible at a CuPc-coverage between 0.4 and 0.6 ML and a residual NTCDA coverage up to one monolayer. The SPA-LEED image of the intermediate phase, already shown in Fig. 4.4, was simulated by Spot-Plotter. This SPA-LEED pattern could not be explained by one superstructure alone. The image contains spots from two different structures. The superstructure simulated in red in Fig. 4.10, called IM1, has an almost rectangular shape with an angle between the unit vectors of (90.7 ± 0.4)°. The vector length corresponds to $|\vec{A}| = (23.6 \pm 0.1)$ Å and $|\vec{B}| = (32.6 \pm 0.1)$ Å. This mixed phase IM1 has a uniaxial commensurate correlation with a superstructure matrix of

$$\mathbf{M}_{\mathrm{IM1}} = \begin{pmatrix} 7 & 13 \\ 8 & -0.3 \end{pmatrix}. \tag{4.3}$$

The second simulated diffraction pattern which is visible in the SPA-LEED image in blue (IM2) has the same unit cell shape and size within the error bars. The unequal diffraction pattern stems only from different in-plane orientations of the unit cell to the substrate. The short vector of the unit cell of the IM1 structure is however rotated by 2.5° to the [-110] silver direction while it is rotated by -4.5° for the IM2 phase. The matrix of this superstructures is:

$$\mathbf{M}_{\mathrm{IM2}} = \begin{pmatrix} 5.4 & 13 \\ 8.6 & 1 \end{pmatrix} \tag{4.4}$$

The simulated superstructure of IM2 does not cover all spots of the measured diffraction pattern perfectly, but a simulation with a better overlap could not be achieved. In the following STM measurements, only one mixed structure could be observed (see

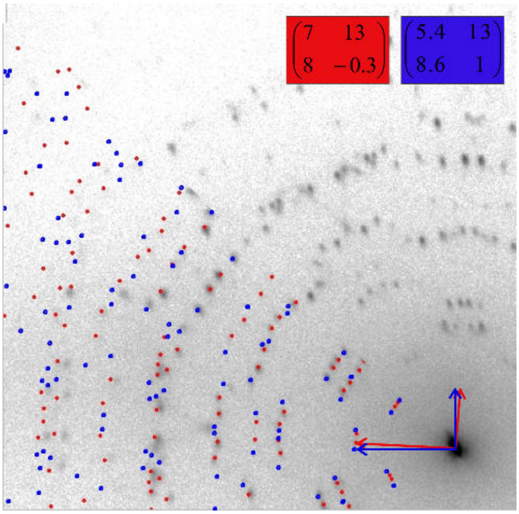

Figure 4.10.: SPALEED image of the intermediate phase at 27.2 eV. The two simulated superstructures are indicated by red (IM1) and blue spots (IM2). Their corresponding superstructure matrices are shown in the same colours.

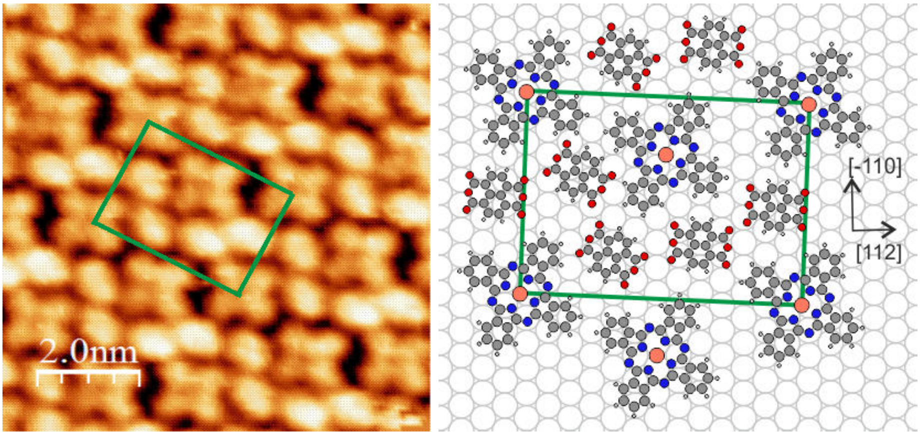

Figure 4.11.: On the left side an STM image of the intermediate phase at U=-2.8 V and I=0.02 nA with the unit cell known from SPALEED, represented in green. On the right side the corresponding ball-and-stick model of the unit cell.

Fig. 4.11). This reflects the IM1 as well as the IM2 structure. The STM measurements were performed in order to determine the molecular orientation. The ball-and-stick model plotted in Fig. 4.11, obtained from the STM image displayed next to it, shows the IM1 structure. The model of the IM2 structure has identical molecular orientations and positions, only the orientation to the substrate would be slightly rotated. The unit cell contains two CuPc- and four NTCDA molecules. The area ratio of CuPc to NTCDA is however 1:1. The CuPc molecules have in this phase, in contrast to the NTCDA-rich phase, just one molecular orientation rotated by 20° to the [-110] direction. This agrees with the orientation of one of the molecules in the NTCDA-rich phase. The determination of the alignment of the NTCDA molecules is however more complicated due to the almost square shape of the molecules. For the determination of the molecular orientation of the NTCDA molecules, STM images recorded with a similar bias were considered where the homomolecular relaxed monolayer structure of NTCDA and the NTCDA-rich phase are visible, as it is the case Fig. 4.6. As the molecular orientation of NTCDA in the RML of NTCDA is known, it can be determined that the long axis in the STM contrast represents the long axis of the molecules. We obtain therefore the following orientation angles for the NTCDA molecules for the IM phase: 55° and 85° to the [-110] direction. The error bar of these angles are at least 10°.

C. The annealed intermediate phase

A second intermediate phase arises when the relaxed monolayer structure of NTCDA with CuPc adsorbed in the second layer is annealed to 550 K. During the annealing, NTCDA molecules desorb and the CuPcs diffuse into the first layer and form a mixed structure with the remaining NTCDA molecules. This mixed structure was also formed

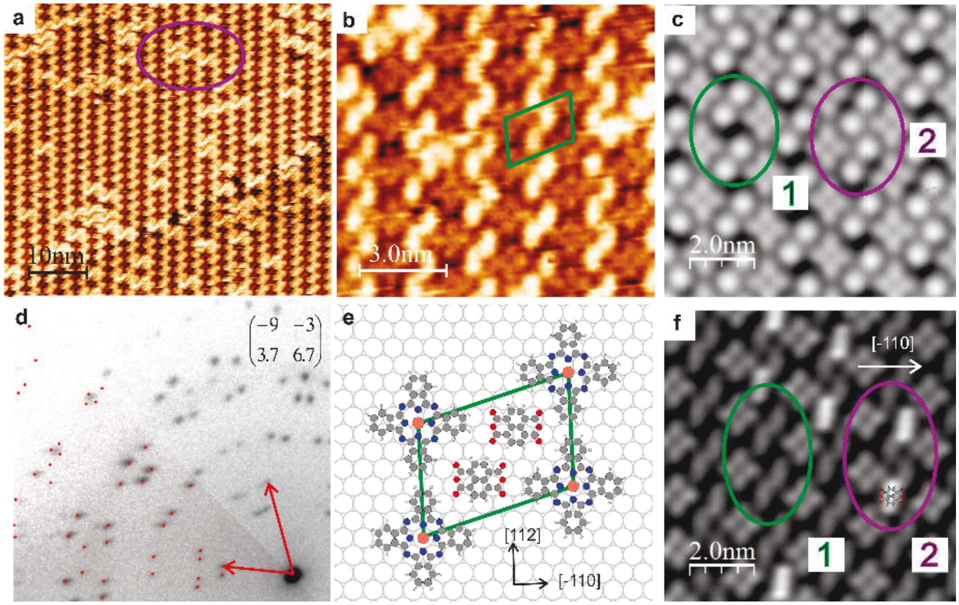

Figure 4.12.: (a) STM image of the annealed intermediate phase (U=−1.0 V and I=0.02 nA) at RT. The purple ellipse marks NTCDA molecules which are differently ordered between the mixed structure. (b) A distortion corrected magnified part of (a). The unit cell is shown in green. (c) STM image of the same structure at 5 K (U=1.5 V and I=0.2 nA). The green ellipse marks the commonly separated NTCDA pairs (called 1) of the annealed IM phase and the purple ellipse indicates the differently ordered NTCDA areas (called 2). (d) SPA-LEED image of the annealed intermediate phase, measured at 27.2 eV, with the simulated diffraction pattern displayed by red spots. (e) Ball-and-stick model of the structure. (f) Constant height image at LT for the determination of the in-plane orientation of the NTCDA molecules at 100 mV.

with 0.6 ML NTCDA deposited on 0.6 ML of CuPc on Ag(111), but also only after annealing to 550 K. The unit cell size and shape of this structure was again determined from the SPA-LEED images using Spot-Plotter. The result is shown in Fig. 4.12 (d) where the red simulated spots belong to the unit cell with

$$\mathbf{M}_{\text{Annealed-IM}} = \begin{pmatrix}-9 & -3\\ 3.7 & 6.7\end{pmatrix}. \tag{4.5}$$

The vectors have a length of $|\vec{A}| = (16.8 \pm 0.1)$ Å and $|\vec{B}| = (22.9 \pm 0.1)$ Å. The vectors include an angle of $(112.6\ \pm 0.4)^\circ$.

The room temperature STM images in Fig. 4.12 (a) and (b) were corrected for distortion using the exact parameters of the unit cell. The lateral structure is identical at 5 K as shown in Fig. 4.12 (c). This enables us to sketch a lateral structure model, based on a ball-and-stick model. The unit cell contains one CuPc- and two NTCDA molecules as shown in Fig. 4.12 (c). It has the same stoichiometric ratio as the intermediate phase, but only half the number of molecules. The CuPc molecules are aligned with their lobes along the [-110] substrate direction. In the constant height STM image recorded at 5 K, shown in Fig. 4.12 (f), the in-plane orientation of the NTCDA molecules is clearly visible, as the electronic contrast is enhanced above the hydrogen atoms of the molecule, as it was already observed for LT-STM images of the NTCDA-rich phase with a similar bias. The long axis of the NTCDA molecules is thus aligned parallel to the [-110] substrate direction. Between the mixed structure however differently ordered areas are visible as seen in the STM image in Fig. 4.12 (a), (c) and(f), marked by purple ellipses. Four NTCDAs are located in one row as marked in area two in Fig. 4.12 (c)) compared to area one (green), where two NTCDAs are separated by a small gap. These modified areas are visible in all islands of the annealed-IM structure at RT and LT, but without a certain periodicity. The number of these areas was determined from the 100 nm^2 STM image in Fig. 4.12 (a). The result is that 15 % of the NTCDA pairs are differently ordered. The reason for this arrangement is not known, but the first and fourth NTCDA in these rows have a different electronic contrast than the other NTCDAs, as shown in the constant height image in Fig. 4.12 (f). This finding will be discussed in the next section.

The packing densities of the annealed and non annealed IM phases differ significantly: The annealed structure has a unit cell size of 355.7 Å, while the non-annealed structure with double the number of molecules has 767 Å $= 2 * 383.5$ Å. The packing density of the annealed structure is thus larger by 8 %. This proves that annealing enables the molecules to arrange in a denser configuration than in the non-annealed intermediate phase. This is also visible in the STM images of the two phases (compare Fig. 4.11 and Fig. 4.12 (b)), where a large distance exists between the CuPc molecules.

The uniaxial commensurate relation to the Ag(111) substrate of both structures excludes that the denser packing of the annealed IM structure arises due to more energetically favourable adsorption sites of the molecules in the annealed IM phase. The potential energies of both geometries are probably located in local minima of energy, separated by a potential barrier. Annealing allows the molecules to overcome this barrier and leads to the formation of the denser packed annealed IM structure. This assumption can however only be verified by pair potential calculations for both unit cells, which was not done in this work due to time constraints.

A striking fact is that the unit cell shape, size and its molecule number and ratio of the annealed intermediate phase is very similar to the Mixed Brick Wall structure of PTCDA and CuPc (see 4.1 (a)). The unit cell of the Mixed Brick wall structure also includes one CuPc molecule and two parallelly aligned PTCDA molecules instead of NTCDA. The in-plane orientation of PTCDA is however different than for the NTCDA molecules. The PTCDA molecules are rotated by 30° in contrast to the NTCDA molecules which are aligned parallel to the [-110] substrate direction. Since NTCDA is 20 % smaller than PTCDA, the NTCDA and CuPc molecules can arrange in a unit cell which is 20 % smaller than the Mixed Brick Wall phase.

This leads to the loss of the commensurate relation between the molecules and the substrate which is present for the PTCDA-rich phase while the NTCDA phase exhibits a weaker uniaxial commensurate relation.

D. The CuPc-rich phase

The CuPc-rich phase consists of $\Theta_{CuPc} \geq 0.6$ ML and $\Theta_{NTCDA} \leq 0.4$ ML. First the diffraction pattern, recorded by SPA-LEED of the CuPc-rich phase shown in Fig. 4.4, was analysed in detail. The result is presented in Fig. 4.13 (a) where the simulation of

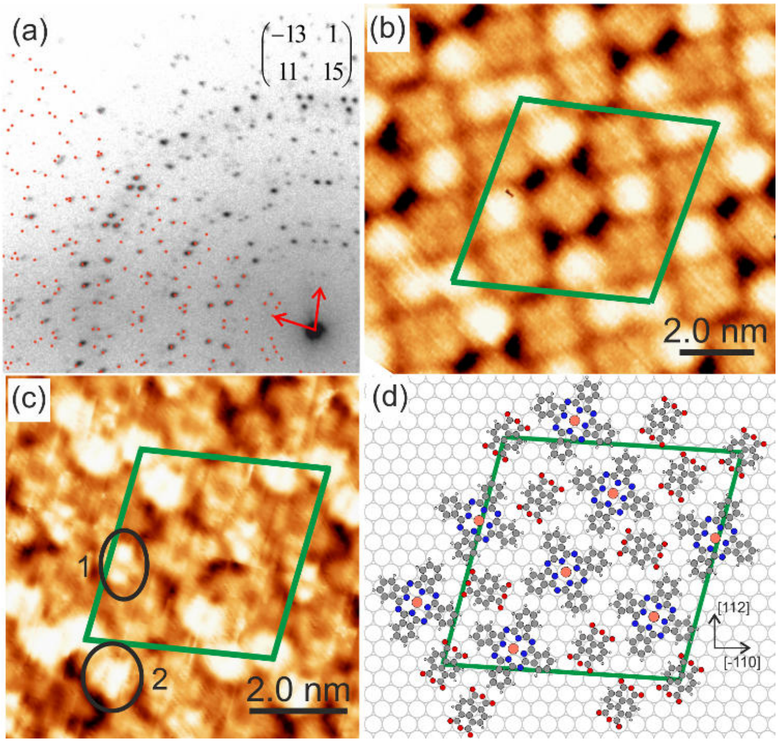

Figure 4.13.: (a) SPALEED image of the CuPc-rich phase at 27.2 eV. The red dots indicate the position of the simulated superstructure relation. (b) STM image of the CuPc-rich structure at U=-2V and I= 0.03 nA and in (c) at U=-1V and I= 0.03 nA. The ellipses mark the two orientations of the NTCDA molecules (d) Ball-and-stick model of the CuPc-rich structure based on the STM images. The green rhomboid indicates the unit cell shape and size.

the diffraction pattern is plotted by red dots. The outcome of this is a commensurate superstructure with the matrix

$$\mathbf{M}_{\text{CuPc-rich}} = \begin{pmatrix} -13 & 1 \\ 11 & 15 \end{pmatrix} . \tag{4.6}$$

This unit cell is almost nine times larger than the unit cell of homomolecular structure of NTCDA with an area of 1490 Å^2. The unit cell vectors have a length of $|\vec{A}| = (39.1 \pm 0.1)$ Å and $|\vec{B}| = (38.9 \pm 0.1)$ Å. The vectors include an angle of $(101.4 \pm 0.4)^\circ$. In the SPA-LEED pattern some spots are weakly visible which are not included in the simulated structure. These probably belong to the intermediate phase which is present on small areas of the substrate. Due to the large size of the unit cell, the number of molecules inside the unit cell can not be obtained by SPA-LEED, but STM measurements are necessary. Hereby we found three different CuPc- rich structures, but at first we discuss the most prominent structure, which was found on large terraces (500 nm^2) and was determined by SPA-LEED.

First the unit cell of the superstructure known from SPA-LEED is analysed. The corresponding STM images are shown in Fig. 4.13 (b) and (c). The unit cell is highlighted in green. This unit cell contains six NTCDA and five CuPc molecules. In Fig. 4.13 (d) a ball-and-stick model of the structure, based on the STM images, is displayed. Four of the five CuPc molecules are rotated by 20° to the [-110] direction with an error bar of 5°. The fifth CuPc molecule, in the centre of the unit cell, is oriented at $65^\circ \pm 5^\circ$ to the [-110] direction. Interestingly, these are the same orientations as for the NTCDA-rich and the intermediate phase. In addition, two orientations of NTCDA molecules, assigned by 1 and 2, can be found in the STM image in Fig. 4.13 (c). The electronic contrast of the NTCDA molecules differs compared to the STM image shown in Fig. 4.13 (b), as the applied bias was changed to -1 V. As already mentioned, the electronic contrast of the LUMO in the homomolecular structure of NTCDA (located at -0.2 eV) has its intensity maxima above the hydrogen atoms of NTCDA. Although the applied bias is 0.8 V lower in Fig. 4.13 (c), it could be possible that a particle is attached to the tip, which leads to the LUMO-like contrast [KWW$^+$11]. For the two NTCDA molecules of type 1 the intensity maxima are clearly visible and thus these molecules are rotated by -20 ° to the [-110] direction. The intensity maxima for the NTCDAs of type 2 are difficult to determine. The adjustment of the NTCDAs between the CuPc molecules in the ball-and-stick model revealed that they are probably aligned by $60^\circ \pm 10^\circ$ to the [-110] direction. An additional indication for this orientation is that the oxygen atoms are always close to hydrogen atoms of CuPc or NTCDA and can therefore form hydrogen bonds.

As mentioned before, more than one CuPc-rich structure was observed. The other two mixed patterns were found only on smaller terraces and are displayed in Fig. 4.14. Unfortunately, the STM images of these structures could not be precisely corrected as the unit cells are not known from (SPA)-LEED.

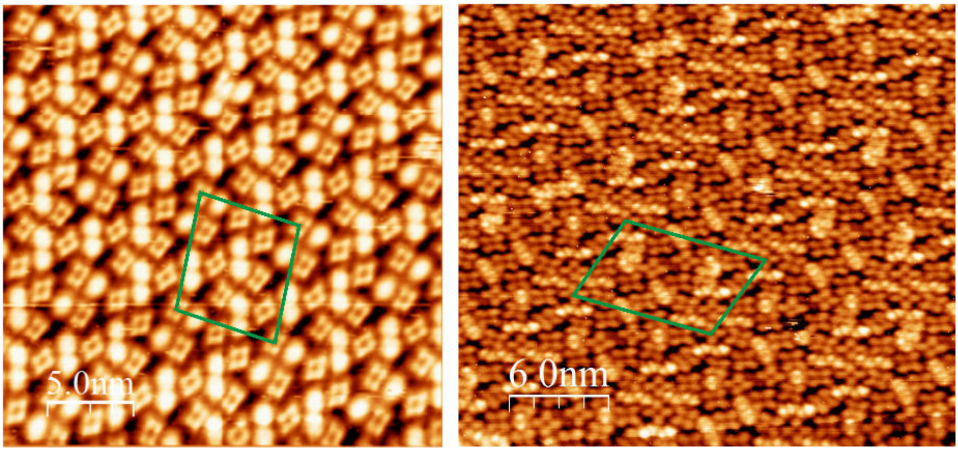

Figure 4.14.: STM images of a second (U=-2.0 V and I=0.03 nA) and third (U=-1.0 V and I=0.03 nA) CuPc-rich structure with their corresponding unit cells in green.

The first of these additional structures is shown on the left side of Fig. 4.14. Its unit cell vectors were estimated to be $|\vec{A}| = (58 \pm 5)$ Å and $|\vec{B}| = (66 \pm 5)$ Å, with an included angle of $(97 \pm 5)°$. The area is therefore 3860 Å^2, more than twice as large as the first CuPc-rich phase. The orientation of the molecules to the substrate was not determined as neither bare crystal areas were detectable nor boundaries to the first CuPc-rich phase, known from SPA-LEED, were observed. Two differently rotated CuPc molecules were found. They are rotated by approximately 20° to each other. The orientation of the NTCDA molecules could not be determined due to its square shape. The ratio of molecules was however determined precisely. The unit cell contains eight CuPc- and NTCDA molecules. This corresponds to an area ratio of NTCDA to CuPc of 0.42. This shows that the coverage ratio of CuPc is larger in the second CuPc-rich phase than in the first (0.54).

Only small domains of the third CuPc-rich phase were observed, shown on the right side of Fig. 4.14. This unit cell has the dimensions of $|\vec{A}| = (51 \pm 5)$ Å and $|\vec{B}| = (85 \pm 5)$ Å. The vectors include a angle of $(109 \pm 5)°$. In this unit cell we count sixteen CuPc- and fourteen NTCDA molecules, although the unit cell is just 12 % larger than the second CuPc-rich phase. The ratio of CuPc : NTCDA molecules is with 7:8 similar to the second CuPc-rich phase with 8:8. The similar size of the unit cell with almost twice the number of molecules indicates that the third CuPc-rich phase is more densely packed than the second CuPc-rich phase. The STM images confirm this finding due to large gaps between the molecules in the second structure. The area ratio of NTCDA to CuPc molecules in this unit cell is 0.4. This allows for the conclusion that a higher coverage ratio of CuPc to NTCDA leads to an increased size of the unit cell.

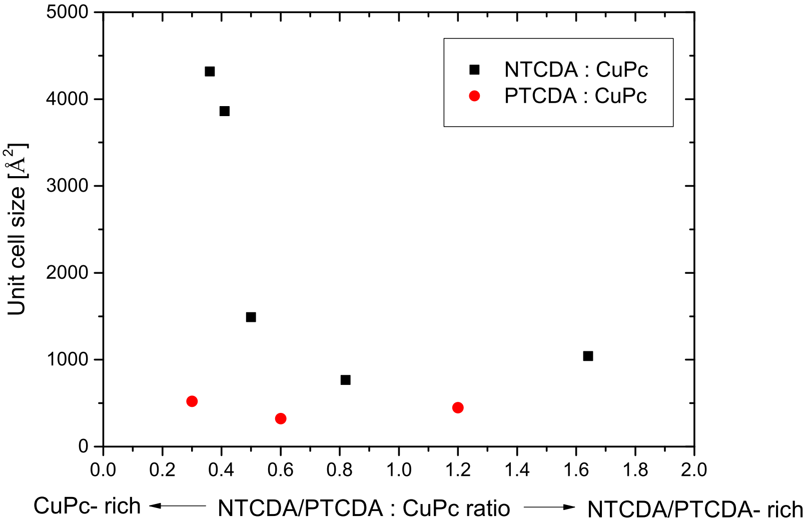

Figure 4.15.: Unit cell size of all NTCDA/CuPc (black) and PTCDA/CuPc (red) heterostructures versus the NTCDA/PTCDA to CuPc ratio.

Although the orientation of the molecules to the substrate could not be determined due to the unknown substrate relation, three differently rotated CuPc molecules were observed. The CuPc molecules are rotated 30° and 60° to each other. In addition three NTCDA molecules are contained in this unit cell. They have relations of 115° and 150° to the first NTCDA molecule.

4.3.2. Comparison of the lateral structures

Many different coverage dependent non-annealed mixed phases, three CuPc-rich, two differently rotated intermediate and a rectangular and square shaped NTCDA-rich phase, were observed in SPA-LEED and STM. In the regime of the intermediate phase additionally an annealed structure with the same molecular ratio was found, but the annealed structure has only half the number of molecules than the non-annealed structure leading to different unit cell sizes. All these structures have surprisingly large unit cells, up to eight times larger than for example that of the homomolecular structure of NTCDA. In Fig. 4.15 the unit cell size of all mixed phases is plotted versus the NTCDA to CuPc area ratio. The areas of the molecules in the densest packed homomolecular structures of NTCDA and CuPc ($A_{NTCDA} = 78.7$ Å^2 and CuPc of $A_{CuPc} = 191.6$ Å^2) were used as references due to missing information about the area of the molecules in the heteromolecular systems. These areas were multiplied by the number of molecules in the heteromolecular structures and their ratio was determined. From investigations of CuPc and PTCDA mixed films, where the molecules arrange in unit cells with a smaller size, as shown by red dots in Fig. 4.15, we expected that the smaller NTCDA molecule would lead to smaller unit cells with CuPc. However this is not the case; instead the unit cell size is up to three times as large for the CuPc- and NTCDA-rich phase in comparison to the PTCDA - CuPc heterostructures. An overview of all NTCDA-CuPc and PTCDA-CuPc heterostructures is given in Tab. 4.1. The number of molecules, the area ratio of NTCDA to CuPc, the unit cell size and the matrix of the superstructures is listed. The different structures are discussed in the following subsection. In particular, the finding that the CuPc- and NTCDA-rich structures have, in contrast to the smaller intermediate phase, a commensurate relation to the substrate. Additionally, the NTCDA-CuPc and PTCDA-CuPc heterostructures are compared with each other.

The formation of a commensurate CuPc-rich structure is astonishing because of the known repulsive interaction between CuPc molecules, which leads in homomolecular CuPc films and mixed PTCDA-CuPc heterostructures (e.g. the One-to-One and the Zig-Zag phase) to incommensurate substrate relations. The molecules in these phases can only arrange themselves into commensurate structures by additional annealing of the crystal. This causes desorption of CuPc molecules from the surface which leads to increased space for each remaining molecule. Furthermore an expansion of the unit cell occurs in order to minimize the pair potential energy [Sta13].

Three fundamental differences can be identified between the CuPc-rich NTCDA+CuPc and the mixed Zig-Zag PTCDA+CuPc phase:

- NTCDA is, in comparison to PTCDA, a weaker electron charge acceptor which leads to a weaker interaction with the Ag(111) substrate [SWR+12], [BFS+07].
- The CuPc ratio is lower in the CuPc-rich phase (Tab. 4.1), which leads to fewer contacts between neighbouring CuPc molecules.
- The establishment of hydrogen bonds between the molecules is expected to stabilize molecular structures [Tau07]. NTCDA has however a smaller size than PTCDA and does not fit into a square of four CuPc molecules as PTCDA does. The distance between the NTCDA and CuPc molecules would be too large for hydrogen bonds to arise.

In the following I discuss these three aspects:

The similar CuPc coverage of the structures indicates that the repulsive intermolecular interaction dominates the structure formation of the CuPc-rich phase as well. The molecules arrange themselves into a commensurate structure without any annealing, simply by arranging into an almost three times larger unit cell in comparison to the Zig-Zag phase. A reason for this could be the weaker interaction between the NTCDA molecules, in comparison to PTCDA molecules, with the Ag(111) crystal. It is known from UPS measurements that the frontier orbitals (HOMO and LUMO) of PTCDA have a higher binding energy than the corresponding orbitals of NTCDA on the Ag(111) crystal [SWR+12], [BFS+07] and PTCDA has in comparison to NTCDA a lower adsorption height on Ag(111) [SHS+07], [HKC+05]. This indicates a weaker binding of NTCDA to the substrate. The ratio between intermolecular and molecule-substrate interaction is thus increased in comparison to the PTCDA-CuPc heterostructures. This became especially clear when PTCDA molecules we deposited first grew in islands and CuPc molecules were added afterwards. Annealing is necessary to dissolve the strongly bonded PTCDA molecules in the homomolecular islands. For NTCDA + CuPc the molecules arrange themselves in mixed islands even at room temperature.

The next point is a higher NTCDA to CuPc coverage ratio of 0.54 in the CuPc-rich phase, in comparison to 0.3 for the PTCDA-CuPc heterostructures. This leads to a reduced number of contacts between neighbouring CuPc molecules. Fewer boundaries are energetically favourable due to the repulsive interaction between the molecules. This enables the molecules to form more CuPc-NTCDA interfaces relative to PTCDA-CuPc. These boundary surfaces between the molecules seem to be energetically favourable due to the attractive interaction between the molecules.

Two further CuPc-rich phases (2 and 3) have been observed on small terraces which in fact have even a 2.5 and almost 3 times larger unit cell than the first CuPc-rich structure. Both unit cell sizes are displayed in Fig. 4.15. The reason for the drastic increase of the unit cell size is probably also the increased number of contacts between the CuPc molecules. These appear due to a decreased NTCDA to CuPc ratio in these structures; the second CuPc-rich phase has a ratio of 0.4 and the third CuPc-rich phase of 0.35 compared to the first CuPc-rich phase, with a ratio of 0.5. The increased number of contacts between CuPc molecules leads to a stronger repulsive interaction between the CuPcs and can only be compensated by an expansion of the unit cell. The molecular coverage ratio can however not be the only reason for the huge unit cell size, as the Zig-Zag phase of CuPc-PTCDA has a molecular coverage ratio of 0.3 and nevertheless forms a unit cell almost three times smaller (see Tab. 4.1). Unfortunately, the relation between the molecules and the substrate is not known for the second and third CuPc-rich phases. We therefore can not glean further information as to whether the higher amount of CuPc contacts leads to an incommensurate structure or if it remains commensurate due to the enormous extension of the unit cell.

The third point is the smaller size of NTCDA in comparison to PTCDA. For PTCDA-CuPc heterostructures, unit cells with at most three molecules were observed [Sta13]. This is also the case on Cu(110) and Cu(111), where a stronger interaction between the substrate and the molecules exists [BWBM03],[CSS+12]. The unit cell sizes are very similar to the ones formed on the silver substrate. Heterostructures consisting of fluorinated CuPc (F16CuPc) - pentacene (PEN) and CuPc - perfluoropentacene (PFP) arrange on Au(111), Ag(111) and Cu(111) into unit cells containing only a few molecules [ESBG+13]. PEN and PFP consist of five linearly bound benzene rings and are therefore of a similar size compared to PTCDA molecules. The similar unit cell sizes are independent from the substrate, which indicates that the size of the molecule influences the periodicity of the mixed layers more strongly than an altered substrate-molecule interaction.

The interplay between the changed molecular interaction and the reduced substrate-molecule interaction thus leads to the formation of large commensurate unit cells. The smaller size of the NTCDA molecules could hinder the CuPc and NTCDA molecules, in the NTCDA- or the CuPc-rich phase on Ag(111), from arranging into a densely packed configuration with a unit cell size similar to previously investigated heterostructures. The molecules therefore have to arrange into very large unit cells to keep their commensurate substrate relation and maintain minimal contacts between repulsively interacting CuPc molecules (and maximal interfaces between CuPc and NTCDA) at the same time.

The NTCDA-rich phase has a commensurate relation to the silver substrate as well. The commensurate substrate relation is probably the reason for the sextupled unit cell size in comparison to the RML of NTCDA. It was found earlier that NTCDA molecules form commensurate superstructures on gold, silver and copper surfaces [Fin99]. The molecules arrange in superstructures with a different density so to keep their commensurate relation. The authors explained this fact by assuming a strong molecule-substrate interaction. This interaction strength increases, however, from gold to silver to copper crystals [DGS$^+$07]. It is known that on silver and gold the interaction is already quite weak. This argumentation is therefore only valid for the strongly interacting copper substrate [SKRK11], [KSK$^+$11] and maybe partly for the silver crystal [LH02]. It is however known that for many molecules on gold only incommensurate superstructures are formed due on the weak molecule-substrate interaction [KUS06], [MTSH$^+$01]. Fournier et al. showed by STS that the LUMO of NTCDA on Au(111) is not filled, despite a commensurate substrate relation [Fou14]. Thus, the commensurate superstructures of NTCDA on various substrates can not only arise due to a strong molecule - substrate interaction.

In the case of the NTCDA-rich phase, the enlarged unit cell size probably allows the integration of two CuPc molecules and the adherence of the commensurate correlation. The strong similarity with the homomolecular structure of NTCDA, the sextupled unit cell size with the same alignment to the Ag(111) surface, leads to the assumption that the structure formation is dominated by the NTCDA molecules. The mixed Brick Wall structure (PTCDA-rich phase) does not have much in common with this phase, probably because of the much larger NTCDA to CuPc ratio of 1.65 in comparison to the PTCDA to CuPc ratio of 1.2. The only similarity between the NTCDA- and PTCDA-rich phase is the commensurate registry with the substrate, as already mentioned.

The intermediate phase (IM) of NTCDA and CuPc is the only NTCDA-CuPc heterostructure with a uni-axial commensurate correlation between the molecules and the substrate. The unit cell of this phase exists with two different rotation angles relative to the substrate. The IM1 is rotated by 2.5° and IM2 by -4.5° to the [-110] direction of the silver substrate. Furthermore the unit cell size of the intermediate phase is just slightly larger in comparison to the PTCDA-CuPc heterostructures. A reason could be that this configuration is the only possible one in which the molecules can form a densely packed structure with many contacts between CuPc and NTCDA. CuPc molecules form zig-zag rows with four NTCDA molecules in between. The structure is similar to the Zig-Zag phase of PTCDA-CuPc heterostructures, however there is only one PTCDA molecule between the CuPc rows. In this configuration the molecules can form many contacts between CuPc and NTCDA molecules, but are displaced from their commensurate substrate sites. This therefore leads to the conclusion that the total energy gained by densely packed NTCDA-CuPc contacts is larger than the reduction of energy which is caused by the loss of the commensurate bonding sites of the molecules.

In addition, an annealed intermediate phase was observed with half the number of molecules, two NTCDA and one CuPc, as in the non-annealed intermediate phase. Both phases have however a uni-axial commensurate registry with the substrate, but the annealed phase is more densely packed than the non-annealed structure. This leads to the conclusion that the additional thermal energy allows the molecules to arrange into a denser structure by overcoming a potential barrier which separates the energetic minima of both intermediate phases.

All mixed NTCDA-CuPc phases have some aspects in common. In every non-annealed phase, the CuPc molecules have the same two in-plane orientations with a rotation of 20° and 65° to the [-110] direction of the silver substrate. This differs from the PTCDA-CuPc heterostrucutres, where one pair of wings of the CuPc molecules is always almost aligned with a substrate row. The NTCDA molecules however have very different orientations in contrast to CuPc. They are usually rotated so that the formation of O-H bonds between the oxygen atoms of NTCDA and the hydrogen atoms of CuPc is possible.

In conclusion, the NTCDA-CuPc heterostructures grow in larger unit cells compared to PTCDA-CuPc blends. This is probably caused by the weaker molecule-substrate interaction between the NTCDA molecules and the Ag(111) surface and the smaller geometric size of NTCDA in comparison to PTCDA. Due to the former the molecules have a higher mobility and can adsorb at their optimum adsorption sites, which is a commensurate relation to the substrate.

NTCDA-CuPc Phases	Ratio of NTCDA:CuPc	Area ratio NTCDA:CuPc	Area unit cell [Å^2]		Matrix
			LEED	STM	
NTCDA-rich	8:2	1.65	1041.6		$\begin{pmatrix} 8 & 0 \\ 9 & 18 \end{pmatrix}$
NTCDA-rich square	8:2	1.65		1089	
Intermediate	4:2	0.82	767		$\begin{pmatrix} 7 & 13 \\ 8 & -0.3 \end{pmatrix}$
Intermediate 2	4:2	0.82	770		$\begin{pmatrix} 5.4 & 13 \\ 8.6 & 1 \end{pmatrix}$
Annealed Intermediate	2:1	0.82	356		$\begin{pmatrix} -9 & -3 \\ 3.7 & 6.7 \end{pmatrix}$
CuPc-rich	6:5	0.54	1490		$\begin{pmatrix} 13 & -1 \\ 11 & 15 \end{pmatrix}$
CuPc-rich 2	8:8	0.42		3860	
CuPc-rich 3	14:16	0.40		4318	
PTCDA-CuPc Phases	Ratio of PTCDA:CuPc	Area ratio PTCDA:CuPc	Area unit cell [Å^2]		Matrix
			LEED	STM	
Brick Wall	2:1	1.2	448		$\begin{pmatrix} 8 & -2 \\ 3 & 7 \end{pmatrix}$
One-to-One commensurate	1:1	0.6	333		$\begin{pmatrix} 6 & -1 \\ 4 & 7 \end{pmatrix}$
Zig-Zag	1:2	0.3	520		$\begin{pmatrix} 7.6 & 0.3 \\ 1.7 & 9.3 \end{pmatrix}$

Table 4.1.: Overview of the unit cells of all NTCDA-CuPc and PTCDA-CuPc heterostructures‘. The number of molecules, the area ratio, the unit cell size and the matrix of the superstructure are given.

4.4. Vertical geometry of mixed CuPc + NTCDA films

In ordered heteroorganic films the vertical geometry is influenced by the lateral interaction between the molecules. Investigating these systems reveals information about the influence of the formation of mixed films on the bonding strength of each molecule to the substrate in comparison to in its homomolecular structures. The normal incidence X-ray standing wave technique enables us to perform a systematic study of the vertical geometry of different stoichiometric structures of NTCDA + CuPc on Ag(111). The comparison of these findings with the adsorption heights of the molecules in the homomolecular systems allows for a deeper understanding of the heteromolecular-metal interactions.

In this section, the core level analysis is performed for the NTCDA-rich and the CuPc-rich phase at room temperature and 60 K. The development of an appropriate fitting model and the separation of different chemical bound species of both molecules was done by CasaXPS and leads to the extraction of corresponding yield curves. These curves were subsequently fitted by a least square fit, which allows for the determination of the coherent position and fraction of each species. The resulting adsorption heights for both mixed NTCDA-CuPc heterostructures are discussed in relation to each other. These findings are thereafter compared with heteromolecular structures, consisting of PTCDA and CuPc, and homomolecular systems measured at low temperatures.

4.4.1. The NTCDA-rich phase

A. Core level model at room temperature

To determine the adsorption height of both molecules in the mixed films, at first models from statistically acquired photoelectron spectra of carbon C1s and oxygen O1s were established using CasaXPS. For nitrogen N1s and coper Cu2p, these spectra were not measured. The XPS spectra of C1s and O1s and exemplary XPS spectra of a XSW scan of Cu2p and N1s are shown in Fig 4.16.

For comparison with the homomolecular structures of NTCDA and CuPc the XPS spectra of the heteroorganic structures have to calibrated to an absolute energy scale. For the calibration, we have chosen the Ag3d region where two sharp peaks (Ag3d$_{3/2}$ and Ag3d$_{5/2}$) arise, clearly separated from each other. The Ag3d spectrum was only measured at the beginning of our beam time, therefore the spectra of the different phases are shifted partly by values of up to 0.2 eV. This effect does not matter so much as the relation of the peaks to each other is the most important quantity in our fitting models.

The N1s and Cu2p spectra show a contribution from the CuPc molecules only and the O1s spectrum from the NTCDA molecules, but with two chemically different bound oxygen atoms, a carboxylic and an anhydride type. In contrast, the C1s spectrum con-

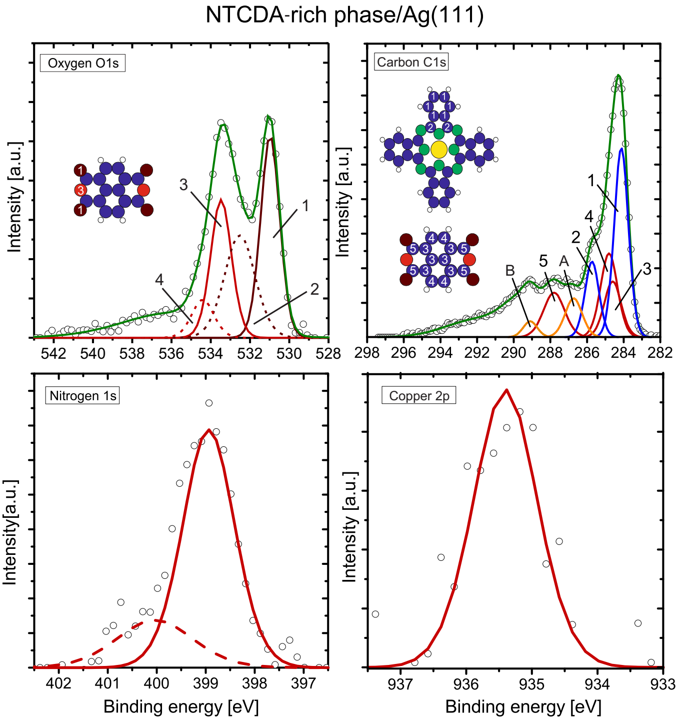

Figure 4.16.: Upper part: Background subtracted XPS spectra of the O1s and C1s with their corresponding fitting models of the NTCDA-rich phase recorded off Bragg. Lower part: A N1s and Cu2p XPS spectra of a XSW scan.

tains contributions from both molecules. The spectra of all species contain a background which originates from inelastically scattered photoelectrons. It is very important to fit this background properly due to the fact that this influences the peak area strongly. It can be described in general in the best way by a Shirley function, but this will be discussed in more detail for the different fitting models later.

The Cu2p and N1s spectra contain just one component and can therefore be fitted by a Voigt function with 30% Lorentzian contribution after a proper consideration of the background signal. The Cu2p spectrum has its maximum at a binding energy of 935.1 eV. The N1s peak arising from CuPc molecules (E_B= 389.6 eV) is superimposed with a further peak from an N1s satellite. The satellite is displayed at a 1.1 eV higher binding energy by a dotted red line in Fig. 4.16.

The O1s signal is split into two main peaks (see Fig. 4.16). The peak at a binding energy of 530.7 eV stems from the carboxylic oxygen atoms (peak 1) and the other, shifted to higher binding energies (at 531.1 eV), from the anhydride oxygen atoms (peak

O1s species	$E_b[eV]$	FWHM [eV]	Intensity [%]
Carboxylic Oxygen Main Line (1)	530.7	1.3	29
Carboxylic Oxygen Satellite (2)	530.7 + 1.4	1.4	25
Anhydride Oxygen Main Line (3)	530.7 + 2.4	1.2	24
Anhydride Oxygen Satellite (4)	530.7 + 3.3	1.9	7
Energy Loss Satellite	530.7 + 5.65	5.0	14

Table 4.2.: The binding energy E_b, the FWHM, and the relative area of the peaks in the fitting model used for the O1s core level spectrum of NTCDA.

3). Moreover, both components have a satellite (peak 2 and 4) shifted to higher binding energies, which is typical for photoelectron spectra of weakly chemisorbed molecules [Ohn94]. The model from Schöll et al. [SZS+04] of the relaxed monolayer of NTCDA was modified for the fitting, where the carboxylic and anhydride peak are separated by a binding energy of 2.2 eV from each other. In our adapted model for the NTCDA-rich phase, the peaks were separated by 2.4 eV. The slightly-changed binding energies can arise from the different chemical environment in the NTCDA-rich phase compared to the homomolecular structure. In addition the satellites are at almost the same distance to the corresponding main lines as in the model of the RML of NTCDA. The tail at higher binding energies arises from inelastically scattered electrons of both species and is fitted by a further peak. For a reasonable fit, the area ratio of the carboxylic main peak plus its satellite to the anhydride oxygen peak plus satellite should be 2:1. The area and width of the satellites have to be constrained to their main peaks. The best fitting model for the O1s spectrum of the NTCDA-rich phase was achieved with the values and constraints shown in table 4.2.
The C1s spectrum, shown in Fig. 4.16, is more complicated to fit as it contains carbon species of NTCDA (red peaks) and of CuPc (blue peaks). The model of the carbon species belonging to the NTCDA molecule is also adapted from the model of Schöll et al. [SZS+04]. Their spectrum contains four main carbon peaks and many satellites. In our case two of the main peaks of NTCDA, the C-C and C-C-O, are found at the same binding energy. In Schöll‘s model the C-C peak (peak 4) is shifted to 0.2 eV higher binding energies in comparison to the carbon atoms bound to hydrogen atoms (peak 3). The distance between these peaks is identical in our fit model. Furthermore the peak of the carbon atoms connected to oxygen atoms (peak 5) is shifted 2.5 eV upwards compared to the C-H peak in Schöll‘s model. In the C1s spectrum of the NTCDA-rich phase, the peak belonging to the C-O carbon is shifted upwards by 2.8 eV compared to the C-H peak. The larger deviation arises from the different chemical environment due to the adjacent CuPc molecules. Two further peaks appear in the spectrum which belong to the CuPc molecules (blue peaks). One of the peaks belongs to the C-C bound carbons of the benzene ring (peak 1) and the second one to the C-N bound carbons in the pyrrole ring (peak 2) [ECS+07]. In our model, the C-N peak is shifted upwards approximately 1.6 eV compared to the C-C peak. This value is larger than the 1.2 eV

C1s species	$E_b [eV]$	FWHM [eV]	Intensity [%]
CuPc C-C (1)	284.2	0.9	26
CuPc C-N (2)	284.2 + 1.6	0.9	10
NTCDA C-H (3)	284.8	1.1	9
NTCDA C-C (incl. C-C-O) (4)	284.8 + 0.2	1.1	14
NTCDA C-O (5)	284.8 + 2.8	1.3	9
Satellite 1 (A)	286.7	1.1	6
Satellite 2 (B)	289.1	0.9	2
Satellite 3	289.5	2.4	12
Satellite 4	292.1	3.9	10

Table 4.3.: List of binding energies E_b, FWHM, and relative areas of the peaks in our fitting model. The model was used for separating CuPc and NTCDA components from the C1s core level spectra of the NTCDA-rich phase at room temperature.

which was used for homomolecular structures of CuPc. The changed binding energies of the peaks of the NTCDA-rich phase compared to the homomolecular structures indicate that the charge is reorganized differently in the mixed structures.

In the C1s spectrum shown in Fig. 4.16, two further orange coloured peaks are shown (A and B). Both are satellites which belong to one of the molecules, but it can not be determined to which. A comparison with the satellites of the homomolecular structures does not help, as the satellites change their position in energy significantly depending on the molecular coverage [SKZ$^+$10]. Thus the area and binding energy of these peaks is constrained, but they were not considered for the area constraints done in the following section.

As for the O1s spectrum, the areas of the peaks have to be constrained. The C-C to C-N peak ratio stemming from CuPc is 3 : 1, for the C-C to C-H peaks of NTCDA it is 3 : 2 while the C-C to C-O peak ratio is 3 : 2. Further, the C-N peak position in energy of CuPc is connected to the C-C peak of CuPc and the C-O and C-H peaks position are connected to the C-C peak of NTCDA. Therefore, the peak positions and the areas of the peaks are fitted by only one parameter. Physically this means that only one height parameter is obtained for these species. This was necessary since otherwise no significant result could be obtained. In table 4.3 a summary of all peak positions, width and relative areas are shown. Two further satellites 3 and 4 are listed which arise from inelastically scattered electrons, but are not important for a proper separation of the molecular species. The parameter of the model were changed until the fraction of the species was maximized; this ensured a proper separation of all components.

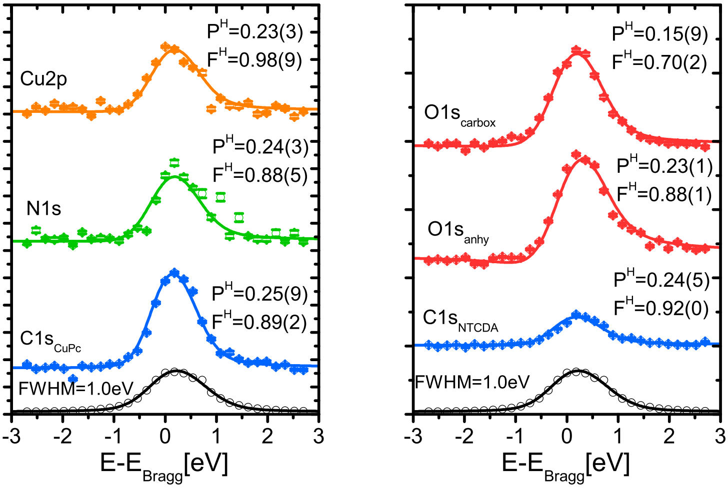

Figure 4.17.: Yield curves of all chemically different species of the NTCDA-rich phase at room temperature. The solid line shows the fit performed by Torricelli. Coherent positions and fractions corresponding to the averaged value of all XSW scans, are shown. The reflectivity curve is plotted as a black curve.

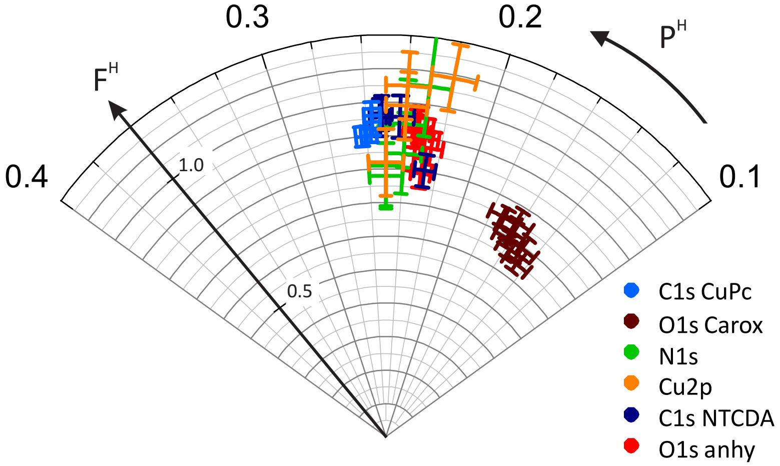

Figure 4.18.: Argand diagram representing the fitting results of all XSW scans obtained for the NTCDA-rich phase at room temperature.

B. Adsorption height at room temperature

All XPS spectra of an XSW scan were fitted with the fitting model described above and the peak area was used as yield curve versus the photon energy. The shape of the yield curves reflects the coherent position and fraction and can be determined by a least square fit with the program Torricelli [Mer12]. In Fig. 4.17 yield curves for all species of CuPc and NTCDA are plotted as an example for single XSW scans. Further, the reflectivity profile of the Ag(111) is shown. The error bars in the plot were determined in two steps. First the statistical errors, obtained by Monte Carlo error analysis, of the photoemission yield curves included in CasaXPS were calculated. In Torricelli these errors are propagated onto the uncertainties of the coherent position and fraction. The statistical error in the coherent fraction and position, obtained from represented XSW scans on different spots of the sample, is however more important as it reflects the accuracy of the determined coherent position and fraction of the individual scans.

The latter of the XSW scans, can be visualized by a so-called Argand diagram. In thus polar diagram the coherent position P^H is plotted as the polar angle and the fraction F^H in the radial direction. When many identical scans are performed, the distribution of their P^H and F^H can be displayed.

The Argand diagram of the NTCDA-rich phase, containing the results of all measured chemical species is displayed in Fig.4.18. It is clearly visible, that except from N1s (green) and Cu2p (yellow), all individual XSW scans of one species are located close to each other in the diagram which reflects the same fraction and position. This shows a very high reliability of our results. The scattering of the Cu2p and N1s scans is larger due to the low density of CuPc in the NTCDA-rich phase, which leads to a bad signal-to-noise ratio. The uncertainties of the resulting adsorption height of copper and nitrogen are nevertheless very small with a maximum of ±0.03 Å.

The coherent fraction of the carboxylic oxygen atoms (0.70) is lower than the fraction of the anhydride oxygen atoms (0.88). A reason for these low fractional values could be that the carboxylic oxygen is only bound to one carbon atom of the carbon backbone. Instead the anhydride oxygen is integrated in the carbon backbone and is thus bound to two carbon atoms. Therefore the adsorption height of the carboxylic oxygen atoms is less constrained.
The same effect has been observed for the homomolecular structures of PTCDA on Ag(100) and Ag(110) [BMW+12] and Ag(111) [HTS+10] and NTCDA [SHS+07] on Ag(111).

In the NTCDA-rich phase, the molecules align their adsorption heights to almost the same value, as already published for other heteromolecular structures [SSB+14]. Both molecules are however adsorbed at lower adsorption heights than in the homomolecular structures, whereas in all earlier measured heterostructures, both molecules adsorb between the respective adsorption heights of their homomolecular structures, except Goiri et al. [GMES+14]. A side view on the adsorption height model of the NTCDA-rich

chemical species	F^H	$d^H_{NTCDA,rich}$[Å]	$d^H_{HOMO,ML}$[Å]	$\Delta d^H_{Mixed-HOMO}$[Å]
$C1s_{total}$	0.87 ± 0.05	2.94 ± 0.02	3.00	- 0.06
$C1s_{NTCDA}$	0.92 ± 0.08	2.93 ± 0.03	3.00	- 0.07
$C1s_{CuPc}$	0.93 ±0.03	2.97 ± 0.01	3.08	- 0.11
$O1s_{total}$	0.72 ± 0.02	2.78 ± 0.01	2.87	- 0.03
$O1s_{carb}$	0.70 ± 0.03	2.73 ± 0.02	2.75	- 0.02
$O1s_{anhy}$	0.88 ± 0.05	2.90 ± 0.01	3.00	- 0.10
$N1s_{CuPc}$	0.9 ± 0.1	2.93 ± 0.02	3.04	- 0.11
$Cu2p_{CuPc}$	1.0 ± 0.1	2.91 ± 0.03	2.97	- 0.06

Table 4.4.: XSW results of coherent fraction and adsorption height of all chemical species the NTCDA-rich phase. For comparison the adsorption heights of the homomolecular structures of NTCDA [SHS+07] and CuPc [KSS+10] and the difference are shown.

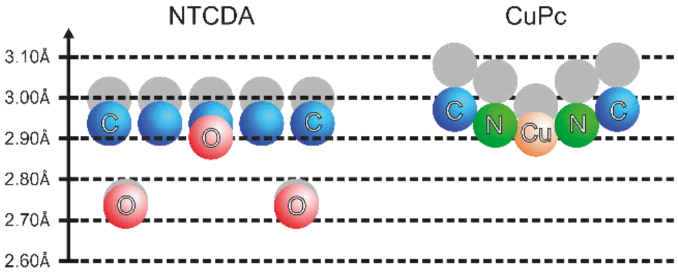

Figure 4.19.: Side view on the adsorption height model of the NTCDA-rich phase above the Ag(111) substrate at room temperature. The coloured circles show the adsorptions heights of the different species of the mixed phase. The grey one indicate the adsorption heights of NTCDA and CuPc in the pure homomolecular structures.

phase is plotted with all species coloured differently in Fig. 4.19. The grey circles indicate the adsorption heights of NTCDA and CuPc in their homomolecular structures [SHS+07],[KSS+10].

In addition the NTCDA molecule is less strongly distorted in the NTCDA-rich phase than in the homomolecular structure of NTCDA. The distance between the carbon backbone and the carboxylic oxygen is reduced to 0.20 Å compared to the homomolecular structure of NTCDA, namely 0.25 Å. This is based on the findings that the carbon backbone of NTCDA is situated at 2.93 Å, which is 0.07 Å lower than in the homomolecular RML structure of NTCDA. However, the carboxylic oxygen atoms are placed at 2.73 Å and the anhydride at 2.90 Å. Both oxygen types are at adsorption heights within the

C1s species	$E_b[eV]$	FWHM [eV]	Intensity [%]
CuPc C-C	283.9	1.0	30
CuPc C-N	283.9 + 1.6	1.0	12
NTCDA C-H	284.2	1.2	11
NTCDA C-C (incl. C-C-O)	284.2 + 0.2	1.2	17
NTCDA C-O	284.2 + 2.8	1.5	8
Satellite 1	286.5	1.1	7
Satellite 2	288.7	1.0	3
Satellite 3	289.4	2.9	10
Satellite 4	292.1	2.8	1

Table 4.5.: Binding energies E_b, FWHM, relative area of the peaks in our model, used for fitting of the C1s core level spectrum of the NTCDA-rich phase at 60 K.

O1s species	$E_b[eV]$	FWHM [eV]	Intensity [%]
Carboxylic Oxygen Main Line	530.7	1.3	30
Carboxylic Oxygen Satellite	530.7 + 1.6	1.4	20
Anhydride Oxygen Main Line	530.7 + 2.4	1.3	25
Anhydride Oxygen Satellite	530.7 + 3.3	1.9	6
Energy Loss Satellite	530.7 + 5.65	5.0	14

Table 4.6.: Binding energies E_b, FWHM, relative area of the peaks of the fitting model used for the O1s core level spectrumof the NTCDA-rich phase at low temperatures.

error bars of those in the homomolecular structures. An explanation for this unchanged adsorption height is probably the commensurate molecule-substrate relation which leads to the formation of well-defined Ag-O bonds.

The CuPc molecules change their adsorption height in the NTCDA-rich phase as well. The carbon atoms are located 0.11 Å closer to the silver substrate (at 2.97 Å). The nitrogen and coper atoms are shifted to smaller values by almost the same amount. The unusual lower adsorption height of both molecules in comparison to the homomolecular structures can not be explained without the investigation of the electronic properties of the mixed NTCDA- rich structure which will be done in the next subsection.

C. Core level spectrum at low temperature

The adsorption of water allowed us only to measure three O1s and C1s spectra for the NTCDA-rich phase at between 60 K and 80 K. In the XPS spectra of O1s a peak appeared between the peaks of the carboxylic and anhydride oxygen due to water adsorption. Therefore the sample was annealed to room temperature, as in UHV the water should desorb at this temperature. Unfortunately, the annealing temperature was higher, which led to a phase transition to the CuPc-rich phase. Thus the reliability of the O1s and C1s data is less than for the NTCDA-rich phase at room temperature. Further, XPS spectra at an energy off-Bragg were not recorded.

However a fitting model for the C1s and O1s spectra was established based on the XSW scans recorded before annealing. The core level spectra of C1s and O1s of the NTCDA-rich phase at low temperatures are very similar to the ones measured at room temperature. Therefore the fitting model is very similar to the room temperature model and is not additionally displayed. Several minor changes of the fitting model are described in the following.

The parameters of all peaks in the C1s model for low temperatures, are displayed in Tab. 4.5. The complete spectrum of C1s is shifted towards lower binding energies by 0.2 eV. All constraints, regarding the relative binding energy of the C-C peaks belonging to CuPc and NTCDA to all other peaks are identical to those in the fitting model of the NTCDA-rich phase at room temperature. The only difference is that the area ratio between the C-C peak and C-O peak of NTCDA changed from 3:2 to 2:1. The ratio had to be changed as the C-O peak was not correctly fitted. As it is not known from which molecule the peaks of the satellites 1 and 2 appear, the exact area ratio of the peaks can not be considered, since the satellites would have to be included in the calculation of the area ratios. Different area ratios were tested, but the resulting coherent position and fraction changed by less than the uncertainty of the method.

The fitting model of the O1s spectrum at low temperature is also based on the model at room temperature. The binding energy of the satellite belonging to the carboxylic oxygen is constrained at 1.6 eV compared to 1.4 eV at room temperature. This shift is probably necessary due to the adsorption of water. The "water"- peak appeared between the peaks of the carboxylic and anhydride oxygen atoms. Therefore the carboxylic satellite is shifted to higher binding energies, between the two main peaks for compensating the intensity arising due to water. A different fit model with an additional peak, situated between the oxygen peaks, was used. The resulting coherent fraction of the oxygen components was however worse. Therefore the fitting model without the additional peak was used in the end. All other parameters are almost the same as for the fitting model at room temperature and are summarized in Tab. 4.6.

D. Adsorption height at low temperature

The C1s and O1s yield curves are plotted in Fig. 4.20 (a). For each species one XSW scan is displayed as an example. The fitting results (coherent position and fraction) are also listed in the figure and represent the averaged value from all performed scans. In Fig. 4.20 (b) the Argand diagram is displayed, containing information about the coherent position and fraction of each single scan. It allows for an evaluation of the reliability of all included species. In the image it is clearly visible that the coherent position ob-

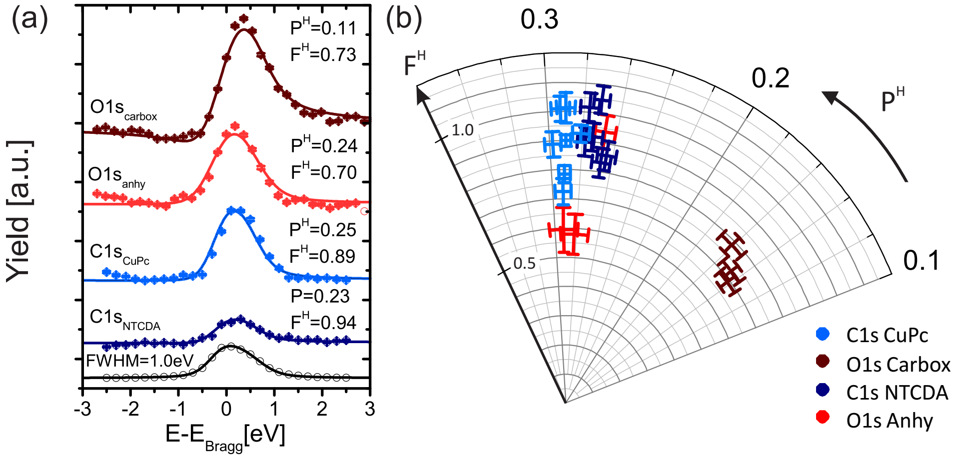

Figure 4.20.: (a) Yield curves of all chemically different species of the NTCDA-rich phase at 60 K. The solid lines show the fits done by Torricelli. The coherent positions and fractions belong to the averaged values from all XSW scan. The reflectivity curve is shown in black. (b) Argand diagram with the results of each individual XSW scan of the oxygen and carbon species.

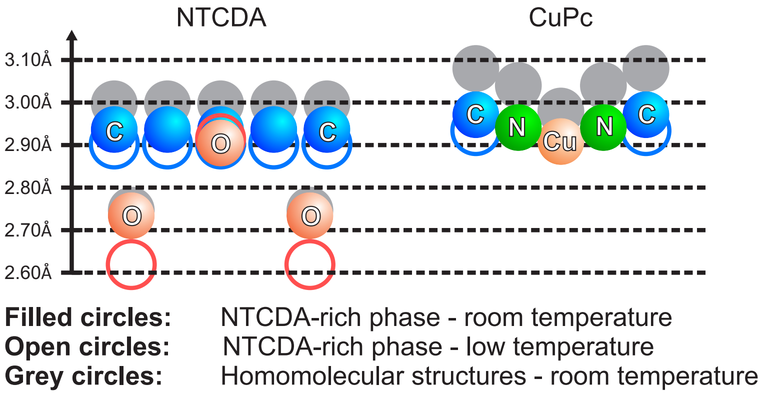

Figure 4.21.: Adsorption height model of the NTCDA-rich phase at room temperature and 60 K.

tained from six individual C1s scans deviate just slightly form the averaged value of P^H_{NTCDA}=0.23 and P^H_{CuPc}=0.25. These values, the coherent position and fraction are very similar to the values obtained for the total C1s signal (see Tab. 4.7). This indicates that the carbon atoms of NTCDA and CuPc are located at almost the same adsorption height. The coherent fraction of the carbon species of NTCDA and CuPc remained at

chemical species	$d^H_{NTCDA-rich}$[Å]		$F^H_{NTCDA-rich}$		
	RT	LT	RT	LT	Δd^H_{LT-RT}[Å]
C1s$_{total}$	2.94 ± 0.01	2.90 ± 0.01	0.87 ± 0.05	0.87 ± 0.05	- 0.04
C1s$_{NTCDA}$	2.93 ± 0.03	2.90 ± 0.03	0.92 ± 0.08	0.93 ± 0.08	- 0.03
C1s$_{CuPc}$	2.97 ± 0.01	2.94 ± 0.02	0.93 ± 0.03	0.9 ± 0.1	-0.03
O1s$_{total}$	2.78 ± 0.04	2.65 ± 0.03	0.72 ± 0.02	0.64 ± 0.08	- 0.13
O1s$_{carb}$	2.73 ± 0.02	2.61 ± 0.02	0.70 ± 0.03	0.73 ± 0.05	- 0.12
O1s$_{anhy}$	2.90 ± 0.01	2.91 ± 0.03	0.88 ± 0.05	0.7 ± 0.2	+ 0.01
N1s$_{CuPc}$	2.93 ± 0.02	-	0.9 ± 0.1	-	-
Cu2p$_{CuPc}$	2.91 ± 0.03	-	1.0 ± 0.1	-	-

Table 4.7.: Summary of the XSW results of the NTCDA-rich phase at LT in comparison to the corresponding RT results. The coherent fraction and adsorption height of all chemical species is given. The adsorption height change induced by cooling is shown in Å.

0.9 as it was observed for room temperature data.

The coherent fraction of the separated oxygen species ($F^H_{carb/anhy} = 0.7$) is higher than for the total O1s signal ($F^H_{tot} = 0.6$), but the fraction of the anhydride oxygen atoms seems to be stronger spread. Furthermore the statistical error bar, based on the standard deviation of the fractions of the single XSW scans, is ± 0.2 for the anhydride oxygen atoms, but only ± 0.05 for the carboxylic oxygen atoms. If the yield curves of the three measured scans is examined, it is visible that the coherent fraction of two of the scans is underestimated in the fit (Fig. 4.20). Thus the real fraction is probably higher.

For the transformation of the coherent position into the adsorption height, it has to be considered that the distance between the silver rows is smaller at 60 K in comparison to room temperature due to shrinking of the crystal. The distance is 2.3503 Å at 60 K [SW71]. As in the NTCDA-rich phase at room temperature, NTCDA and CuPc align their adsorption heights also at 60 K, but at a lower adsorption height. The values of all chemical species of the NTCDA-rich phase at RT and LT are displayed in Tab. 4.7. Furthermore, the adsorption height change of all species between room and low temperatures data is shown as well as the coherent fraction at room and low temperature. The resulting adsorption heights of all species of the NTCDA-rich phase at room and low temperatures are visualized in Fig. 4.21. The adsorption height difference between RT (filled circles) and LT (open circles) is shown. The carbon backbone of NTCDA is located at 2.90 Å and for CuPc at 2.94 Å. The carbon backbone of both molecules is therefore shifted by almost the same amount of 0.03 - 0.04 Å to lower adsorption heights in comparison to the room temperature data. This shift is only slightly larger than the error bar of the coherent position.

The adsorption height of both oxygen species changed very differently compared to the room temperature data. The carboxylic oxygen atoms are located at 2.61 Å, which is 0.12 Å lower than at room temperature. This corresponds to an adsorption height change four times as large due to cooling compared to that of the carbon backbone of the NTCDA molecule. The distance between the carbon backbone and the carboxylic oxygen is therefore increased to 0.29 Å (0.20 Å at RT). The NTCDA molecules are thus more strongly distorted at 60 K than at room temperature. The anhydride oxygen is located at 2.91 Å, which is almost the same value as at RT; they are therefore at the same adsorption height as the carbon backbone of NTCDA.

The shape of the CuPc molecules in the NTCDA-rich phase at 60 K could not be determined, as XSW scans of the Cu2p and N1s species were not measured.

4.4.2. The CuPc-rich phase

A. Core level model at room temperature

The XPS spectra are very similar to the one of the NTCDA-rich phase (see Fig. 4.22). In the N1s, Cu2p and O1s spectra all constraints are identical, only the peak width is slightly different. The values of the fitting model of the O1s spectrum are listed in Tab. 4.8.

The binding energies of the peaks in the fitting model of the C1s spectrum is also very similar to the spectrum of the NTCDA-rich phase (see Tab. 4.9). The C-O peak of NTCDA (peak 5) is however shifted upwards by 0.2 eV in comparison to the NTCDA-rich phase. Additionally, the binding energies of the satellites and the width of the peaks is slightly different.

O1s species	$E_b[eV]$	FWHM [eV]	Intensity [%]
Carboxylic Oxygen Main Line (1)	530.8	1.3	30
Carboxylic Oxygen Satellite (2)	530.8 + 1.65	2.9	25
Anhydride Oxygen Main Line (3)	530.8 + 2.4	1.2	7
Anhydride Oxygen Satellite (4)	530.8 + 3.3	1.5	24
Energy Loss Stellite	530.8 + 5.65	6.0	14

Table 4.8.: Binding energies E_b, FWHM and relative areas of the peaks in the O1s fitting model, used for the CuPc-rich phase at room temperature.

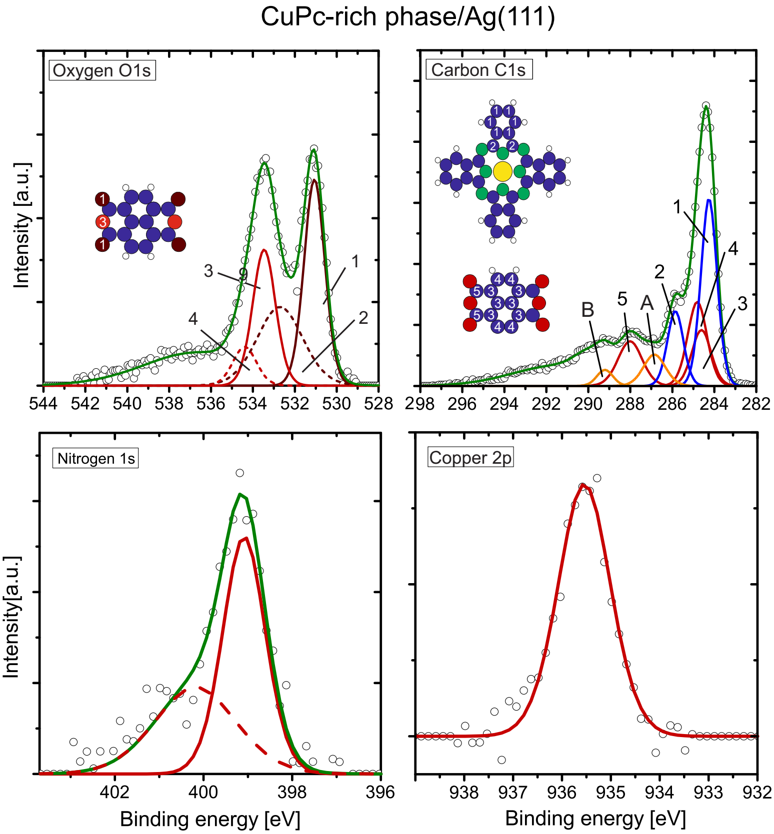

Figure 4.22.: High resolution XPS spectra of the oxygen O1s, carbon C1s, nitrogen N1s and copper Cu2p of the CuPc-rich phase. The peaks belonging either to NTCDA or CuPc are numbered. The corresponding values of these peaks are displayed in table 4.8 and 4.9

B. Adsorption height room temperature

As an example, one yield curve of each species is displayed in Fig. 4.23. The CuPc-rich phase at room temperature was measured at an earlier beam time (July 2013) compared the other data sets. At this time the intensity of the core level spectra was lower and therefore the signal-to-noise ratio was worse in comparison to the other beam time. Therefore the error bars of the yield curves of all species of the CuPc-rich phase are larger. This does not matter so much, as the more meaningfully determined error is in fact the deviation of the coherent position and fraction of the single scans from each other and will be discussed later in this chapter.

C1s species	$E_b[eV]$	FWHM [eV]	Intensity [%]
CuPc C-C (1)	284.2	0.9	26
CuPc C-N (2)	284.2 + 1.6	0.9	10
NTCDA C-H (3)	284.9	1.1	9
NTCDA C-C (incl. C-C-O) (4)	284.9 + 0.2	1.1	14
NTCDA C-O (5)	284.9 + 3.0	1.3	9
Satellite 1 (A)	286.8	1.2	6
Satellite 2 (B)	289.2	0.9	2
Satellite 3	289.9	1.7	5
Satellite 4	291.5	5.1	16

Table 4.9.: Binding energies E_b, FWHM and relative areas of the peaks in the C1s fitting model, used for the CuPc-rich phase at room temperature.

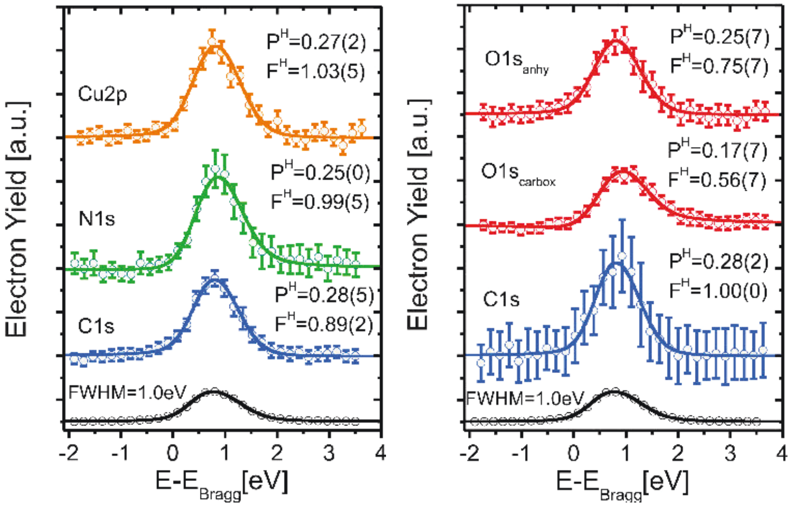

Figure 4.23.: Yield curves of all chemically different species of the CuPc-rich phase at room temperature. The solid lines show the fit results done by Torricelli. The coherent positions and fractions belong to one single XSW scan. The reflectivity curve is shown in black.

The coherent positions and fractions of all XSW scans are summarized in an Argand diagram in Fig. 4.24. The coherent position and fraction of all species, except that of the carboxylic oxygen atoms, are located around a coherent position of 0.28. The carboxylic oxygen species has a lower coherent position at 0.18. The coherent fraction is lower for both oxygen species than for the other species. The fraction of the carboxylic oxygen

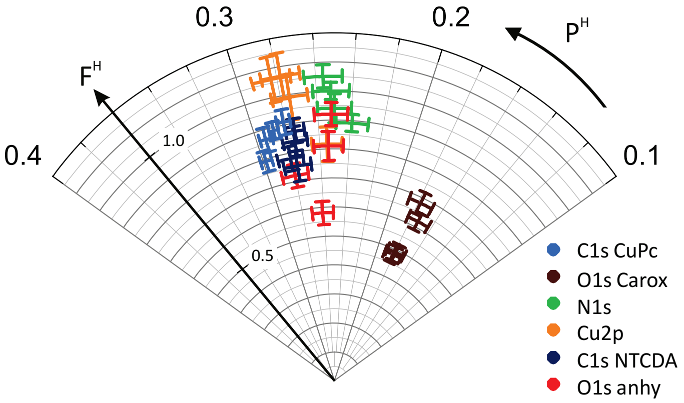

Figure 4.24.: Argand diagram of the reflecting the coherent position and fraction of all XSW scans for all species contained in the CuPc-rich phase.

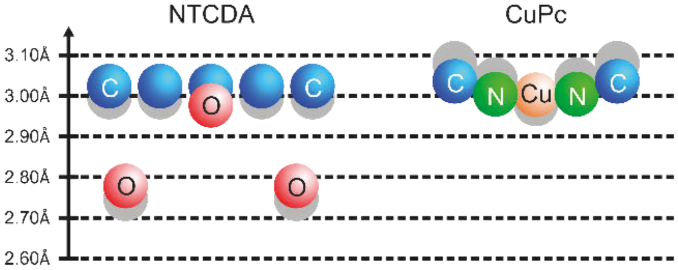

Figure 4.25.: Side view of the adsorption height model of the CuPc-rich phase above the silver substrate at room temperature. The coloured circles show the adsorptions heights of the different species of the mixed phase. The grey circles indicate the adsorption height of NTCDA and CuPc in the pure homomolecular structure.

atoms is averaged at around 0.57 and for the anhydride oxygen atoms at 0.76. One reason for the low values could be that at least two inequivalent NTCDA molecules are in the unit cell of the CuPc-rich phase present which are surrounded by two inequivalent CuPc molecules. This is a indication that the adsorption height of the oxygen atoms is possibly different for both NTCDA molecules.

The averaged adsorption height of all species of both molecules is plotted in a side view above the Ag(111) surface in Fig. 4.25.

Both molecules change their adsorption height in comparison to the homomolecular phases only slightly. The carbon backbone of the NTCDA molecule is 0.03 Å higher located (3.02 Å) and the CuPc carbon atoms are lowered by 0.05 Å (3.04 Å). The change

chemical species	$F^H_{CuPc-rich}$	$d^H_{CuPc-rich}$[Å]	$d^H_{HOMO,ML}$[Å]	$\Delta d^H_{Mixed-HOMO}$[Å]
$C1s_{Total}$	0.81 ± 0.04	3.01 ± 0.01	3.00	+ 0.01
$C1s_{NTCDA}$	0.82 ± 0.06	3.01 ± 0.01	3.00	+ 0.01
$C1s_{CuPc}$	0.8 ± 0.1	3.04 ± 0.01	3.08	- 0.04
$O1s_{Total}$	0.6 ± 0.1	2.83 ± 0.02	2.87	+ 0.03
$O1s_{carb}$	0.7 ± 0.1	2.78 ± 0.01	2.75	+ 0.03
$O1s_{anhy}$	0.8 ± 0.1	2.98 ± 0.03	3.00	- 0.02
$N1s_{CuPc}$	1.0 ± 0.1	3.00 ± 0.02	3.04	- 0.04
$Cu2p_{CuPc}$	1.0 ± 0.1	3.00 ± 0.02	2.97	+ 0.03

Table 4.10.: XSW results of the CuPc-rich phase. The coherent fractions and adsorption heights of all chemical species is given. The adsorption heights of the homomolecular structures of NTCDA [SHS+07] and CuPc [KSS+10] and the change in comparison to the CuPc-rich phase are shown.

of the carbon atoms belonging to the NTCDA molecules is therefore only in the range of the error bar, but significant for the carbon atoms of the CuPc molecule. The anhydride (2.98 Å) as well as the carboxylic (2.78 Å) oxygen atoms are present at a higher adsorption height in comparison to the homomolecular structures. The distance between the carbon backbone of NTCDA molecules and the carboxylic oxygen is 0.24 Å, which is almost identical with the homomolecular phase where the distance adds up to 0.25 Å. The distance between the anhydride oxygen and the carbon backbone is however slightly increased (0.04 Å). The NTCDA molecules are therefore similarly distorted in the CuPc-rich phase as in the homomolecular structure of NTCDA while the shape of the molecule is slightly changed due to the different anhydride position. These effects will be discussed in more detail in chapter 4.4.3.

The shape of the CuPc molecules is almost unvaried compared to the homomolecular structure of CuPc. The distance between the nitrogen atoms to the carbon backbone remains constant, but the copper atom is at a slightly higher position than the nitrogen.

C. Core level spectrum at low temperature

The CuPc-rich phase was cooled down to 60 K, but this temperature did not stay constant for the measurement of the complete data set. The effects on the measured data will be discussed later. Nevertheless, statistically acquired XPS spectra off Bragg of the carbon C1s and oxygen O1s were measured, but were not recorded for copper Cu2p and nitrogen N1s. XSW scans were however measured for all four species.

A fitting model for the C1s spectrum was established based on the off Bragg XPS measurement, see Fig. 4.26. The values of the fitting model are all displayed in Tab. 4.11. The fit parameters are almost identical to the model of the CuPc-rich phase at room

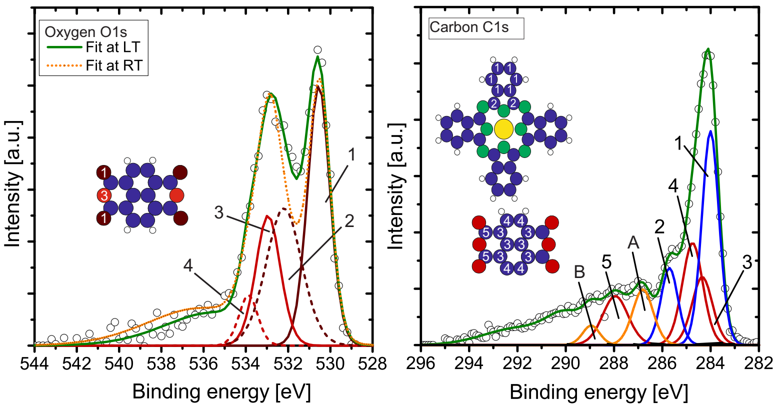

Figure 4.26.: High resolution XPS spectra of the oxygen O1s and carbon C1s of the CuPc-rich phase at LT. The orange line in the O1s spectrum indicates the corresponding spectrum at room temperature. The peaks belonging either to NTCDA or CuPc are numbered. The corresponding values of these peaks are displayed in Tab. 4.11 and Tab. 4.12.

temperature. The binding energies of the CuPc C-C and NTCDA C-C peak are equal. The constrained relation of the binding energies of the CuPc C-C and C-N peak changed slightly to a distance of 1.7 eV between the peaks, instead of 1.6 eV at room temperature.

The O1s spectrum is shown in Fig. 4.26 and the corresponding parameters of the fit model at 60 K are listed in Tab. 4.12. The whole spectrum is shifted downwards by 0.2 eV in comparison to the room temperature data. The relative peak positions to the carboxylic main line are identical; only the width of the peaks changed slightly. The O1s spectrum recorded at room temperature is indicated by an orange line. The intensity is clearly higher in the minimum between the peaks of the anhydride and carboxylic oxygen atoms at low temperatures. The reason is the adsorption of water molecules. The area of the carboxylic satellite (peak 2) is therefore increased as it includes the additional intensity in this region due to water. This effect does not influence the coherent position strongly as it is determined from the area change of the peaks, instead of the absolute area.

The Cu2p spectrum is almost identical to the one at room temperature. The peak has a binding energy of 935.1 eV (935.2 at room temperature). The N1s spectrum is also almost unchanged at 60 K. The main peak is situated at 398.7 eV and the silver plasmon stays constrained at a 1.1 eV higher binding energy than for core level spectra at room temperature.

C1s species	$E_b [eV]$	FWHM [eV]	Intensity [%]
CuPc C-C (1)	284.0	0.8	27
CuPc C-N (2)	284.0 + 1.7	0.8	10
NTCDA C-H (3)	284.5	1.0	10
NTCDA C-C (incl. C-C-O) (4)	284.5 + 0.4	1.0	15
NTCDA C-O (5)	284.5 + 2.8	1.2	9
Satellite 1 (A)	286.8	1.0	8
Satellite 2 (B)	288.9	0.8	2
Satellite 3	289.9	1.6	9
Satellite 4	292.1	3.2	8

Table 4.11.: Binding energies E_b, FWHM and relative area of the peaks of the C1s fitting model used for the CuPc-rich phase at 60 K.

O1s species	$E_b [eV]$	FWHM [eV]	Intensity [%]
Carboxylic Oxygen Main Line (1)	530.6	1.3	32
Carboxylic Oxygen Satellite (2)	530.6 + 1.65	2.0	27
Anhydride Oxygen Main Line (3)	530.6 + 2.4	1.4	19
Anhydride Oxygen Satellite (4)	530.6 + 3.3	1.1	5
Energy Loss Satellite	530.8 + 5.65	5.4	17

Table 4.12.: Binding energies E_b, FWHM and relative area of the peaks used for the O1s fitting model of the CuPc-rich phase at low temperatures.

D. Adsorption height at low temperature

Based on the fitting model, the yield curves of all species were determined and the coherent positions and fractions were subsequently identified by Torricelli. The electron yield curves of one XSW scan of all chemical species are displayed as an example in Fig. 4.27. The shown coherent positions and fractions in this image reflects the averaged value of all measured XSW scans. The chemical species are shown in two Argand diagrams as otherwise the position in the Argand diagram of almost all species would overlap (see Fig. 4.28). This indicates that the adsorption height of all these species is very similar and that both molecules are adsorbed at the same distance above the silver crystal. We measured various N1s and Cu2p scans due to a stronger scattering of the data, in particular the position of the N1s, as can be seen in Fig. 4.28 (a).

The resulting adsorption heights and coherent fractions of all chemical species in the CuPc-rich phase are summarized in Tab. 4.13 for the room temperature and the low temperature data. In the last column, the adsorption height change upon cooling is shown.

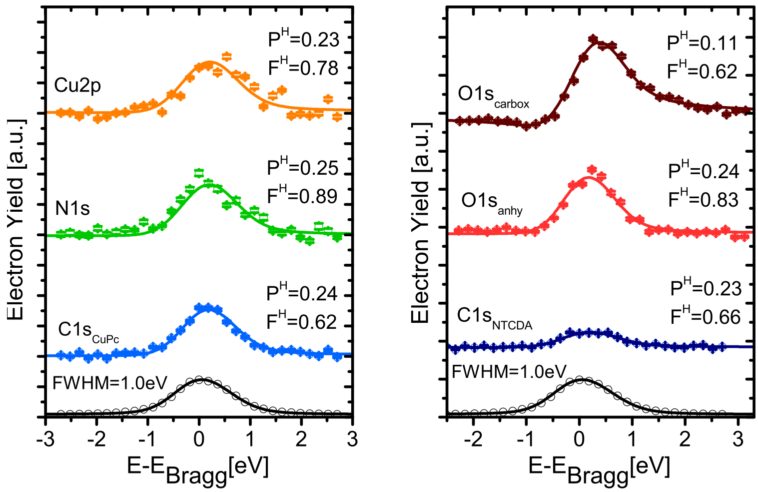

Figure 4.27.: Yield curves of all chemically different species of the CuPc-rich phase at room temperature. The solid line shows the fit done by Torricelli. The coherent positions and fractions belong to the averaged value of all XSW scans. In black is the reflectivity curve shown.

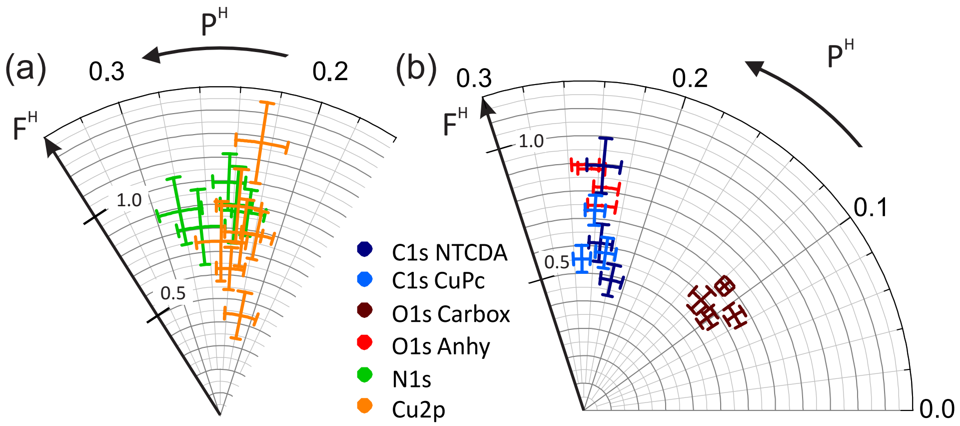

Figure 4.28.: (a) Argand diagram of the fitting results of all N1s and Cu2p XSW scans. (b) Argand diagram of the results of C1s of NTCDA and CuPc and of the carboxylic and anhydride oxygen atoms of the CuPc-rich phase at LT.

The result is also visualized in Fig. 4.29 in an adsorption height model of NTCDA and CuPc in the CuPc-rich phase. The room temperature data are indicated by filled

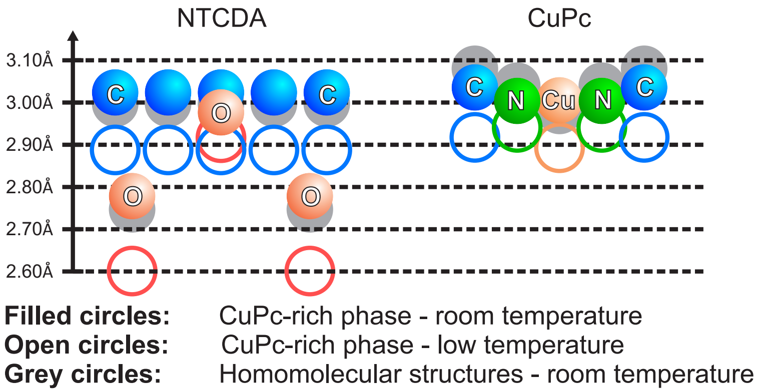

Figure 4.29.: Side view of the adsorption height model of the CuPc-rich phase above the Ag substrate at room temperature and 60 K. The coloured filled circles show the adsorption heights of the different species of the mixed phase at room temperature and the coloured open circles at 60 K. The grey one indicate the adsorption height of NTCDA and CuPc in the pure homomolecular structure at room temperature.

coloured circles and the data at 60 K with open coloured circles. The adsorption heights of the molecules in the homomolecular structures at room temperature are displayed by grey circles.

As can already be seen in the Argand diagram, the adsorption height of the carbon atoms of the NTCDA and CuPc molecules are aligned at 60 K as at room temperature, but at a lower height. The NTCDA molecules in the CuPc-rich phase at 60 K are more strongly distorted than at room temperature. The distance between the carbon backbone and the carboxylic oxygen at 60 K increased to 0.29 Å compared to the room temperature data (0.25 Å). The distortion is however identical to the NTCDA molecules in the NTCDA- rich phase at 60 K. This findings are based on the following results. The carbon backbone of NTCDA is situated at 2.89 Å and that of CuPc at 2.92 Å in the CuPc-rich phase at LT. The adsorption height of both carbon backbones is therefore lower by 0.13 Å (NTCDA) and 0.12 Å (CuPc), which is less than at room temperature. The adsorption height of the carboxylic oxygen atoms changed the most. They are located at 2.60 Å which is 0.18 Å lower than at room temperature.

The copper atoms are shifted identically as the carbon wings, but the nitrogen atoms of CuPc are adsorbed at 2.94 Å, which is only 0.06 Å lower than at room temperature. The error bar of the adsorption height of N1s is however with 0.05 Å the largest of all species (for an explanation see above). The others have only slightly larger error bars in comparison to the room temperature data. Therefore we can conclude that the CuPc molecules lowered their adsorption height, but the shape of the CuPc molecules is unchanged by cooling.

chemical species	$d^H_{CuPc-rich}$[Å]		$F^H_{CuPc-rich}$		
	RT	LT	RT	LT	Δd^H_{LT-RT}[Å]
C1s$_{Total}$	3.01 ± 0.01	2.88 ± 0.03	0.81 ± 0.04	0.6 ± 0.1	- 0.13
C1s$_{NTCDA}$	3.01 ± 0.01	2.89 ± 0.04	0.86 ± 0.06	0.6 ± 0.1	- 0.12
C1s$_{CuPc}$	3.04 ± 0.02	2.92 ± 0.03	0.8 ± 0.1	0.6 ± 0.1	- 0.12
O1s$_{Total}$	2.82 ± 0.02	2.65 ± 0.04	0.6 ± 0.1	0.63 ± 0.06	- 0.17
O1s$_{carb}$	2.78 ± 0.01	2.60 ± 0.03	0.7 ± 0.1	0.62 ± 0.06	- 0.18
O1s$_{anhy}$	2.98 ± 0.03	2.92 ± 0.03	0.8 ± 0.1	0.84 ± 0.07	- 0.06
N1s$_{CuPc}$	3.00 ± 0.02	2.94 ± 0.05	1.0 ± 0.1	0.89 ± 0.07	- 0.06
Cu2p$_{CuPc}$	3.00 ± 0.02	2.89 ± 0.03	1.0 ± 0.1	0.8 ± 0.2	- 0.11

Table 4.13.: Summary of the XSW results of the CuPc-rich phase at LT compared to its RT results. The coherent fraction and adsorption height of all chemical species is given. The adsorption height change induced by a crystal temperature of 60 K is shown.

As already shown by the Argand diagram, the coherent fractions of all species decreased by around 0.1 at 60 K in comparison to room temperature. The reason is probably a reduced order of the structure due to cooling, which seems to be caused by weak water adsorption.

4.4.3. Comparison of adsorption heights in different structures

The adsorption heights of the molecules in the NTCDA- and CuPc-rich phase were determined at room temperature and at 60 K. Fitting models for all XPS spectra were successfully established which allow for a separation of the all species in NTCDA and CuPc molecules. The most important findings are: (1) The (small) adsorption height differences the molecules exhibit in the homomolecular phases are levelled out upon the formation of the mixed structures at both temperatures. (2) The NTCDA molecules are less strongly distorted in the NTCDA-rich phase than in the homomolecular structure at room temperature. (3) Cooling led to a smaller molecule-substrate distance in all phases and to a stronger distortion of the NTCDA molecule in the NTCDA- rich and CuPc-ich phase compared to the homomolecular system at room temperature. The results are discussed in detail in the following.

In Fig. 4.30 the adsorption heights of all species of homo- and heteromolecular structures for RT and LT are compared with the corresponding values in their homomolecular structures. The figure shows that the molecules align their adsorption heights in both mixed phases at both temperatures most clearly to be seen for the CuPc-rich RT phase; where NTCDA moves up and CuPc downwards. This is effect has been observed for

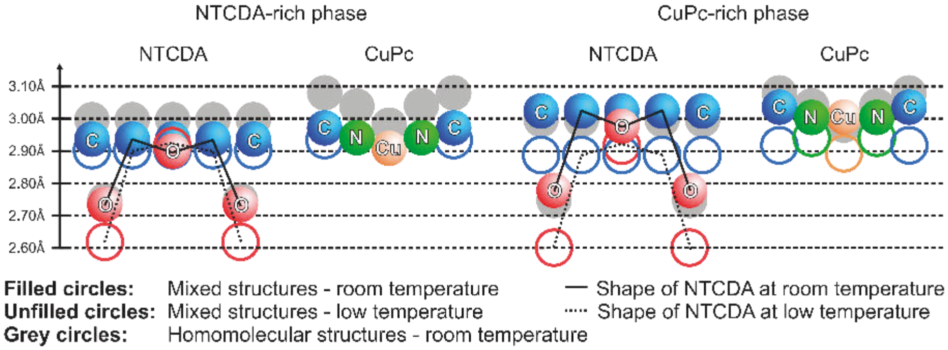

Figure 4.30.: Side view of the adsorption height model of both mixed phases at room temperature (coloured filled circles) and 60 K (coloured open circles). The NTCDA-rich phase is displayed left and the CuPc-rich phase on the right. The shape of the NTCDA molecule is highlighted by black lines for the room temperature data and by a dotted black line for the data at 60 K.

other heteromolecular structures [SSB+14]. In contrast the molecules in the NTCDA-rich phase both move downwards. Furthermore the molecules in the NTCDA-rich phase are adsorbed at lower heights than in the PTCDA-rich phase.

When cooling to 60 K both molecules lower their adsorption heights in both heterostructures, but conserve the alignment of their adsorption heights. Therefore the molecules are at almost the same adsorption height at 60 K in both NTCDA-CuPc heterstructures. A further interesting finding is that the carbon atoms of the NTCDA molecules in the NTCDA-CuPc systems at 60 K are adsorbed almost as low as PTCDA in its homomolecular structure at room temperature.

As Stadtmüller et al. have discussed, the adsorption height of molecules in heteromolecular structures appears to be decoupled from their electronic properties [SLW+14]. We have to compare our results, in order to receive a deeper understanding, with experiments earlier reported in literature involving CuPc, NTCDA and PTCDA on Ag(111) at different temperatures.

Comparison of CuPc molecules in hetero- and homomolecular structures at RT and LT

- Cooling influences the adsorption height of CuPc molecules in homo- and heteromolecular systems differently, as the molecules lower their adsorption height only in the heteromolecular system.

Kröger et al. [KSS+10] investigated the adsorption height of CuPc on Ag(111) for different coverages depending on the temperature. They showed that CuPc molecules are lifted upon increasing the CuPc coverage, but a change of temperature down to 140 K did not influence the adsorption height significantly. Only the nitrogen and copper

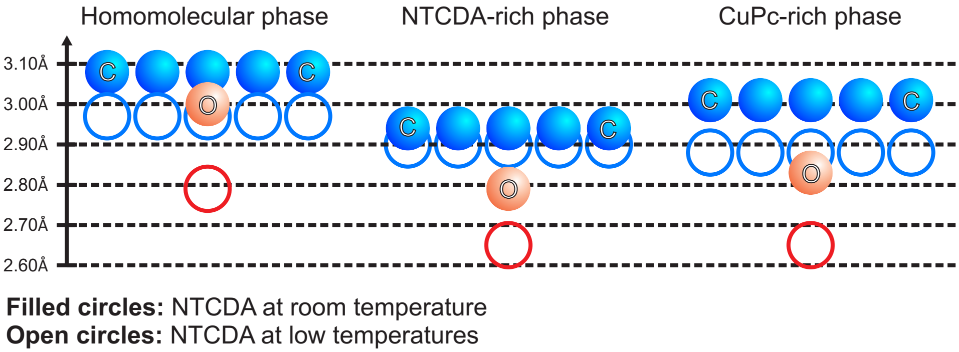

Figure 4.31.: Adsorption height model of the carbon and oxygen species of NTCDA in the homomolecular-, the NTCDA-rich- and the CuPc-rich phases at room temperature (filled circles) and 60 K (open circles).

atoms are at slightly lower adsorption heights, but the carbon backbone is unchanged. In addition, Kochler [Koc09] has proved that the electronic structure of CuPc films on Ag(111) is almost identical at room temperature and at 80 K. This indicates that the lower adsorption height for CuPc in the heteromolecular structures upon cooling might go along with a change in the electronic structure, as will be discussed in the next section.

Comparison of NTCDA molecules in hetero- and homomolecular structures at RT and LT

- The NTCDA molecules show the same trends in the homomolecular and heteromolecular structures: a decreased adsorption height at low temperatures.

- The adsorption height difference between the carbon and oxygen species of NTCDA at LT is smaller in the homomolecular structure (0.18 Å) than in the NTCDA-rich (0.25 Å) and the CuPc-rich phase (0.23 Å).

This finding are based on a comparison with data of the relaxed monolayer structure of NTCDA measured at 150 K by Stanzel et al. [Sta02]. The resolution of the analyser which was used at this time was worse than today, which made a separation of the differently bound carboxylic and anhydride oxygen atoms impossible. Therefore there are no data available for the bending of NTCDA at LT. We can thus compare only with data based on C1s spectra. The carbon backbone of NTCDA lowers its adsorption height due to cooling in the NTCDA-rich phase by less, in the CuPc-rich phase by more than in the homomolecular structure of NTCDA, as it is shown in Fig. 4.31. The carbon atoms are lowered in the homomolecular structure of NTCDA due to cooling by $\Delta = 0.11$ Å, in the NTCDA-rich phase by 0.04 Å and for the CuPc-rich phase by 0.13 Å.

For the oxygen atoms, the adsorption height and coherent fraction, based on the integrated oxygen spectrum, was determined. This led to the finding that the change of average adsorption height of the oxygen atoms due to cooling is stronger in the homomolecular phase than in the mixed structures, although the homomolecular structure was only cooled down to 150 K in contrast to the heteromolecular structures, which were cooled to 60 K (see Fig. 4.31). While in the homomolecular structure the average height of the oxygen atoms was 2.79 Å at 150 K and 3.01 Å at RT, i.e. the difference is 0.22 Å, in the mixed phases this differences are smaller by 0.13 Å and by 0.18 Å for the NTCDA- and CuPc-rich phases, respectively.

Comparison with the behaviour of PTCDA in homomolecular systems

An adsorption height decrease due to cooling was also observed for PTCDA on Ag(111) by Hauschild et al. [HTS+10]. The molecules in a disordered LT phase exhibit a lower adsorption height than in the ordered herringbone structure at room temperature. The authors interpret these effects by a stronger molecule-substrate interaction at low temperature. The intermolecular interaction between the molecules is explained to be reduced by the lateral disorder at low temperature. In contrast, the PTCDA molecules can only form weaker Ag-O bonds at room temperature due to competitive intermolecular interactions and a back action of these to the bond between the carbon backbone and the silver substrate. The structure of the NTCDA- and CuPc-rich phase was unchanged during cooling, as LEED confirmed.

- Since changes of the lateral structure due to cooling can be excluded for the mixed systems of NTCDA and CuPc, the lower adsorption heights must be caused by intramolecular interactions, which are induced by changed molecules-substrate interactions.

Comparison of the molecular shapes in heterostructures to their homomolecular structures at RT and LT

The shapes of the NTCDA and PTCDA molecules are of special interest, as the adsorption height of the oxygen atoms in relation to the carbon backbone and the silver substrate describes the interaction between the reactive molecular groups and the substrate. This helps to explain the bonding strength between the molecules and the substrate [HKC+05], [HBL+07].

Two different principal shapes of NTCDA and PTCDA on various substrates were observed earlier; on the one hand a saddle-like geometry, where the anhydride oxygen atoms are located above the carbon backbone and the carboxylic oxygen underneath. This was observed for PTCDA molecules in the monolayer structure of PTCDA on Ag(111) and in the MBW-phase at 50 K. On the other hand the so-called "M"-like shape exists, where both anhydride and carboxylic oxygen atoms are located underneath the carbon atoms. This shape was observed for the MZZ-phase [Sta13], and for homomolecular phases of PTCDA on the more reactive Ag(100) and Ag(110) substrate [BMW+12] at

	d^H[Å]		Δd^H[Å]		Shape of
Phase	O_{anhy}	O_{carb}	$O_{anhy} - C$	$O_{carb} - C$	(N)/(P)TCDA
RML NTCDA RT	3.00	2.75	0.00	- 0.25	S
NTCDA-rich RT	2.90	2.73	- 0.03	- 0.20	M
NTCDA-rich 60 K	2.91	2.61	+ 0.01	- 0.29	S
CuPc-rich RT	2.98	2.78	- 0.04	- 0.23	M
CuPc-rich 60 K	2.92	2.60	+ 0.03	- 0.29	S
MZZ-phase RT	2.92	2.79	- 0.09	- 0.22	M
MBW-phase LT	3.10	2.63	+ 0.10	- 0.37	S
ML PTCDA RT	2.98	2.66	+ 0.12	- 0.20	S
ML PTCDA 150 K	2.83	2.50	+ 0.02	- 0.36	S

Table 4.14.: Adsorption heights of the anhydride and carboxylic oxygen atoms of NTCDA and PTCDA and their distance to the carbon backbone for the homomolecular structure of NTCDA, the NTCDA- and CuPc-rich phases at room temperature and 60 K. This is also shown for the MZZ- phase, the Mixed Brickwall structure at 50 K and the homomolecular structure of PTCDA at RT and 150 K. The shape of the molecules is called M for a "*M*"- like shape and S for a saddle like shape.

room temperature. Bauer et al. assumed that the "M"-like shape occurs due to an enhanced interaction between the anhydride oxygen atoms and the silver surface, which is the case for commensurate structures. This can explain the adsorption geometry in both homomolecular phases, but not in the MZZ-structure since this only has a point registry.

The adsorption height of the anhydride and carboxylic oxygen atoms and their distances to the carbon backbone are summarized for all measured phases: heterostructures of NTCDA-CuPc and PTCDA-CuPc, and homomolecular structures of NTCDA and PTCDA at room temperature and 60 K or 150 K (see Tab. 4.14).

The table clearly demonstrates that PTCDA and NTCDA have in all homomolecular structures at RT and LT, and in all heteromolecular structures at LT a saddle like shape. The "*M*"-like shape occurs in all heteromolecular phases at RT. Although the C-O$anhy$ distance is often within the experimental uncertainness, it reflects a clear trend for all structures. In addition the molecules are in all phases more strongly distorted at LT compared to the their homomolecular structure at room temperature.

The distance between the carboxylic oxygen and the carbon atoms of the NTCDA molecule increases to 0.29 Å in the CuPc- and NTCDA-rich phases due to cooling compared to the 0.25 Å of NTCDA in the relaxed monolayer at room temperature. This is the opposite effect compared to the mixed NTCDA-CuPc structures at room temperature, where the distortion of the NTCDA is reduced (Tab. 4.13). These results can unfortunately only be compared with data based on the integrated spectra of carbon and oxygen of the homomolecular structure of NTCDA cooled to 150 K, which does not allows for a determination of the molecular shape and its distortion. In contrast, PTCDA has the same distortion of 0.20 Å in the homo- and heteromolecular structures at room temperature, which increases at lower temperatures to 0.37 Å. However, since the lateral order in the homolecular structure of PTCDA due to cooling a proper comparison of the molecular shape is not possible.

Nevertheless, the reduction of the adsorption height upon cooling combined with the change from a "M"-like shape to a saddle-like shape at first sight contradicts the assumption of Bauer et al. that the "M"-like shape occurs due to a stronger molecule-substrate interaction. However, the reduced adsorption height of the molecules in the mixed NTCDA-CuPc structures due to cooling is approximately connected with a stronger binding of the molecules to the substrate, as no additional channel for charge transfer is induced just by cooling. The shift towards higher binding energies of the LUMO of PTCDA on Ag(111) at LT [KHT+08] strengthen our findings.

Summary

To conclude this section, we obtained some interesting new findings about the vertical structure of molecules in heteromolecular structures on Ag(111):

At room temperature:

- The adsorption height alignment was found for all systems under study and hence appears to be a general trend[1].
- The NTCDA molecules are less strongly distorted in the NTCDA-CuPc heterostructures than in their homomolecular structure and have an "M"-like shape.
- The distortion of PTCDA molecules in the MZZ heterostructure and the homomolecular structure is similar. But the shape of the PTCDA is "M"-like in the MZZ- phase, in contrast to the homomolecular structure.
- The shape of the CuPc molecules does not change significantly in the NTCDA-CuPc heteromolecular structures in comparison to the homomolecular phase.

At low temperature:

- The adsorption height alignment in heteromolecular structures is also valid at low temperatures.
- The NTCDA molecules are more strongly distorted in the NTCDA-CuPc heterostructures than in their homomolecular and heteromolecular structures at room temperature.

---

[1] execpt [GMES+14]

- The NTCDA molecules change their shape during cooling from an "M-like" to a saddle-like shape. This is mainly due to a stronger down-shift of the C-core and the carboxylic oxygen compared to the anhydride oxygen atoms.

- In the mixed structures the PTCDA molecule is more strongly distorted at LT than at room temperature. In the MBW phase at LT its distortion is very similar to that as in the homomolecular structure at LT.

- The CuPc molecules do not change their shape significantly in the NTCDA-CuPc heterostructures at 60 K.

The XSW data alone cannot reveal the origin of the change in the molecular shapes and the different adsorption heights of the molecules at room and low temperatures, but allow some speculations which are addressed in the following section. The different distortions of NTCDA and PTCDA molecules in the heteromolecular structures might be related with a different charge transfer to the molecules in comparison to their homomolecular structures. Also the stronger distortion and lower adsorption height of the NTCDA molecules, which was observed for the homomolecular and heteromolecular structures at LT, is probably caused by a larger charge transfer to the LUMO of NTCDA. The LUMO of CuPc may also become partially filled. This would explain that they both approach the surface since they can accept charge from the surface spill out into their LUMOs.

The effect of an adsorption height decrease in PTCDA-CuPc heterostructures due to cooling seems to be weaker than for NTCDA-CuPc structures. The LUMO of CuPc remains empty in this system, only the LUMO of PTCDA is shifted towards higher binding energies [SLW$^+$14]. Thus the additional filling of the LUMO of CuPc could explain the stronger adsorption height change in the NTCDA-CuPc heterostructures.

Therefore the electronic structure of these structures has to be investigated in detail to determine the binding strength of the molecules to the substrate and influence of temperature on the binding energy of the molecular orbitals. The results of this study are presented in the next chapter.

4.5. Electronic properties of NTCDA-CuPc heterostructures on Ag(111)

In this section the influence of the lateral and vertical geometry on the electronic properties of the mixed NTCDA - CuPc systems on Ag(111) is discussed. As already shown in chapter 4.4 Stadtmüller et al. revealed that the distance of the molecules above the substrate is not "coupled" to the binding strength in PTCDA-CuPc heteromolecular systems [SLW$^+$14]. It is thus essential to determine the electronic properties of the different NTCDA-CuPc heterostructures as they reveal the bonding strength of the molecules to the substrate and are likely to explain the vertical geometry of the system.

The electronic properties were determined by photoemission spectroscopy (PES) and angle resolved PES (ARPES). The ultraviolet photoelectron spectroscopy was performed at room and low temperatures, as we wanted to investigate how the temperature influences the binding strength of the molecules in the mixed NTCDA - CuPc systems. Additionally, STS measurements were done to confirm the occupation of the F-LUMO of NTCDA determined by orbital tomography.

4.5.1. The NTCDA-rich phase

A. Ultraviolet photoelectron spectroscopy at room and low temperatures

The photoelectron spectrum of the NTCDA-rich phase at RT was measured at the BESSY II storage ring in Berlin and is shown in the lower part of Fig. 4.32. The spectrum of the same phase at 60 K was recorded with a UV light source at Diamond

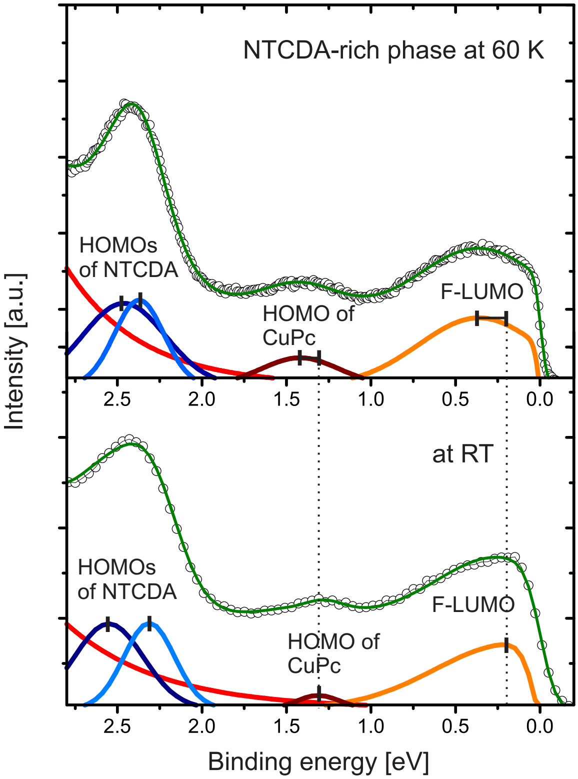

Figure 4.32.: UPS spectra of the NTCDA-rich phase at 60 K (upper part) and at room temperature (lower part). The peaks used for fitting are plotted in different colours and the shifts due to temperature decrease are indicated by dashed black lines.

and is displayed in the upper part of Fig. 4.32. A peak is visible in the spectra at a binding energy of 1.34 eV at RT and at 1.39 eV at LT. It can be assigned to the HOMO of CuPc from comparison with spectra of the homomolecular monolayer structure of CuPc [KSS^{+}10], where the HOMO peak is located at 1.25 eV at RT and LT. The HOMO peak is thus shifted to higher binding energies in the NTCDA-rich phase, in particular at LT.

Two overlapping peaks are visible at the binding energies of 2.31 eV and 2.58 eV at RT and 2.31 eV and 2.50 eV at 60 K. Either they stem from the two inequivalent NTCDA molecules or one peak arises from the HOMO-1 of CuPc ($E_B = 2.2$ eV [KSS^{+}10]). Therefore ARPES data were recorded in this binding energy region, which in the following will be deconvoluted by orbital tomography to assign the peaks correctly.

Most importantly both spectra clearly show a resonance near the Fermi level, corresponding to the former LUMO, which due to molecule adsorption is partially filled. At RT the LUMO peak is located at a binding energy of 0.25 eV and is shifted to 0.35 eV at 60 K. By UPS it can not be determined which molecule this peak stems from, but from earlier measurements with PTCDA and CuPc heterostructures it is known that only the LUMO of PTCDA is populated and the LUMO of CuPc is depleted [SLW^{+}14]. As NTCDA is a weaker charge acceptor, it is very interesting to investigate whether the whole charge is still transferred to the NTCDA molecules or the CuPcs have to act as a electron acceptor as well for compensation the weaker filling of the NTCDA LUMO.

B. ARPES and orbital tomography

For the determination which orbital of which molecule contributes to the peaks observed by UPS, ARPES measurements and consequently orbital tomography was performed. Therefore the theoretical angular momentum maps for the different in-plane orientations of NTCDA and CuPc, the orientations are known from the STM data shown earlier in this chapter, were calculated as described in chapter 2.3 and are shown in Fig. 4.33 (a-d). Due to the six-fold symmetry of the substrate, the momentum maps of molecules whose in-plane molecular orientations are multiples of 60° relative to the [-110] direction of the substrate are identical. For simplicity they are therefore labelled by the in-plane orientations used in the former chapters, although in reality they are rotated by a multiple of this number. In the following the orbitals are thus always labelled by the type of molecule and the corresponding rotation angle of the molecules to the [-110] direction of the silver substrate.

The ARPES data cube recorded in the energy regime of the LUMO was deconvoluted by the maps shown in Fig. 4.33: (a) the NTCDA LUMO 0°, (b) the CuPc LUMO 65°, (c) the CuPc LUMO 20° and (d) the NTCDA LUMO 45°. The map of the NTCDA LUMO 0° has exactly the same intensity distribution as that of the homomolecular RML of NTCDA with six sharp intensity maxima. In contrast the momentum map of the NTCDA 45° has a ring-like intensity distribution with twelve smaller maxima. The momentum map of the CuPc LUMO 65° has broadened intensity maxima at the same location in k-space as the NTCDA LUMO 0°. In addition, intensity lobes besides these maxima are present at higher k values. The momentum map of the LUMO CuPc 20° has a similar intensity distribution as the 65° rotated momentum map of CuPc, but is

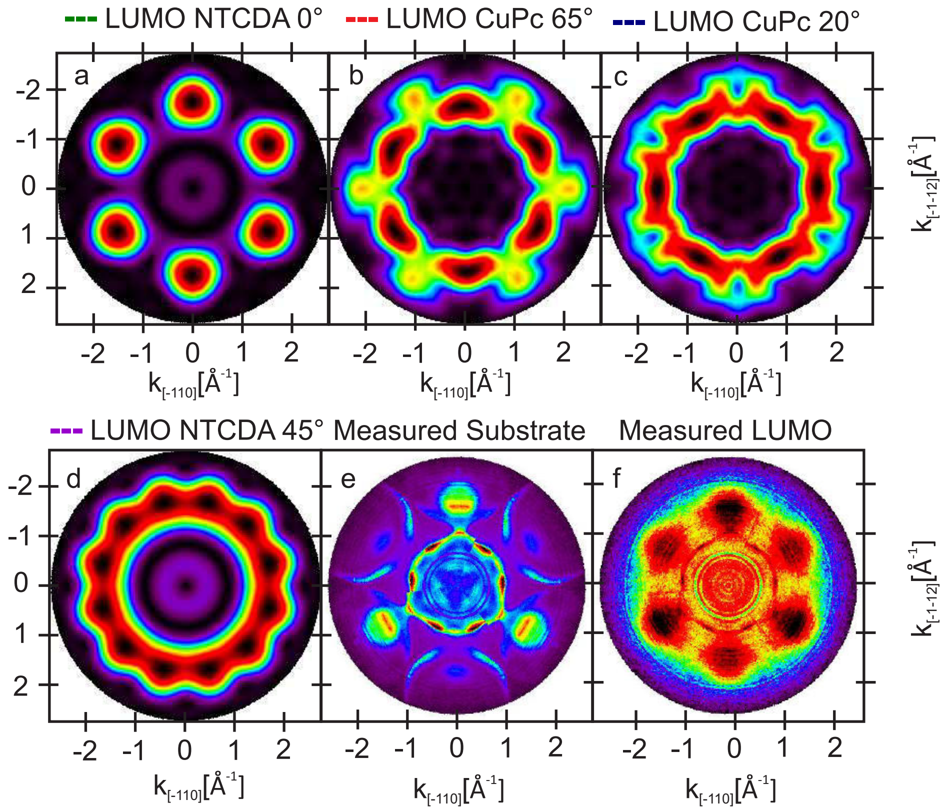

Figure 4.33.: Theoretical angular momentum maps of the NTCDA LUMO aligned parallel to the [-110] substrate direction (a), the CuPc LUMO rotated 65° (b), 20° (c), the NTCDA LUMO rotated 45° (d) to the [-110] direction are shown. These maps were used for the deconvolution. (e) Measured map of the plain substrate in the energy regime of the Fermi level. (f) Measured CBE map at $E_B = 0.25$ eV of the NTCDA-rich phase.

rotated by 22.5°. The intensity maxima are therefore located at the k-space where the CuPc 65° map has its lower intensity lobes. Both momentum maps of CuPc reveal a sixfold symmetry.

The different positions of the intensity maxima in the k - region of the four theoretical maps allow for a successful deconvolution of the ARPES data cube recorded in the LUMO energy regime by orbital tomography. The measured constant binding energy (CBE) map at a binding energy of 0.25 eV is plotted in Fig. 4.33 (f). This map has six intensity maxima at the same k - values as the theoretical map of the NTCDA LUMO 0°. Additional intensity is visible between the maxima. The symmetry of the experimental

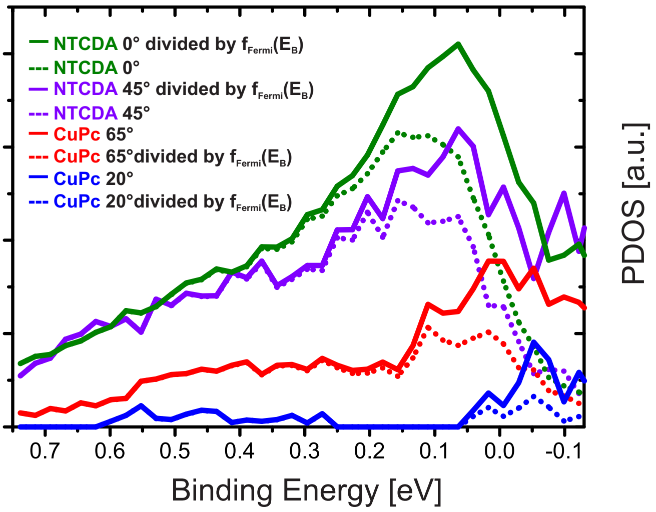

Figure 4.34.: The result, the PDOS versus the binding energy, of the orbital tomography fitting routine. The green line corresponds to the NTCDA 0° contribution, the purple line to NTCDA 45°, the red one to the CuPc 65° and the blue one to the CuPc 20°.

momentum map is reduced to three-fold due to the contribution of the sp-band of the silver substrate in this binding energy regime. Three of the maxima have therefore clearly a higher intensity. Around smaller maxima a parabolic intensity distribution is visible instead. Therefore the data cube of the plain silver substrate was included in the orbital tomography fitting which is displayed in panel (e).

For a qualitative analysis, the ARPES data cube was fitted with the theoretical and substrate maps. The result, the PDOS, are plotted versus binding energy in Fig. 4.34. The fitting coefficient $a_i(E_B)$ can be understood as the density of occupied states, which differs from the PDOS since the peak is located close to the Fermi level. The PDOS is obtained by dividing $a_i(E_B)$ through the Fermi function. In this case, the Fermi function for $T_{eff} = 930$ K was used for a broaden Fermi distribution function and instrumental resolution of 150 meV. The DOS is plotted for all contributing molecules by solid lines and the occupied density of states by dashed lines as shown in Fig. 4.34. The PDOS of NTCDA 0° (solid green line) and NTCDA 45° (solid purple line) reveal sharp peaks close to the Fermi level, both at a binding energy of $E_B = 0.08$ eV. The comparison of the DOS and the PDOS shows clearly that the orbitals are not completely filled.

The PDOS of CuPc 65° and 20° show both a broad peak close above the Fermi level. Therefore it is not ambitiously determinable whether the LUMO of CuPc, in particular for the CuPc 65° (red solid line) is due to the broad Fermi function slightly filled or this peak is only an artefact of the fitting routine.

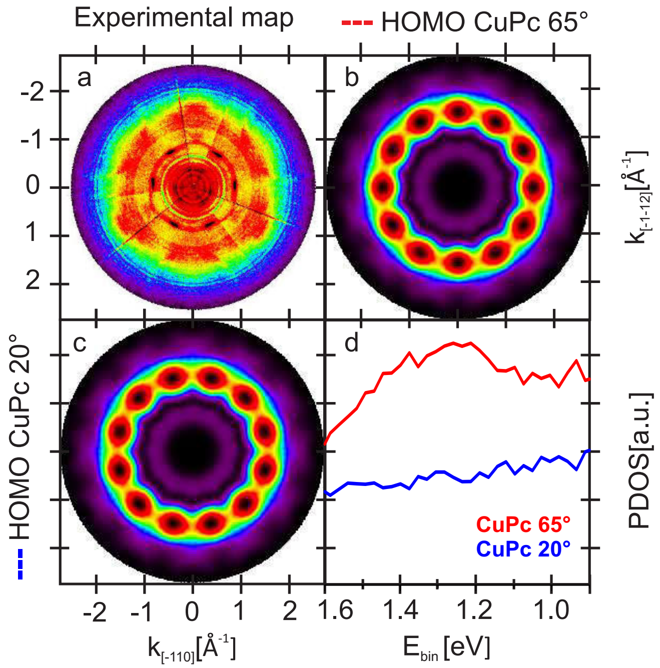

Figure 4.35.: The experimental momentum map of the CuPc HOMO of the NTCDA-rich phase at $E_B = 1.25$ eV is plotted in (a). The theoretical momentum map of the CuPc HOMO with a molecule rotation of 65° (b) and with 20° (c) to the [-110] direction is shown. (d) The PDOS of both CuPcs versus binding energy is displayed.

Furthermore the photoelectron intensity was recorded in the energy range of the HOMO of CuPc, but the intensity was very weak according to the NTCDA : CuPc ratio of 4:1. In addition it was difficult to find a proper 120° broad part of the momentum map (which is necessary for a symmetrization to a full map), without any intensity stemming from imperfectly aligned beam entrance slits on the channel plates. Nevertheless orbital tomography was performed with the theoretical momentum maps of two differently rotated CuPcs. In 4.35 (b) the theoretical momentum map with molecules rotated 65° and in (c) rotated 20° to the [-110] direction of the silver substrate are shown. In Fig. 4.35 (a) the experimental CBE map at a binding energy of $E_B = 2.4$ eV is displayed. In this map three radial stripes are visible, which were caused by an error of the channel plate during the measurement. The result of the fit is shown in Fig. 4.35 (d). The PDOS of the CuPc 65° reveals a peak at a binding energy of $E_B = 1.25$ eV, but the PDOS of the CuPc 20° has a linear shape. Based on the stoichiometry found in STM images, both molecules should contribute equally to the density of states. The reason for this discrepancy is probably the already mentioned bad quality of the measured ARPES

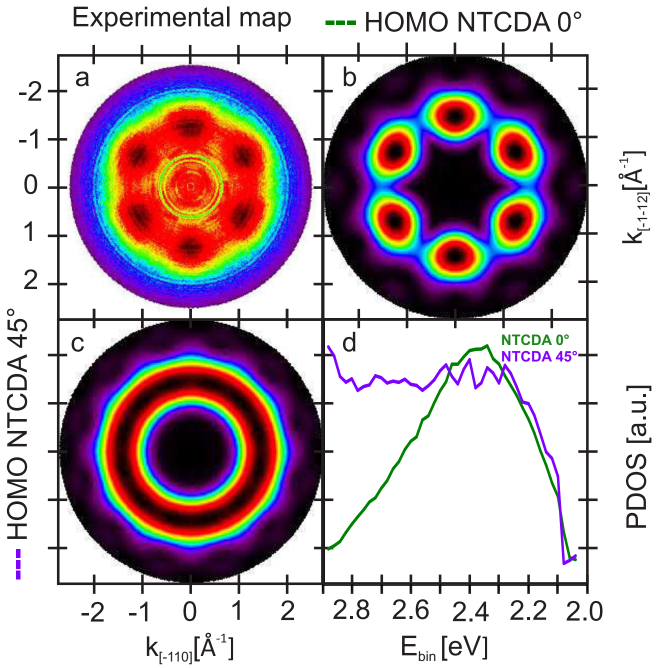

Figure 4.36.: The experimental NTCDA HOMO of the NTCDA-rich phase is plotted in (a). The theoretical map of the NTCDA HOMO parallel to the [-110] direction is shown (b) and in (c) the resulting PDOS is displayed

data cube. The experiment has to be repeated with better adjusted entrance lenses.

The resonance stemming from the NTCDA HOMO was also investigated by ARPES. In Fig. 4.36 (a) the experimental momentum map of the NTCDA HOMO with six characteristic features is displayed at a binding energy of 2.35 eV. Between the maxima diffuse intensity is visible. The theoretical momentum maps for both inequivalent NTCDAs, 0° Fig. 4.36 (b) and 45° Fig. 4.36 (c) rotated to the [-110] direction were used for the deconvolution of the data cube. The result of the fit, the PDOS, is displayed in Fig. 4.36 (d). The maximum of the NTCDA HOMO 0° is located at E_B = 2.35 eV. The PDOS of the NTCDA HOMO 45° has on the right side of the curve (lower binding energies) the expected shape, but a plateau at higher binding energies. Therefore it seems that the fit worked properly at low binding energies, but a ring-like background appeared in the ARPES data cube at higher binding energies, which leads to a plateau in the PDOS. This background probably stems from the HOMO-1 of CuPc which is located in this binding energy regime [KSS^{+}10] and therefore overlaps with the HOMOs of NTCDA.

Nevertheless, the peak of the HOMO NTCDA 0° is shifted to 130 mV lower binding energies in comparison to the homomolecular RML of NTCDA. The fit of the UPS spectrum revealed that the HOMO is located for the NTCDA-rich phase at 2.42 eV (a difference of 70 meV). A more exact determination of the binding energy by orbital tomography in comparison to UPS is possible due to the fact that the momentum maps are a unique fingerprint of the corresponding orbitals and therefore enable a more precise assignment of the binding energy of the orbital.

C. Scanning tunnelling spectroscopy

We could not determine unambiguous by ARPES and orbital tomography whether the LUMO of CuPc is partially filled or not. Therefore scanning tunnelling spectroscopy (STS) measurements of the NTCDA-rich phase were performed at 5 K. In Fig. 4.37 (a) an LT-STM image is displayed where the unit cell of the NTCDA-rich phase is indicated by white arrows. For each NTCDA and CuPc molecule, marked by different coloured

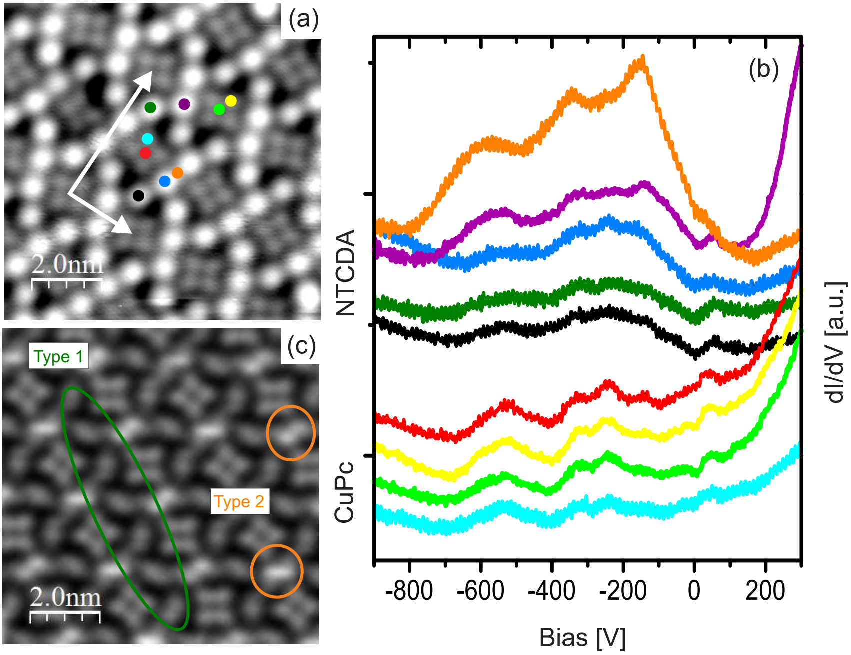

Figure 4.37.: (a) STM image of the NTCDA-rich phase (I=0.05 nA, V=1.5 V). The coloured dots mark the different molecular positions where dI/dV spectra were recorded (T=5 K, modulation: ν=912 Hz, amplitude: 10 mV, T_c=50 ms). (b) The corresponding spectra of all NTCDAs and CuPcs. (c) Constant height STM image of the NTCDA-rich phase (I=0.05 nA, V=50 mV)

dots, dI/dV was recorded and is shown in Fig. 4.37 (b). These spectra represent the local density of states at the respective positions on the surface.

The spectra recorded above the lobes and the centres of the two inequivalent CuPc molecules (in red, yellow, light green and turquoise) show an almost flat line with some small peaks, which probably stem from tip states. Since a broader peak is not visible, it is likely that the small peaks present in the PDOS, which was obtained from orbital tomography, are only fitting artefacts. Therefore it can be concluded that the LUMO of CuPc is depleted.

In Fig. 4.37 (c), a constant height LT-STM image recorded at a bias of 50 mV, it is clearly visible that the electronic contrast of the NTCDA molecules is different. The darker NTCDAs are called type 1 and the brighter type 2. Two type 2 NTCDAs are always located next to each other, embedded between the lobes of two adjacent CuPc molecules (see orange highlighted area in Fig. 4.37 (c)). The NTCDA pair has the same in-plane orientation, but two differently aligned pairs are present, rotated 60° and -45° to the [-110] substrate direction. The type 1 NTCDAs do not appear in pairs, but in a row with alternating in-plane orientations of 60° and -45°, as indicated by the green ellipse in Fig. 4.37 (c). Additionally, each is located between the lobe of a CuPc molecule on one side and in the gap between the lobes of one CuPc on the other side. The type 1 NTCDAs are thus at a larger distance to the CuPcs than the type 2 NTCDAs.

dI/dV curves were also recorded for both types of NTCDA molecules and are shown in Fig. 4.37 (b). A broad peak appears at a bias of -300 mV for the spectra of the type 2 NTCDAs (displayed in orange, purple and light blue). In the spectra recorded between the pairs the peak is especially clearly visible (orange). This peak is also visible in the spectra measured above the type 1 NTCDA (in green and black), but less intense. The peak position of the type 1 and 2 NTCDAs is identical. This confirms that the LUMOs of all eight NTCDAs are (partially) filled and are shifted compared to the RML of NTCDA to higher binding energies. The peak position fits very well with the binding energy determined by UPS at LT, located at 0.35 eV. By orbital tomography it was analysed that the LUMO resonance is in contrast visible at a binding energy of 0.08 eV. However these ARPES data were recorded at RT and thus are not directly comparable with LT-STS data, as the UPS data indicate, that the binding energy of the NTCDA LUMO depends strongly on temperature. Nevertheless all methods have proven that the NTCDA LUMO is (partially) filled and the CuPc LUMO is probably empty.

4.5.2. The annealed intermediate phase

A. Ultraviolet photoelectron spectroscopy at room temperatures

The electronic properties of the annealed intermediate phase were determined by UPS, as shown in Fig. 4.38. The HOMO peak of CuPc (blue) has a binding energy E_B(HOMO) = 1.45 eV and the HOMO peak of NTCDA (magenta) is located at E_B(HOMO) = 2.43 eV. The LUMO peak (yellow line) can be fitted by a single Gaussian, is located at a binding energy of E_B(LUMO) = 0.2 eV and is therefore partially filled. As the

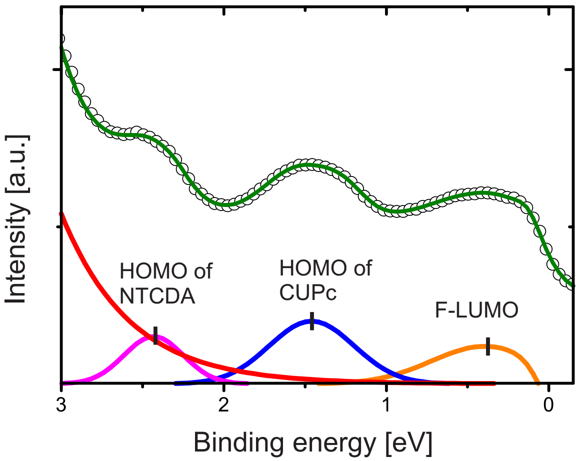

Figure 4.38.: Ultraviolet photoelectron spectrum of the annealed intermediate phase at room temperature. The molecular resonances are displayed in different colours.

molecular contribution to the LUMO peak can not be determined by UPS additional STS was performed.

B. Scanning tunnelling spectroscopy

A STM image of the annealed intermediate phase at 5 K is shown in Fig. 4.39 (a) and all inequivalent molecules are marked in different colours. The corresponding dI/dV curves recorded above all molecules contained in the unit cell are displayed in Fig. 4.39 (b).

The dI/dV curves recorded on the lobes and centres of the CuPc molecules (turquoise, yellow and red spectra) are almost flat. However at a bias of -350 mV a broad peak with low intensity is visible in all CuPc spectra. It is therefore difficult to evaluate whether it stems from a partially filled LUMO peak or just from tip states.

As already shown in chapter 4.3.1.C, the unit cell of the annealed IM phase consists of one CuPc and two NTCDA molecules, but defects are present in the ordered structure. There the two NTCDAs are located next to the NTCDAs of the next unit cell. In the constant height STM image shown in Fig. 4.39 (c), two of the NTCDAs (marked by a purple and orange circle), located at the defects, have a different electronic contrast than the other NTCDAs: the first and the fourth NTCDA in the defect rows are much brighter. The darker NTCDAs are called in the following type 1 and the brighter NTCDAs type 2.

The dI/dV curves of the type 2 NTCDAs (purple and orange), displayed in Fig. 4.39 (b), both exhibit a broad peak at a bias of -340 mV. This indicates that the LUMOs of the

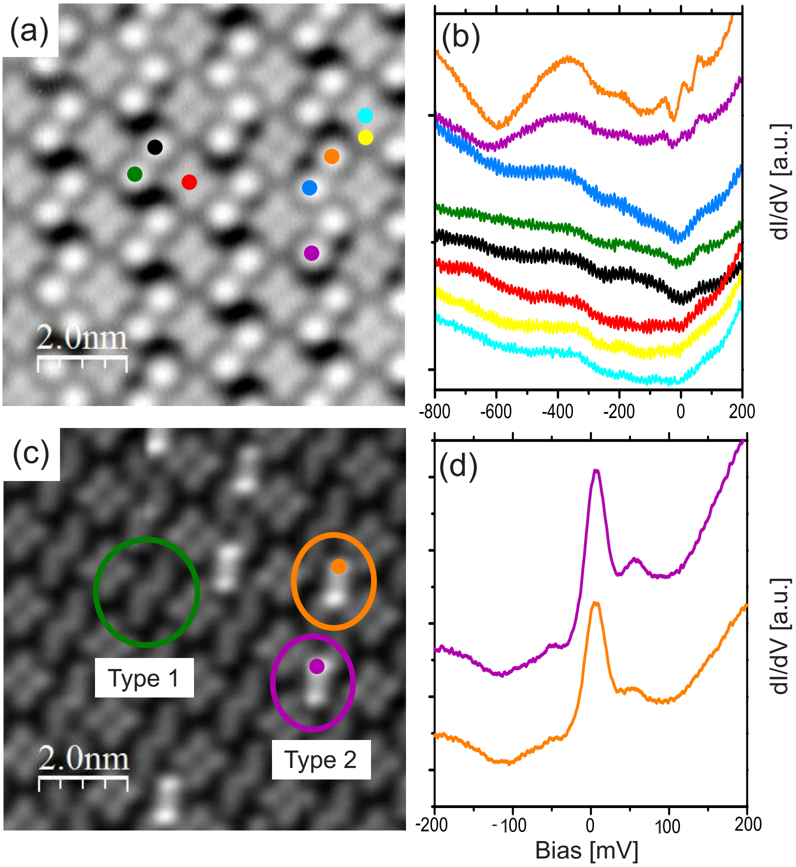

Figure 4.39.: (a) STM image of the annealed intermediate phase (I=0.05 nA, V=1.5 V). The coloured dots mark the different molecular positions where dI/dV spectra were recorded (T=5 K, modulation: ν=912 Hz, amplitude: 10 mV). (b) The corresponding spectra are shown on the right side of the image. (c) Constant height STM image, where two different types of NTCDA are highlighted (I=0.05 nA, V=50 mV). (d) dI/dV spectra of the type 1 NTCDAs with a z_{offset} = 1.25 Å.

type 2 NTCDAs are (partially) filled, as UPS data already indicated. In addition, at the Fermi level a sharp resonance was observed for both type 2 NTCDAs. Therefore spectra with a z offset, which causes a smaller tip-surface distance and thus a higher sensitivity, were recorded sweeping the bias from -200 mV to 200 mV, as displayed in Fig. 4.39 (d). This resonance might be a indication for a Kondo effect.

These are of interest, as a many-body resonance was observed earlier for the homomolecular structures of NTCDA and CuPc on Ag(111) [ZHK⁺12]. This effect appears if a coupling between an electron in a occupied molecular state and conduction electrons of the substrate occurs and leads to the appearance of either a peak or a dip at the Fermi level depending on the tunneling path of the electrons [THS09]. A pre-condition is in both cases a partially-filled state close to the Fermi level. This could be the reason that in the spectra of the CuPc molecules no dip or peak at U=0 V is visible, as shown in Fig. 4.39 (b) in the turquoise, yellow and red spectra. This effect should be investigated in the future in more detail, as this many-body resonance would be an additional channel for charge transfer. Many-body resonances lead to an energy gain and their occurrence depends on the adsorption sites of the molecules, thus they can have a influence on the structure formation of mixed molecular systems.

The spectra of the type 1 NTCDAs (shown in green, black and blue in Fig. 4.39 (b)) also reveal a less intense broad peak at a bias of approximately -340 mV, but a Kondo resonance at the Fermi level is not visible. Thus the LUMO of the type 1 NTCDA is probably also partially filled. By comparison of UPS data recorded at RT and STS data at LT, it can be concluded that the LUMO of NTCDA is shifted to approximately 140 mV higher binding energies due to cooling.

4.5.3. The CuPc-rich phase

A. Ultraviolet photoelectron spectroscopy at room and low temperature

The electronic structure of the CuPc-rich phase was measured by a UV-light source at I09 at Diamond in Didcot at room temperature. Afterwards the sample was cooled down to 60 K. The spectra at RT and 60 K are displayed in Fig. 4.40. The spectrum at room temperature shows a partially filled F-LUMO (yellow peak) close to the Fermi level at $E_B(\mathrm{LUMO}) = 0.37$ eV, which probably stems from NTCDA, as it was observed for the other mixed structures. The LUMO of NTCDA is superimposed by a sharp resonance located directly at the Fermi level, which probably arises from a many-body resonance.

Additionally, two peaks are visible in the energy regime of the HOMO of CuPc with binding energies of $E_B(\mathrm{HOMO}_1) = 1.26$ eV and $E_B(\mathrm{HOMO}_2) = 1.47$ eV, which belong to the two inequivalent CuPc molecules in the unit cell. The peaks of the NTCDA HOMO are located at $E_B(\mathrm{HOMO}_1) = 2.33$ eV and $E_B(\mathrm{HOMO}_2) = 2.54$ eV. However it should be mentioned that the HOMO-1 of CuPc is also in this energy regime, therefore one of the peaks could belong to this orbital as well.

In the spectrum of the cooled CuPc-rich phase it is clearly visible that three peaks appear close to the Fermi level. The peaks have binding energies of $E_B(\mathrm{LUMO}) = 0.54$ eV (yellow peak) $E_B(\mathrm{LUMO}) = 0.32$ eV (green peak) and $E_B(\mathrm{LUMO}) = 0.15$ eV (blue peak). From RT-STM images it is known, that at least two inequivalent NTCDA molecules are located in the unit cell, but it can not be excluded that further orientations exist due to the poor resolution of the images. The additional peaks could therefore either belong to the LUMOs of inequivalent NTCDAs or to the LUMO of CuPc. By UPS

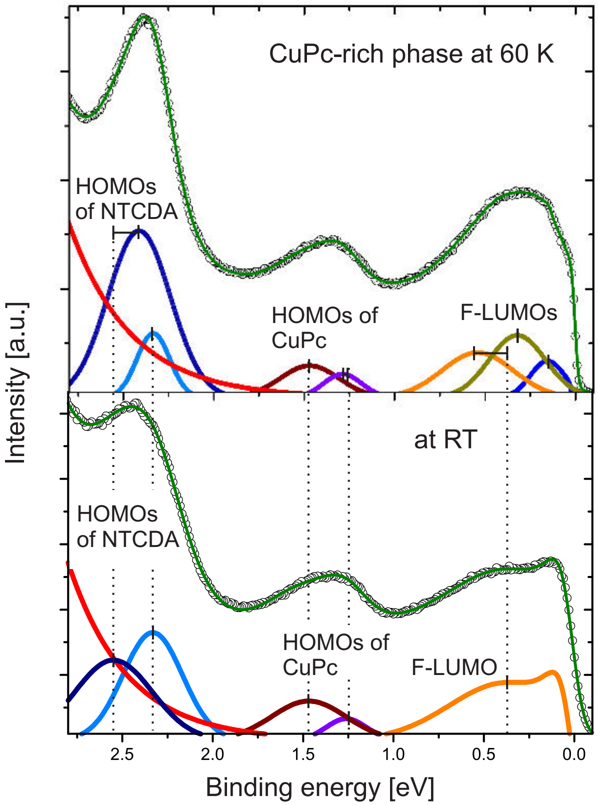

Figure 4.40.: Ultraviolet photoelectron spectroscopy data of the CuPc-rich phase in the upper part at 60 K and underneath at room temperature. The resonances of both molecules are plotted in different colours and the shifts due to temperature decrease are indicated by dashed black lines.

this can not be determined there ARPES and consequently orbital tomography has to be performed.

The sharp resonance at the Fermi level observed at RT disappears at LT, which should not be the case for a many-body effect. An explanation could be that the LUMO of NTCDA at LT is completely filled, in contrast to the RT data where it is only partially filled. A coupling between the molecules and the conduction electrons of the metal appears however only for a partially filled LUMO. This seems to be a reasonable explanation as the same effect was earlier observed by Ziroff et al. [ZHK$^+$12] for the RML of NTCDA on Ag(111).

The peaks of the CuPc HOMOs have a binding energies $E_B(\text{HOMO}_1) = 1.29$ eV and $E_B(\text{HOMO}_2) = 1.47$ eV at RT. At LT the HOMO_1 is shifted to 30 meV higher binding energies, but the HOMO_2 is found at the same binding energy as at RT.

The HOMO peaks of NTCDA have binding energies of $E_B(\text{HOMO}_1) = 2.33$ eV and $E_B(\text{HOMO}_2) = 2.41$ eV . Thus the HOMO_1 stays at the same position but the HOMO_2 shifts by 100 meV to lower binding energies. Note that the latter might also be caused by the vicinity of the HOMO-1 CuPc peak, which complicates the fit.

In conclusion, the HOMOs of NTCDA and CuPc changed their position in energy only slightly, but the more relevant observation is the appearance of three peaks close above the Fermi level.

B. ARPES and Orbital Tomography

To assign the origin of the peaks observed by UPS, ARPES data were recorded and analysed by orbital tomography. As it is known from STM, at least two NTCDA and two CuPc molecules are contained in the unit cell. Therefore four different theoretical maps have to be considered for the performance of an orbital tomography fitting procedure of the energy regime just above the Fermi level; these are shown in Fig. 4.41. In the theoretical momentum maps of the LUMO of NTCDA, the long axis of NTCDA is either aligned parallel to the [-110] direction (a) or rotated by 20° (b). In the theoretical momentum maps of the CuPc HOMO the lobes of the CuPc molecules are rotated by 65° (d) or 20° (e) to the [-110] direction. A constant binding energy (CBE) map at $E_B = 0.2$ eV of the measured data cube is displayed in Fig. 4.41 (c). In addition, the ARPES maps of the bare silver substrate were also recorded and the CBE map at 0.2 eV is shown in Fig. 4.41 (f).

The resulting PDOS versus binding energy is plotted in Fig. 4.42 (a). The plot indicates that the LUMOs of both inequivalent NTCDA molecules are partially filled (shown in green and magenta), but both CuPc LUMOs are unfilled (displayed in red and blue). As it was not possible to determine the precise in-plane orientation of the NTCDA molecules from RT-STM images, the fitting routine was performed again with a theoretical map where one NTCDA is rotated by 15°, instead of 20°. This small angular discrepancy causes a large difference in the intensity distribution of the momentum maps as can be seen by comparison of Fig. 4.42 (c) and Fig. 4.41 (b). Therefore LT-STM images are necessary to determine it more precisely. The other theoretical maps were kept and the fit was again performed. The result of this fit is displayed in Fig. 4.42 (b). The NTCDA 15° map now has the largest contribution and the NTCDA LUMO 0° map has a much smaller one. Instead the maps of both CuPc molecules contribute to the measured data cube. Therefore, it seems that the contribution of four different momentum maps leads to an under-determined system. The intensity maxima with a ring-like background of the measured momentum map, can either be created by a superposition of the theoretical maps of the NTCDA LUMO 0° and NTCDA LUMO 20° or by the superposition of two theoretical maps of CuPc 65°, NTCDA 15° and NTCDA 0°. The contribution only from both NTCDA maps seems to be more reasonable due to previous measurements,

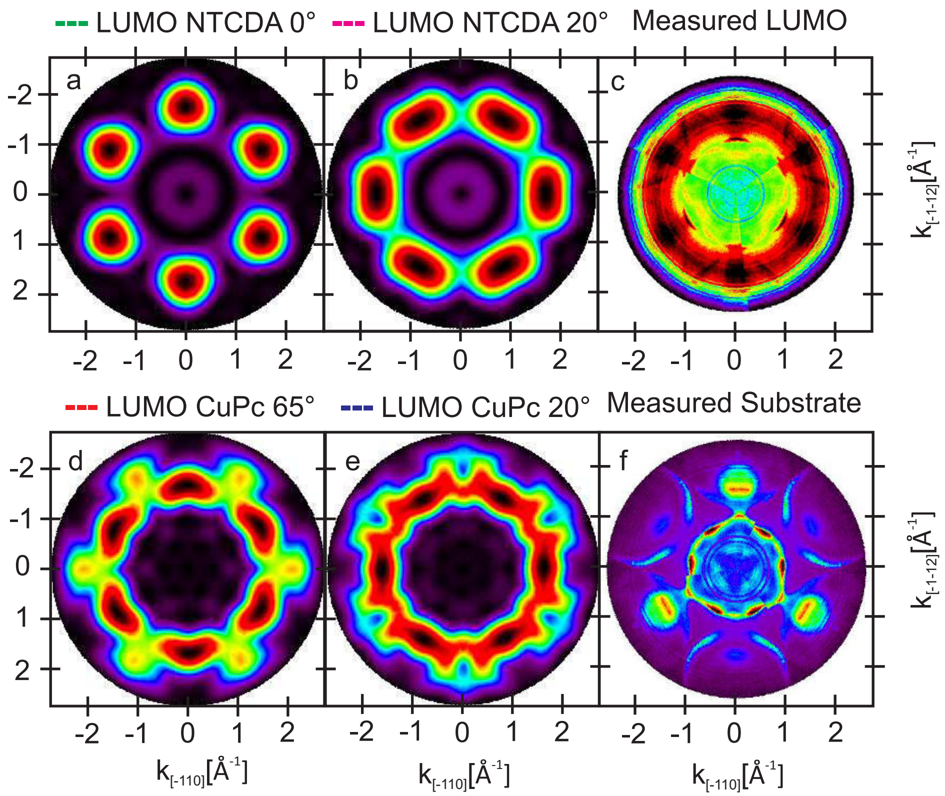

Figure 4.41.: LUMO CuPc- rich phase: The four theoretical momentum maps of (a) the NTCDA LUMO 0°, (b) the NTCDA 20°,(d) the CuPc 65° and in (e) the CuPc 20° are displayed. The measured LUMO momentum maps is shown in (c) and the measured silver substrate contribution in (f).

but at this point, obviously, the limit of orbital tomography is reached and it can not be identified unambiguously whether the LUMO of CuPc is partially filled or empty. The binding energy of the LUMO of NTCDA (for both fits the in-plane orientation with the strongest contribution) is however located at approximately E_B(LUMO) $= 0.30$ eV. This slightly deviates to the binding energy of 0.37 eV determined by UPS.

Angle-resolved intensity distributions in the energy regime of the HOMO of CuPc and NTCDA were measured as well. A deconvolution of these was possible as there were fewer contributing molecular maps, namely only two for each measured data cube. The measured CBE map of the HOMO of CuPc at $E_B = 1.4$ eV is displayed in Fig. 4.43 (a). The theoretical momentum maps representing the two different CuPc orientations, known

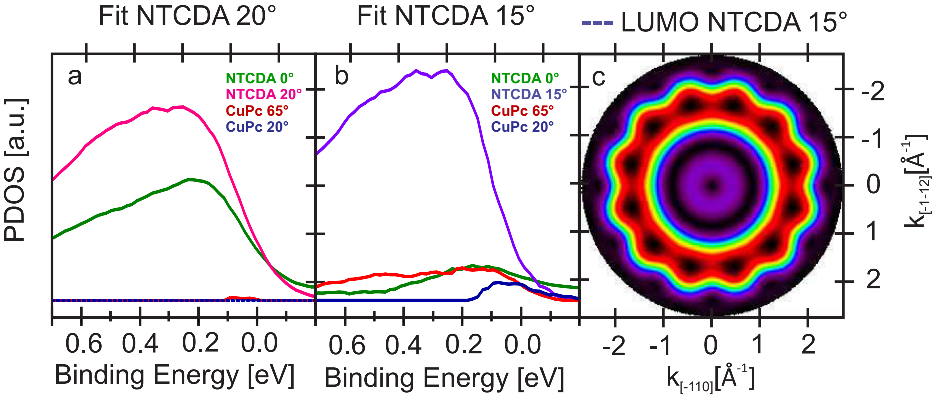

Figure 4.42.: The fit result, the PDOS, of the CuPc-rich phase is displayed for the energy regime just above the Fermi level. In (a) the theoretical momentum maps of the NTCDA 0° (green), NTCDA 20° (magenta), CuPc 65° (red) and the CuPc 20° (blue) contribute to the fit. In (b) the NTCDA 20° momentum map is replaced by NTCDA 15° (purple). (c) The theoretical momentum map for NTCDA 15°.

from STM images, were used for the fitting procedure, where the molecules are rotated either by 65° (b) or 20° (c) to the [-110] silver direction.

The result of the deconvolution, the PDOS versus binding energy, is shown in Fig. 4.43 (d). The maps of both molecular orientations contribute to the experimental data cube of the HOMO of CuPc, but the measured energy range of the ARPES data cube was too small, which means that only a part of CuPc HOMO 20° (blue) is contained in the ARPES data cube. The map of the CuPc 65° (red) has an almost five times larger contribution to the PDOS than the map of the CuPc 20° (blue). This fits to the results known from STM measurements, which revealed that the unit cell of the CuPc-rich phase contains four CuPc molecules rotated by 65° and just one by 20°.

The binding energies of the two orbitals differs strongly. The CuPc HOMO 65° has a binding energy of $E_B(\text{HOMO}_2) = 1.48$ eV and the CuPc HOMO 20° at $E_B(\text{HOMO}_1) = 1.10$ eV. The binding energies of the CuPc HOMOs determined by UPS, fitted by two peaks, are $E_B(\text{HOMO}_2) = 1.47$ eV and $E_B(\text{HOMO}_1) = 1.29$ eV. The binding energies of HOMO_2 determined by ARPES and UPS are therefore in good agreement. The binding energies of HOMO_1 differs for UPS and ARPES, but as already mentioned a reason could be that only a part of the HOMO_1 is contained in the recorded APRPES data cube.

The angular distribution of the HOMO of NTCDA was also recorded and the corresponding CBE map with a homogeneous ring-like intensity distribution is displayed in Fig. 4.44 (a) at a binding energy of $E_B = 2.5$ eV. The deconvolution was performed by the two theoretical momentum maps, which are shown in Fig. 4.44 with

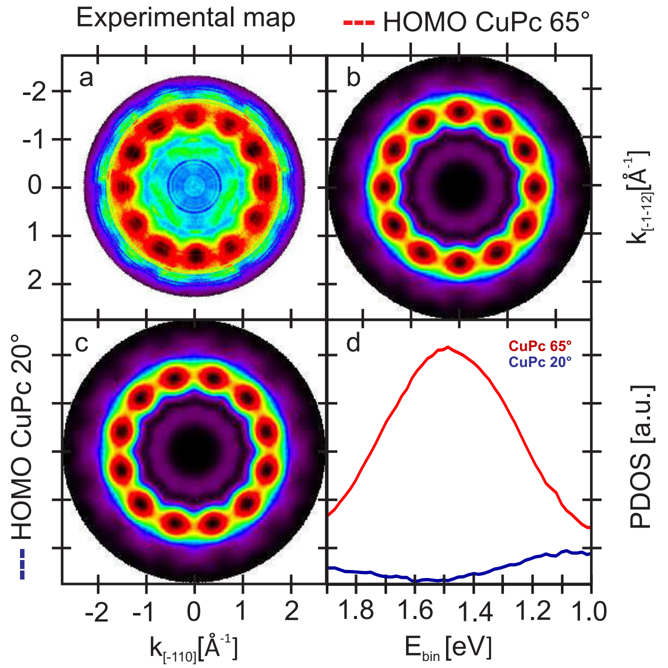

Figure 4.43.: (a) The experimental CBE momentum map at 1.4 eV in the energy regime of the CuPc HOMO in the CuPc-rich phase. The theoretical CBE maps with CuPc rotated 65° (b) and 20° (c) to the [-110] direction used for the orbital tomography fitting routine. (d) The PDOS of the maps of CuPc rotated by 65° in red and the 20° contribution in blue.

NTCDA molecules rotated by 0° (b) and 20° (c) to the [-110] direction. The subsequent PDOS of the two molecular orientations, 20° in magenta and 0° in green, are plotted in Fig. 4.44 (d). Both orbitals have the same binding energy of $E_B = 2.42$ eV. The binding energies determined by UPS differ with $E_B(\mathrm{HOMO}_1) = 2.33$ eV and $E_B(\mathrm{HOMO}_2) = 2.54$ eV. A reason for the mismatch could be that the in-plane orientation of the NTCDAs is not determined exactly and/or that the HOMO-1 of CuPc is located in the same energy regime, which can deliver additional intensity to our experimental ARPES data cube.

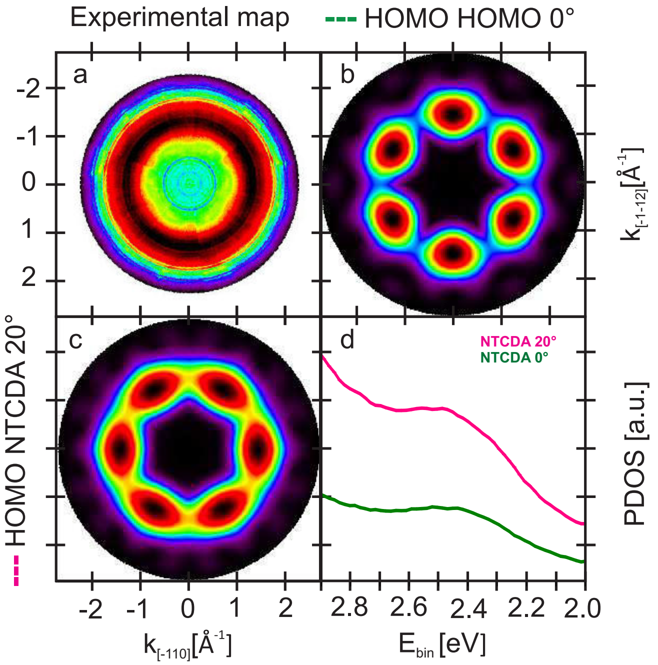

Figure 4.44.: (a) The experimental CBE momentum map at $E_B =$ 2.5 eV of the NTCDA HOMO in the CuPc-rich phase. The theoretical maps with NTCDA rotated 0° (b) and 20° (c) to the [-110] direction. (d) The PDOS of NTCDA rotated by 0° in green and the 20° contribution in pink.

4.5.4. Comparison of electronic properties

The electronic properties of the NTCDA- and CuPc-rich phases and the annealed intermediate phase were investigated by UPS, ARPES and STS.

For comparison, the results of the UPS experiments are plotted next to the spectra of the homomolecular structures of NTCDA (blue) and CuPc (black) in Fig. 4.45. The curves are arranged from top to buttom with increasing CuPc and decreasing NTCDA content.

All spectra clearly show a resonance below the Fermi level, which leads to the conclusion that the former LUMO of all these phases is partially filled. Additionally, peaks stemming from the HOMOs of NTCDA and CuPc are visible. The exact binding energies are listed in the table included in in Fig. 4.45 and differ depending on the structure and molecular orientation. This is caused by the large unit cells of the mixed NTCDA-CuPc phases, which lead on the one hand to at least two NTCDA and CuPc in-plane orientations and on the other hand to different adsorption sites and neighbours for each molecule and to various distances between them. Therefore many molecular orbitals

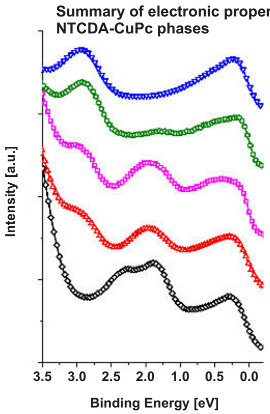

	HOMO NTCDA [eV]		HOMO CuPc [eV]		LUMO [eV]	
	RT	LT	RT	LT	RT	LT
RML of NTCDA	2.45	-	-	-	0.17	-
NTCDA-rich phase	2.31 2.50	2.31 2.58	1.34	1.39	0.25	0.35
Annealed intermediate phase	2.43	-	1.45	-	0.20	0.35 [V]
CuPc-rich phase	2.33 2.54	2.33 2.41	1.26 1.47	1.29 1.47	0.37	0.54 0.32 0.15
CuPc (bi)-layer	-	-	1.37	-	0.15	-

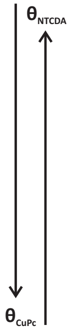

Figure 4.45.: Valence band spectra determined by UPS of the relaxed monolayer NTCDA (blue), the NTCDA-rich phase (green), annealed intermediate phase (magenta), CuPc-rich phase (red) and the CuPc monolayer (black) in the binding energy regime which contains the former LUMO, the CuPc HOMO (around $E_B = 1.4\ eV$) and the NTCDA HOMO (around $E_B = 2.45\ eV$). The CuPc content of the different structures increase from top to bottom. The table on the right side contains the binding energies of the HOMOs of CuPc and NTCDA and for the former LUMO for all investigated systems.

overlap and make a proper deconvolution partly very difficult, as it was shown for the LUMO energy regime of the CuPc-rich phase.

Nevertheless a correlation between the adsorption geometry and the electronic properties can be obtained for the different phases:

The unexpectedly low adsorption heights of the molecules, which was found for the NTCDA-rich phase at RT, lower than in both homomolecular structures, could arise for different adsorption heights of the type 1 and 2 NTCDA molecules. This assumption is based on STS measurements where the intensity of the local density of states varies strongly depending on whether the spectrum is recorded at a type 1 or 2 NTCDA. Taking STS and orbital tomography together, we conclude with a rather high certainty that only the former LUMO of NTCDA is partially filled and the LUMO of CuPc is unpopulated. Furthermore, as found for the homomolecular structure of PTCDA on Ag(111) [KHT$^+$08], the LUMO shifts to higher binding energies upon cooling. This proofs that the lower adsorption heights determined by XSW experiments for LT structures, are connected to a stronger binding of the molecules to the surface.

Similar observation were made for the annealed intermediate phase. The binding energies of the LUMO and the HOMOs are very similar to the values determined for the NTCDA-rich phase. The intensity of dI/dV differs however above the type 1 and

2 NTCDAs. A many-body effect was found as a sharp peak at the Fermi level. This peak was only found for NTCDAs, which are ordered in a "defect"- structure. The adsorption heights of the molecules in this phase were not recorded and therefore it can not be determined how the additional resonance influences the adsorption height. This enables an additional channel for charge transfer, which could have an influence on the formation of the laterally mixed structures. To confirm this finding, measurements have to be performed with an optimised experimental set-up and multiple times to improve reliability. However, it proves that differently ordered structures, in which the molecules consequently have different adsorption sites, influence the electronic properties.

The LUMO of the NTCDA molecules contained in the CuPc-rich phase is located at higher binding energies compared to the other mixed systems. A reason for this effect could be the lower NTCDA to CuPc ratio in this phase; Each NTCDA molecule has to accept more charge from the adjacent CuPcs. Nevertheless, the adsorption height of the carbon backbone of both molecules changes only slightly due to mixing at RT, but decreases by 0.13 Å upon cooling. The LUMO shifts by 0.17 eV to higher binding energies and two further peaks appear below the Fermi level. This proves, as it was already observed for the NTCDA-rich phase, that cooling causes more charge to be pushed to the NTCDAs, which reduces the charge spill out from the substrate and consequently leads to lower adsorption heights. The CuPcs align their adsorption height to the NTCDAs, but most probably the LUMO of CuPc is depleted.

The investigation of the electronic properties of the laterally mixed NTCDA-CuPc structures is in good agreement with results from the thesis of Stadtmüller. In particular, we also found that the original character of the molecules is enhanced upon mixing the different molecules [SLW⁺14]: NTCDA becomes a stronger charge acceptor and CuPc turns from a weak electron acceptor to an electron donor. This indicates that although NTCDA is a weaker acceptor than PTCDA, it is still strong enough to (probably completely) attract the charge from the CuPc LUMO.

However, cooling affects the heterostructures of NTCDA and CuPc differently than the mixed systems of PTCDA and CuPc. The adsorption heights of the molecules in the PTCDA-CuPc systems change only slightly upon cooling. This can be explained by the electronic properties of both heteromolecular systems. The LUMO of PTCDA is already (almost completely) filled at RT in the mixed PTCDA-CuPc structures. Additional charge can therefore not be transferred to the LUMO of PTCDA during cooling which leads to almost unchanged adsorption heights of both molecules. This situation is different for the LUMO of NTCDA in the mixed NTCDA-CuPc structures, which is only partially filled. Additional charge can be pushed to the NTCDA molecules at LT, which consequently lowers the adsorption height.

5. Stacked heteroorganic systems

5.1. Introduction

The laterally mixed heterostructures of NTCDA and CuPc on Ag(111) have been intensively studied in the last chapter. We could improve the understanding of the interplay of intermolecular and molecule-substrate interaction, and understood the charge redistribution between the molecules via the substrate. An alternative way of producing mixed molecular films is stacking homomolecular layers. The investigation of such stacked organic heterostructures is also very important for the future development of efficient organic devices. They also have been only rarely studied until now [YHJ03],[SSHT$^+$01],[Kle13], [SGP$^+$14], [SWS$^+$15].
In this chapter we want to determine the interaction between two organic layers on top of a metal substrate. One of the most important questions is, whether the molecules grow in a long rang order in the second layer or the molecules of the first and second layer exchange, as it was earlier observed for PTCDA on a monolayer of CuPc on Ag(111) [Sta13]. Therefore we have studied three similar systems of stacked heterostructures consisting of NTCDA and CuPc molecules on Ag(111). CuPc molecules on top of a closed monolayer of NTCDA on Ag(111) were investigated, first on a relaxed monolayer of NTCDA and in a second try on a compressed monolayer of NTCDA. SPA-LEED revealed that the CuPc molecules arrange in a long range ordered film in the second layer. The electronic properties were investigated by ARPES and orbital tomography. This enabled us to study the bonding strength of the molecules and the molecular orientation of the CuPc molecules in the second layer. Additionally, the inverse system, NTCDA on a monolayer of CuPc on Ag(111), has been investigated by SPA-LEED before and after annealing.

5.2. CuPc on a relaxed monolayer of NTCDA on Ag(111)

5.2.1. Lateral structure

The long range order of CuPc molecules on a closed relaxed monolayer of NTCDA was investigated by SPA-LEED. The relaxed monolayer of NTCDA was prepared by mulitlayer desorption (see chapter 2). Changes of the diffraction pattern due to the additional deposition of CuPc were observed in situ by SPA-LEED. A SPA-LEED image of the pristine relaxed monolayer of NTCDA, integrated for approximately 25 minutes,

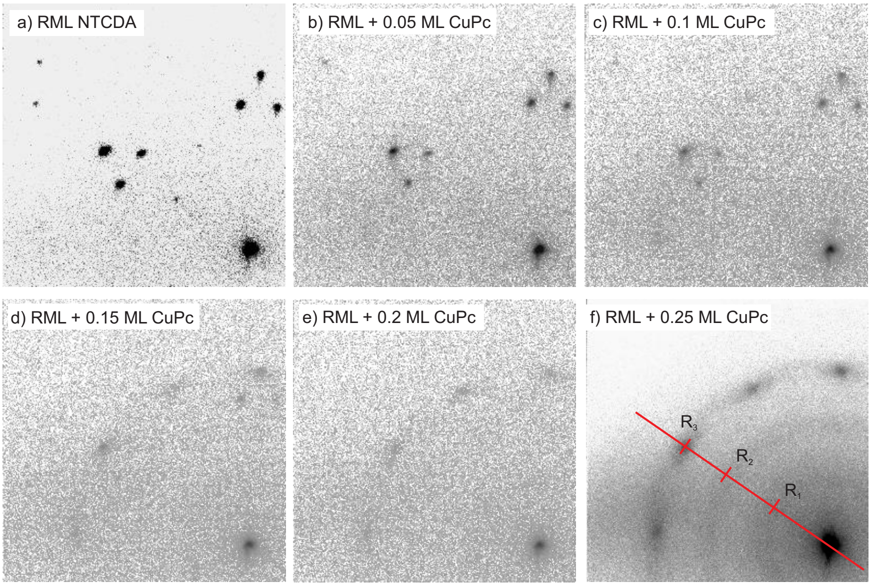

Figure 5.1.: (a) SPA-LEED image of a RML of NTCDA. (b) SPA-LEED image of a RML of NTCDA with 0.05 ML CuPc on top, (c) 0.1 ML CuPc, (d) 0.15 ML CuPc (e) 0.2 ML CuPc and (f) 0.25 ML CuPc. The images were all recorded at 27.2 eV.

is shown in Fig. 5.1 (a). The spots reflect the characteristic diffraction pattern of the RML of NTCDA on Ag(111). CuPc molecules were deposited on top with a rate of 0.05 ML per minute. After every minute a SPA-LEED scan was measured as displayed in Fig. 5.1(b-e). At a low CuPc coverages (0.05 ML), the spots belonging to NTCDA are still clearly visible (b, c). However they become less intense and almost disappear in (d), where a modulated ring appears at the same time. The NTCDA spots have completely vanished in (e). A high statistic SPA-LEED image is shown in (f), in which a modulated ring emerged, but also two diffuse rings with smaller radii. The intensity of a line scan along the direction of the (0,0) spot and one of the maxima of the modulated ring (red line in (f)) was measured with a long integration time (see Fig. 5.2(b)).

The line scan enabled us to determine the radii R of these rings, which should explain the change of the lateral geometry by the adsorption of CuPc. The reciprocal radii were transformed in real space distances d by calculating $d = \frac{2\pi}{R}$. The inner ring has a radius of $R_1 = (0.286 \pm 0.005)$ Å^{-1} and reflects a real space distance of $d_1 = (22.0 \pm 0.2)$ Å. The scattering intensity arises from disordered CuPc molecules with a certain nearest neighbour distance d. This effect was already observed for the submonolayer regime of CuPc on Ag(111) [KSS+10]. Kröger et al. determined a dependence between the ring radius R and the CuPc coverage Θ with $d = \frac{2\pi}{R} \propto \frac{1}{\sqrt{\Theta}}$.

For the stacked system the question arises whether the CuPc molecules causing the intermolecular ring are located in the first layer. At a very low coverage the NTCDA spots were still visible, but at a CuPc coverage of 0.2 ML they are gone (see Fig. 5.2 (f)). An explanation for the vanishing reflections belonging to NTCDA, at such a low CuPc coverage, is that CuPc molecules diffuse from the second organic layer into the relaxed monolayer of NTCDA, and fill the space between the NTCDA molecules until the monolayer is most densely packed. Possibly also some exchange with NTCDAs in the first layer. This destroys the long range order of the NTCDA domains, which leads to the disappearance of the NTCDA spots in the LEED image. However when the most densely packed first layer is formed, the residual CuPc molecules can not penetrate into this layer any more and grow on top where they form a 2D gas, similar as for the homomolecular structure of CuPc on Ag(111) [KSS^{+}10].

The real space distance of $d_1 = 22.0\,\text{Å}$ at a CuPc coverage of 0.25 ML matches well with the 22.2 Å determined for pristine 0.27 ML CuPc on Ag(111), as it was determined from line scans by Kröger et al. [KSS^{+}10] (see Fig. 5.3). This demonstrates that only a small amount of CuPc molecules penetrates into the first organic layer, and most of the molecules form a 2D gas in the second layer.

The outer ring at $R_3 = (0.835 \pm 0.005)$ Å^{-1} is modulated and shows twelve intensity maxima in the [-110], [0-11], [10-1], [-1-12], [2-1-1] and [-12-1] substrate directions. The corresponding real space distance is d_3 =(7.5 ± 0.2) Å , which is in good agreement with the real space distance (7.5 Å) of the second ring of the homomolecular submonolayers of CuPc on Ag(111). Kröger et al. explain it by intramolecular scattering which is proven by a Fourier transform of the total electron density of a free CuPc molecule. Modulations of the ring for the homomolecular CuPc structures were only observed when the systems was cooled down to $T = 140K$. Then the wings of CuPc were azimuthally aligned along the $<$-110$>$ directions of the substrate, which is probably caused by the condensation of the molecules on energetically most favourable adsorption sites.

A intermediate ring is clearly visible in Fig. 5.1 and Fig. 5.2 with a radius R_2 of (0.560 ± 0.005) Å^{-1}, which corresponds to a real space distance of d_2 =(11.2 ± 0.2) Å and was not observed for the homomolecular structures of CuPc. The radius is however almost exactly twice the radius of R_1. Firstly, it could reflect the second diffraction order of the inner ring, as the azimuthal order of the CuPc molecules on top of the monolayer of NTCDA increased. Secondly, it can arise due to a certain distance between the NTCDA molecules. The later is more probable as the NTCDA molecules exhibit in the homolecular monolayers a similar distance to each other in one direction of the unit cell of the CML: 11.07 Å and RML: 11.57 Å.

This section showed us that the NTCDA molecules leave their optimum adsorption sites and the RML structure is lifted, when CuPc molecules are deposited on top. The CuPc molecules can therefore diffuse into the first layer, where they have a direct contact to the silver substrate. The energy gain due to the adsorption of CuPc molecules directly on the silver substrate has therefore to be larger than the energy reduction caused by the loss of the optimum adsorption sites of the NTCDA molecules.

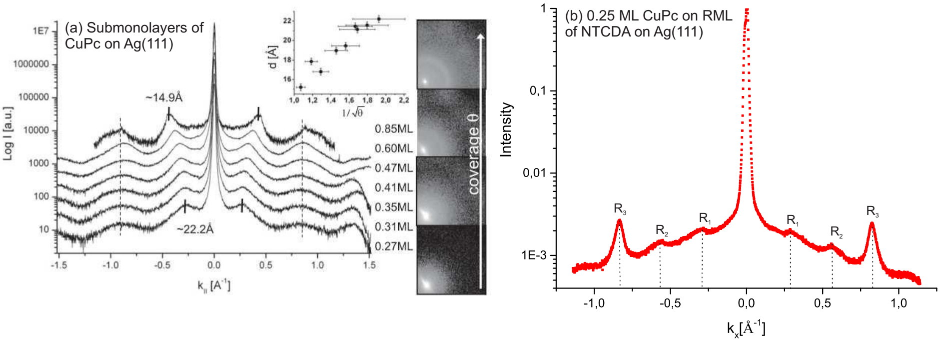

Figure 5.2.: (a) SPA-LEED line scans through the diffuse rings of CuPc on Ag(111) at different submonolayer coverages (reproduced from [KSS+10]). (b) Line scan through the diffuse rings of the SPA-LEED image shown in Fig. 5.1 (f), recorded for 0.25 ML of CuPc on a RML of NTCDA on Ag(111). The line scan direction is indicated by a red line.

Lateral structure of CuPc grown on a RML of NTCDA cooled to 95 K on Ag(111)

In an additional experiment, a relaxed monolayer of NTCDA was deposited on a clean Ag(111) crystal and was cooled afterwards down to 95 K. Subsequently 0.7 ML of CuPc molecules were evaporated on this cooled NTCDA layer. The aim of this experiment was to test whether the CuPc molecules stay on top of the NTCDA layer when their thermal energy is reduced. The experiment showed, despite the high CuPc coverage, that the NTCDA layer stayed intact as shown in Fig. 5.3 (a). The diffraction pattern of the relaxed monolayer of NTCDA is still visible. Additionally, only one diffuse ring appeared, the radius of which was determined by a line scan. It is shown in Fig. 5.3 (b), together with the measurement at RT reported in the previous section. The ring has a radius of $R_{1cooled}$ =(0.46 ± 0.01) Å^{-1} at 95 K and therefore corresponds to $d_{1cooled}$ =(13.5 ± 0.4) Å in real space. It reflects the smaller CuPc intermolecular distance, present at LT due to the higher amount of CuPc molecules deposited. This value is however larger than the radius of the highest observed CuPc coverage of 0.85 ML on Ag(111). This indicates that the CuPc molecules, which are very densely packed, can still arrange in a disordered structure at LT, while the same packing density leads for the homomolecular structure of CuPc at RT to a ordered structure.

This experiment mainly showed, that the NTCDA structure remained intact at low temperatures despite an additional adsorption of CuPc molecules on top. This can only be the case if potential barriers exit for the molecules, which they have to cross. The NTCDAs i.e. have to leave their commensurate adsorptions sites, which enables the CuPcs to diffuse into the first layer. A second barrier has to be overcome for exchanging the NTCDAs in the first layer to the second layer, which leads afterwards to a diffusion

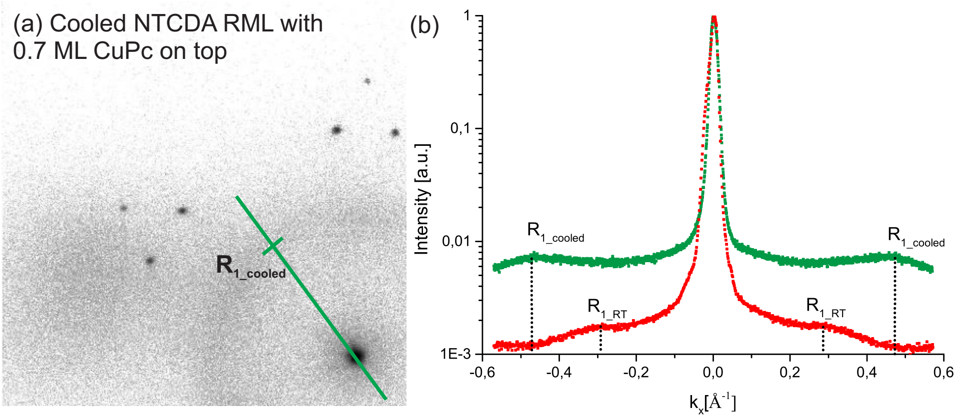

Figure 5.3.: A relaxed monolayer of NTCDA on Ag(111) cooled down to 95 K was prepared. Subsequently 0.7 ML of CuPc were deposited on top. The corresponding SPA-LEED image is shown in (a). A line scan direction is indicated by a green line and the line scan is displayed in (b). The line scan of the relaxed monolayer structure of NTCDA on Ag(111) at RT is plotted in red for a better comparison of both structures.

of CuPcs in the first layer. At room temperature the thermal energy is sufficient for overcoming these barriers, which is not the case at low temperatures.

5.2.2. Electronic properties

The electronic structure of this system has been measured at Bessy II by UPS and ARPES. Because of a bad calibration of the evaporation source 1.0 to 1.5 monolayer of CuPc were deposited on top of the relaxed monolayer of NTCDA. The diffraction spots of the RML of NTCDA were not visible and only diffuse intensity was detectable. The corresponding UPS spectrum is displayed in Fig. 5.4 (a). Two HOMO peaks are visible, located at binding energies of 1.07 eV and 1.38 eV, probably corresponding to CuPc molecules in the first and second layer. This confirms our findings from SPA-LEED, that CuPc molecules penetrate into the layer of NTCDA.

The SPA-LEED experiment led to the conclusion that just a little amount of the CuPc molecules penetrates into the first layer and the residual CuPcs stay on top in the second layer. Thus the peak of the CuPc molecules arising from the second layer should have a larger intensity than the peak stemming from the CuPcs located in the first layer. The smaller peak has a binding energy of $E_B(HOMO_1)$ = 1.38 eV, which is identical to the binding energy determined in chapter 4 for the HOMO of CuPc in the mixed heteromolecular structures of NTCDA and CuPc, which is a second strong indication for this peak steming from the first layer CuPc.

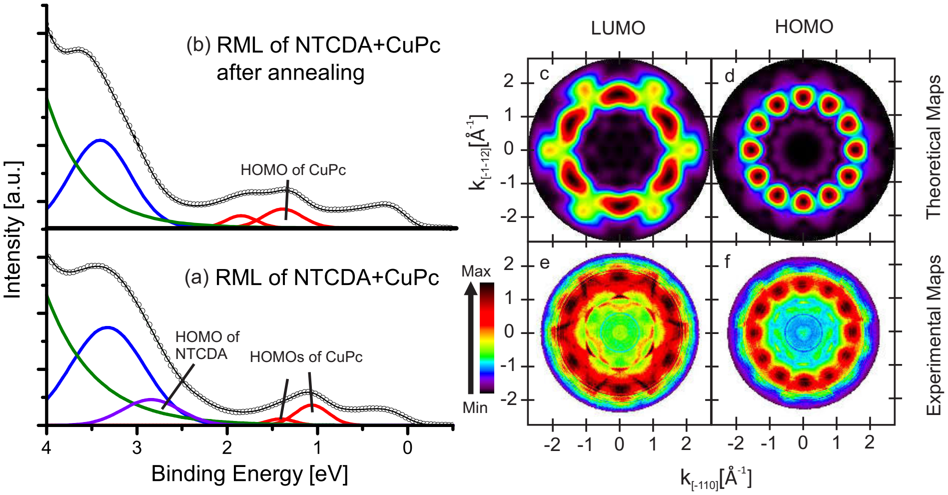

Figure 5.4.: (a) UPS spectrum of the relaxed monolayer of NTCDA with CuPc on top on Ag(111) at room temperature. (b) UPS spectrum of the same sample after annealing to around 500 K. The red peaks correspond to the HOMOs of CuPc in the first and second layer. The purple peak reflects the HOMO of NTCDA. The blue peak belongs probably to the HOMO-1 of CuPc. The green line arises from inelastically scattered photoelectrons. (c) Theoretical map of the LUMO and (d) HOMO of CuPc. (e) Measured CBE maps at E_B=0.2 eV and (f) at E_B=1.26 eV.

The second HOMO peak of CuPc, however, has a surprisingly low binding energy of 1.07 eV, while the bilayer HOMO peak has a binding energy of 1.6 eV in a homomolecular monolayer [KSS$^+$10]. The interaction with the first layer, consisting of NTCDA and CuPc molecules leads probably to a different charge redistribution which influences the binding energies of the orbitals. The similar effect was observed for the stacked system of CuPc on a monolayer of PTCDA on Ag(111). For this system, the HOMO of the second layer CuPc was even found at a binding energy of 0.9 eV, around 0.2 eV lower than for the system under study [SSK$^+$12].
The HOMO of NTCDA lies at a binding energy of 2.84 eV (see purple peak in Fig. 5.4 (a)). The HOMO of the homomolecular structure of NTCDA is located at 2.4 eV in a monolayer and at 3.4 eV in a multilayer [BFS$^+$07]. The purple peak probably consists of two contributions of NTCDA molecules located in both layers, but the superposition with the resonance of the HOMO-1 (shown in blue) hinders a proper separation of both HOMOs of NTCDA.

The UPS spectrum of the same system after annealing to approximately 500 K is shown in Fig. 5.4 (b). The uncertainty of the determined temperature is very large (± 100 K). The HOMO$_{first}$ of CuPc lies at $E_B(HOMO_1)$ =1.26 eV. A further peak is visible at $E_B(HOMO_2)$ =1.71 eV and corresponds to the HOMO of CuPc arising from the second layer. Both values are now in good agreement with binding energies determined from a bilayer of CuPc on Ag(111) [KSS$^+$10].

Additionally ARPES data cubes were recorded in the energy regime of the HOMOs of CuPc and the LUMO. The corresponding CBE maps at E_B = 0.2 eV and E_B =1.26 eV are displayed in Fig. 5.4 (e) and (f). The comparison of these maps with theoretical momentum maps of the LUMO (c) and HOMO (d) clearly proof that the intensity distribution of the ARPES maps reflect a well ordered CuPc film. This is a first indication, that the there are no NTCDA molecules left in the first layer or actually in the whole organic film, as the NTCDA HOMO peak has vanished in the UPS spectrum.

The photoelectron spectroscopy experiments are in good agreement with SPA-LEED results, and indicate that some CuPc molecules exchange with NTCDA molecules of the relaxed monolayer and the residual CuPc molecules adsorb in the second layer. The NTCDA molecules desorb when the sample is annealed at 500 K. These experiments indicate that it is energetically more favourable that CuPc molecules adsorb directly on the silver substrate, adjacent to NTCDA molecules until the first layer is most densely packed, instead of adsorbing only in the second layer.

5.2.3. Desorption behaviour

Since desorption of NTCDA was found in the ARPES experiments, we have investigated this behaviour in more detail using our SPA-LEED instrument. The stacked system of a relaxed monolayer of NTCDA with 0.25 ML of CuPc molecules on top on Ag(111) was annealed in steps of approximately 20 K for 10 minutes. After each annealing cycle a SPA-LEED scan was measured for circa 20 minutes at room temperature. In Fig.5.5 (a) a SPA-LEED pattern of the stacked system is shown at room temperature. Already after heating to 445 K, the diffraction pattern of the modulated ring vanishes and the spots of one of the laterally mixed NTCDA-CuPc structures, the NTCDA-rich phase appeared (Fig. 5.5 (b)). This indicates that more NTCDA molecules desorbed from the first layer which consequently allows for the diffusion of additional CuPc molecules from the second into the first layer, where they can form a mixed structure with the remaining NTCDA molecules.

During the next annealing cycles, the characteristic spots of the NTCDA-rich phase, in particular the triangle, diminish (5.5 (c)). After annealing to 500 K additional spots appear (d), which correspond to the intermediate phase. This implies that further NTCDA molecules desorbed and consequently the ratio of CuPc to NTCDA increased 1:2. Since only 0.25 ML of CuPc was deposited, the surface is not completely covered any more. After annealing to 575 K only one of the intermediate structures remains (IM2) (Fig.

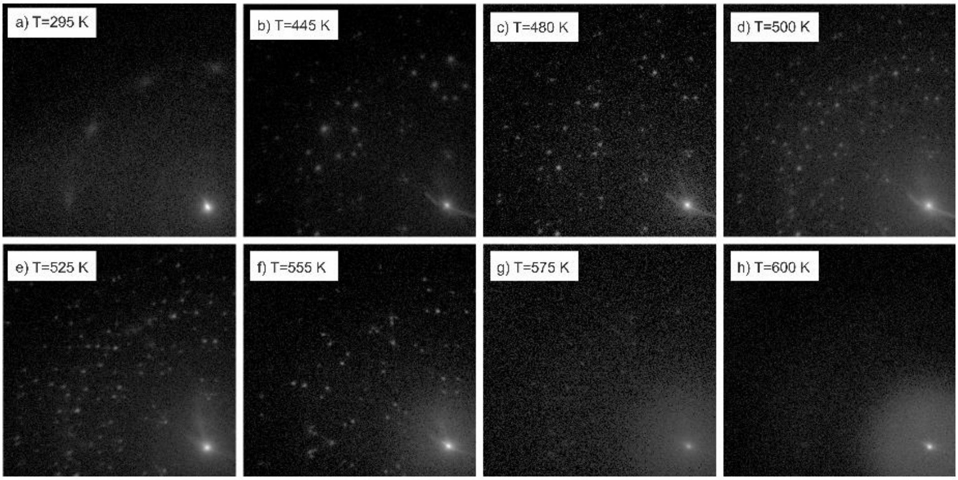

Figure 5.5.: (a) Temperature induced phase transitions of a relaxed monolayer NTCDA with CuPc on top measured by SPA-LEED, all at 27.2 eV. (b) After annealing to 445 K a transition to the NTCDA-rich phase occurs which changes due to higher annealing over (c) and (d) in the intermediate phase (e). In (f) just the diffraction pattern of the superstructure of the 1:1 phase (IM2) remained, which is even almost gone at 575 K in (g). After annealing to 600 K only a diffuse CuPc ring was left (h).

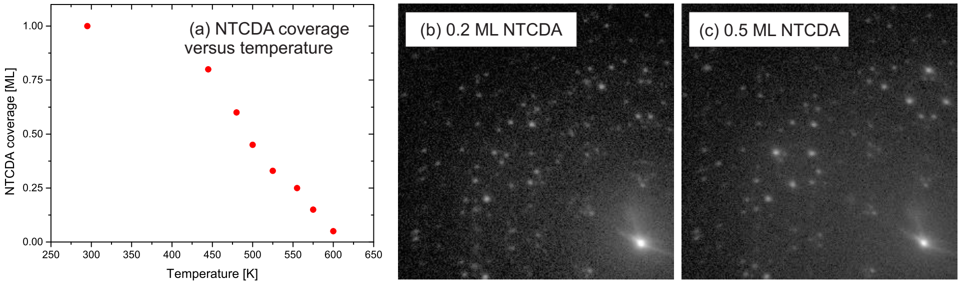

Figure 5.6.: (a) NTCDA coverage, determined from SPA-LEED images shown in Fig. (5.5, depending on the annealing temperature. (b) SPALEED images after the additional deposition of 0.2 ML and (c) further 0.3 ML of NTCDA molecules (27.2 eV). After the first deposition, the molecules form a superimposed intermediate and the NTCDA-rich phase. Further 0.3 ML NTCDA led to a pure NTCDA-rich phase.

5.5 (f)) and heating to 600 K leads to a diffuse ring of CuPc only (Fig.5.5 (g) and (h)). That indicates that basically all NTCDA molecules desorbed from the surface. The known NTCDA and CuPc coverage of the different ordered mixed structures allows to determine the NTCDA coverage depending for every annealing temperature, as it is plotted in Fig. 5.6 (a). This enables us to prepare the desired mixed structures easily by annealing.

In an additional experiment was tested whether NTCDA molecules are still on the surface after annealing at 600 K or all are already desorbed at this temperature, as the SPA-LEED image in Fig.5.5 (h) indicates. Therefore additional 0.2 ML (and in a second step 0.3 ML) of NTCDA were deposited on the diffuse CuPc phase. As we know which phase should be formed if a certain amount of NTCDA is additionally deposited to the 0.25 ML of CuPc, we can conclude whether NTCDA was still located at the sample or all molecules desorbed. It can be excluded that CuPc molecules were desorbed due to annealing, because a bilayer of CuPc on Ag(111) desorbs at a temperature of 580 K.

In Fig. 5.6 (b) the SPA-LEED image of a well ordered superposition of the intermediate and NTCDA-rich phase is visible, which was formed after the deposition of 0.2 ML of NTCDA. The appearance of these structures indicates, that some NTCDA molecules were still present on the surface, since at least a NTCDA coverage of 0.3 ML is needed for the formation of the observed structures. The second deposition of 0.3 ML of NTCDA leads to a pure NTCDA-rich phase, as shown in Fig. 5.6 (c). This experiment proofs that approx. 0.05-0.1 ML of NTCDA must have remained on the surface after annealing to 600 K. It also shows that the transformation of the mixed NTCDA-CuPc structures is a reversible process.

This observed desorption behaviour differs from that of PTCDA and CuPc heterostructures. In stacked systems with CuPc on top of PTCDA on Ag(111), annealing is necessary for a diffusion of CuPc molecules into the ordered PTCDA layer. Interestingly, the CuPc molecules desorb at a lower temperature as PTCDA. Therefore it is possible to mix the inverse system of a monolayer of CuPc with PTCDA on top into lateral mixed systems. This allows a transformation of the mixed Zig-Zag phase (CuPc-rich phase) by annealing in the One-to-One phase and Mixed Brick Wall structure (PTCDA-rich phase).

5.3. CuPc on a compressed monolayer of NTCDA on Ag(111)

5.3.1. Lateral structure

In this section a compressed monolayer of NTCDA with CuPc on top has been studied. We investigated whether a molecule exchange between CuPc and NTCDA occurs or the CuPc molecules stay on top of the denser packed compressed monolayer of NTCDA. Therefore, at first the lateral order of CuPc molecules adsorbed on a compressed monolayer of NTCDA was investigated by SPA-LEED. The SPA-LEED image of the homomolecular compressed monolayer of NTCDA was already shown and discussed in chapter 3. The additional deposition of 0.5 monolayer of CuPc on top leads to the appearance of new broad spots in the diffraction pattern, highlighted by blue ellipse in Fig. 5.7 (a). However the diffraction pattern of the compressed monolayer of NTCDA remains visible at the same time (red dots).

This finding poofs that the CML of NTCDA stays intact upon the adsorption of CuPc molecules, in contrast to the relaxed monolayer of NTCDA, where the diffraction spots of the NTCDA monolayer vanish. The appearance of broaden spots (blue ellipses) rather than a diffuse ring, indicates that the lobes of the CuPc molecules are aligned along the high symmetry directions of the Ag(111) substrate even at room temperature, in contrast to the homomolecular submonolayer structures of CuPc, where an alignment of the molecules has only been observed at low temperatures or at rather high coverages, close to the regime of ordered CuPc structures [KSS$^+$10]. The distance of the diffuse spots to the (0,0) spot were determined from the SPA-LEED images by extracting line scans, shown in Fig. 5.7 (c), through Fig. 5.7 (a). The distance of the broad spots (called R_3) to the (0,0) spot in k-space was determined to (0.85 ± 0.01) Å^{-1}. This corresponds to a distance of (7.4 ± 0.2) Å in real space. This value is almost identical to real space distance of the outer (third) ring of the diffraction pattern known from the relaxed monolayer of NTCDA with CuPc on top. This identical findings strengthen our assumption that this ring occurs due to intramolecular scattering on the CuPc molecules. Additionally, a diffuse ring was observed with a radius of $R_1 = (0.30 \pm 0.05)$ Å^{-1}, which corresponds in real space to a distance of $\mathrm{d}_1 = (20.9 \pm 0.2)$ Å. If this value is compared to the line scans performed at different submonolayer coverages of CuPc on Ag(111) [KSS$^+$10], one would estimate the coverage to (0.4 ± 0.1) ML in our stacked system. This fits rather well to the 0.5 ML determined by QMS (within the error bars). The second diffuse ring R_2, which was observed for the relaxed monolayer of NTCDA with CuPc on top, was also slightly visible. The ring radius is $R_2 = (0.57 \pm 0.01)$ Å^{-1}, which

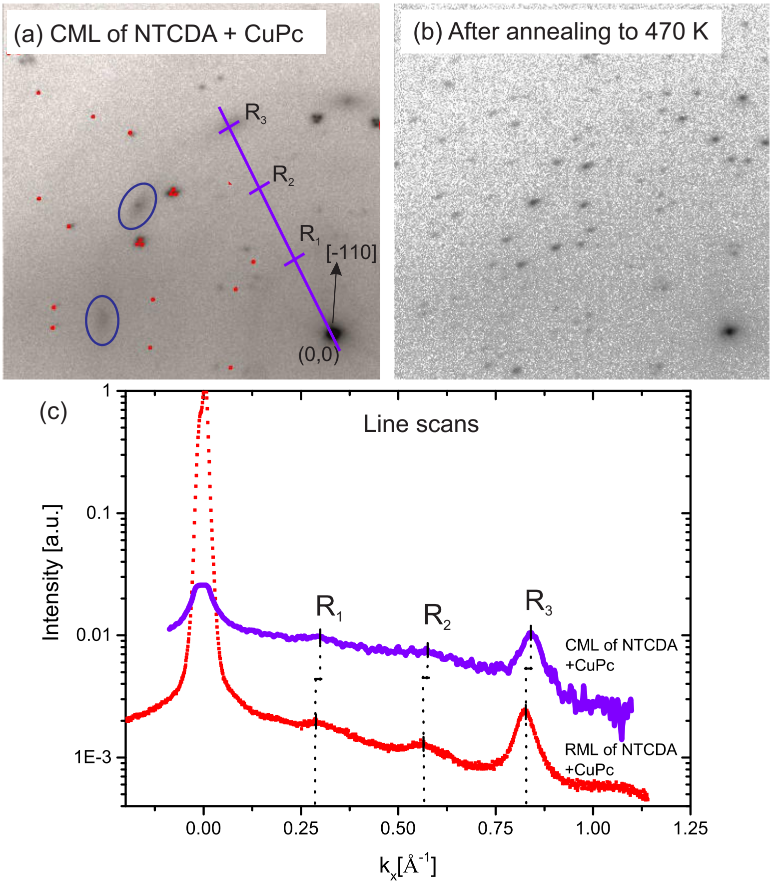

Figure 5.7.: (a) SPA-LEED image of the compressed monolayer (CML) of NTCDA with 0.5 ML CuPc on top on an Ag(111) substrate, measured at 27.2 eV. The red spots indicate the simulated diffraction pattern belonging to the CML of NTCDA. The broad spots, highlighted by blue circles, arise from the additional adsorbed submonolayer of CuPc. The purple line indicates the direction of the line scan shown in (c). (b) Diffraction pattern of the same sample after annealing to 470 K, which led to the formation of the NTCDA-rich phase. (c) Line scans from the SPA-LEED image of (a), the CML of NTCDA + CuPc, and from a diffraction pattern of the RML of NTCDA + CuPc.

corresponds in real space to a distance of d_3 = (11.0 ± 0.2) Å. This distance is within the error bars identical to the value determined for the RML of NTCDA + CuPc.

Desorption behaviour

This sample was annealed in steps of 20 K up to 470 K and after each annealing cycle a SPA-LEED image was recorded. The diffraction pattern of the stacked system (Fig. 5.7 (a)) disappeared only at 470 K and the pattern of the NTCDA-rich phase appeared as shown in Fig. 5.7 (b). Hence, the CuPc molecules do not penetrate into the first layer before 470 K are reached. Then molecular exchange occurs, NTCDA molecules desorb and the molecules form a laterally mixed film. This proofs that the CML of NTCDA is more stable than the RML of NTCDA. The 10 % increased packing density of the CML compared to the RML of NTCDA leads a higher potential barrier, which the molecules have to cross for exchanging NTCDA molecules from the first to the second layer. Thus thermal energy of the molecules at RT is sufficient for inducing a molecule exchange for the molecules in the RML of NTCDA + CuPc, but is too less for the molecules in the CML of NTCDA + CuPc.

5.3.2. Electronic properties

A. UV photoelectron spectroscopy

The electronic structure of this stacked system was measured by UPS and ARPES, to explain the well ordered alignment of the CuPc molecules on top of a compressed monolayer of NTCDA on Ag(111). The UV photoelectron spectrum is therefore shown in Fig. 5.8 by green circles. For comparison, the UV photoelectron spectroscopy spectrum of a homomolecular compressed monolayer of NTCDA on Ag(111) is displayed by black circles.

A new peak appears in the spectrum of the stacked system due to the adsorption of CuPc molecules. It corresponds to the HOMO of CuPc and is displayed in Fig. 5.8 in purple. It is located at a binding energy of E_B =1.38 eV. The HOMO peak of the homomolecular structure of CuPc is formed at a binding energy of E_B =1.25 eV [KSS$^+$10]. For a CuPc bilayer the second CuPc HOMO appears at a binding energy of 1.6 eV [Koc09]. Thus the HOMO of CuPc in the stacked system has a surprisingly low binding energy. The same effect was observed for the stacked system of a RML of NTCDA covered by CuPc on Ag(111). The HOMO peak of the CuPs located on top of a RML of NTCDA compressed by CuPc molecules had a binding energy of 1.07 eV. The same effect was also observed for the stacked system of PTCDA + CuPc [Sta13]. Stadtmüller explains this effect by a polarization of the PTCDA molecules, which induces a dipole moment in the CuPc molecules in the second layer. This overcompensates the effect of a work function increase due to the stronger binding of PTCDA to the substrate upon the adsorption of CuPc molecules. This leads a decreased work function of the stacked system.

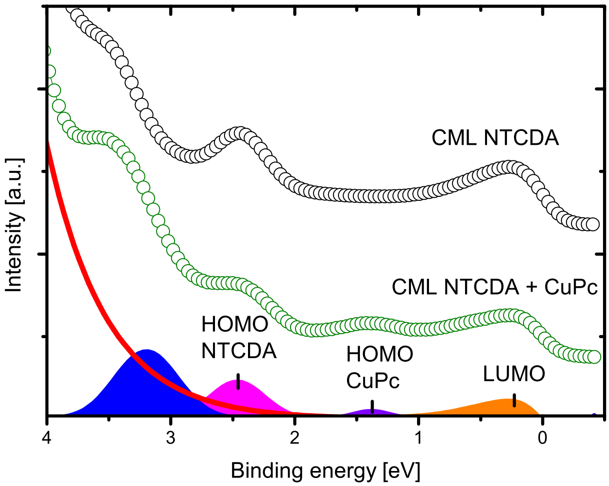

Figure 5.8.: UPS spectra of the compressed monolayer (CML) of NTCDA (black) and the stacked system with CuPc on top (green). The fitted peaks of the stacked system, the LUMO (orange), the HOMO of CuPc (purple) and the HOMO of NTCDA (magenta) are shown. The red line represents the background caused by inelastic scattered electrons.

The same effect appears probably for the stacked system of NTCDA and CuPc, as charge is transferred from the substrate to the NTCDA molecules due to adsorption on the Ag(111) surface. The larger interface dipole leads to a work function increase of around 0.2 eV [ABB06]. The work function change is smaller than for PTCDA on Ag(111), consequently this causes a different binding strength of the CuPc molecules in the second layer. Work function measurements could confirm this, but have not yet been performed.

The energy region close to the Fermi level was fitted by a Fermi function which cuts a Gaussian peak. The orange peak reflects the LUMO at a binding energy of $E_B = 0.13$ eV. It is expected that only the NTCDA molecules contribute to the partially filled LUMO peak as it is known for other stacked systems [SWS$^+$15]. Thus the LUMO of NTCDA is shifted to a 20 meV higher binding energy due to the adsorption of CuPc molecules on top of the compressed monolayer of NTCDA.

The HOMO of NTCDA is located at a binding energy of $E_B = 2.46$ eV and is displayed by a magenta coloured peak in Fig. 5.8. Thus the HOMO of NTCDA is shifted to a 40 meV higher binding energy due to the adsorption of CuPc molecules. The blue peak at a binding energy of $E_B = 3.2$ eV consists probably of a superposition of two peaks belonging to the HOMO-1 of NTCDA and CuPc.

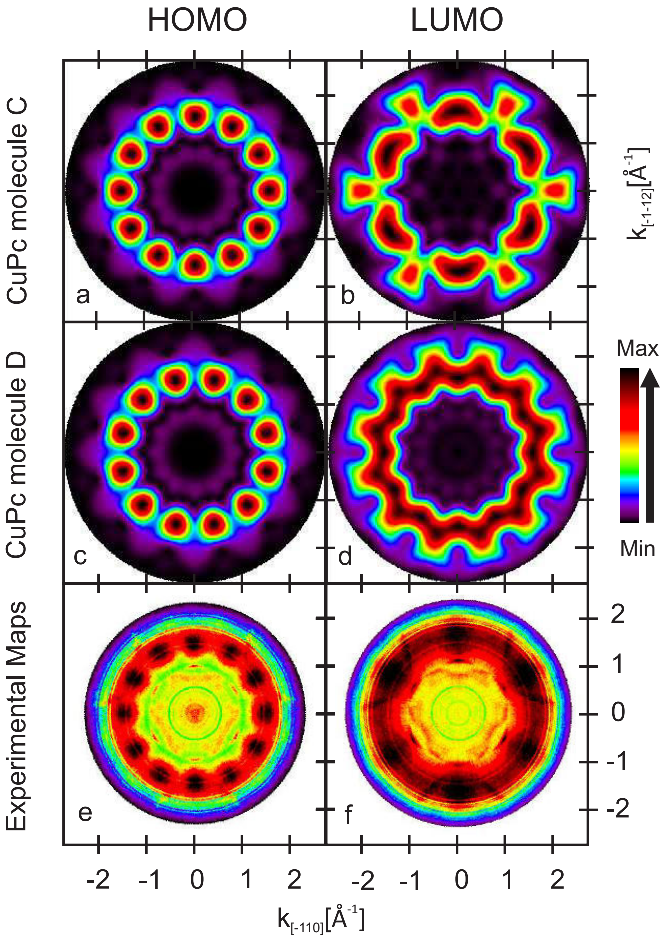

Figure 5.9.: Constant binding energy maps (CBE) for the HOMO and LUMO of a free molecule calculated by density functional theory under consideration of the p3m1 symmetry of the substrate. The CBE maps of the HOMO (a) and LUMO (b) for molecule C (0°) and the HOMO (c) and LUMO (d) for molecule D (80°) are shown. The measured maps of an CML of NTCDA with CuPc on top on Ag(111) in the energy regime of the HOMO (g) and LUMO (h).

B. ARPES and theoretical CBE maps

The SPA-LEED experiments presented earlier in this chapter, revealed an ordered CuPc layer on top of the CML of NTCDA, with a preferential orientation of the CuPc wings to the <-110> directions of the silver substrate. The comparison of calculated CBE maps, with different in-plane orientations to the silver substrate, to ARPES data recorded in the same energy regime should deliver the precise in-plane orientation of the CuPc molecules to the substrate. In Fig. 5.9 (a) the theoretical momentum map of the CuPc HOMO with its characteristic twelve emission features is shown, parallel aligned to the [-110] or equivalent substrate directions (called molecule C subsequently). According to its twelvefold symmetry, the momentum maps of all CuPc molecules with a rotation angle of $n * 30°$ ($n = 0 - 12$) to the <-110> direction, have the same intensity profile. The comparison with the experimental data cube in (e) shows a good agreement with the CBE map of molecule C. However, between the intensity maxima of the measured ARPES data cube there is some additional intensity visible. Therefore a second CBE map with a molecular rotation of 15° to the high symmetry direction of the substrate was considered (called molecule D), shown in Fig. 5.9(c).

The corresponding theoretical momentum maps of the LUMO for the different molecular orientations are also plotted in Fig. 5.9(b) for molecule C and for molecule D in (d). We expect that only the two NTCDA molecules contribute to the LUMO (not the CuPc LUMO) due to earlier experiments [SWS$^+$15]. However, for the deconvolution we used the theoretical maps of both NTCDA molecules (A and B) as well of both CuPcs (C and D) to confirm our assumption. The experimental momentum map of the former LUMO is shown in (f). The similarity of the latter with the CBE map of LUMO, measured for the homomolecular structure of the CML of NTCDA (see chapter 2), indicates that the NTCDA contribution is dominant for the peak at the Fermi level. The momentum map of the HOMO of NTCDA was measured as well, but is not displayed as it shows the same intensity distribution as the map of the pristine CML of NTCDA shown in chapter 3.

C. Orbital tomography deconvolution

All maps of the CuPc/CML NTCDA/Ag(111) were deconvoluted separately by orbital tomography. The resulting PDOS in the binding energy regime from -0.2 to 2.8 eV is displayed in Fig. 5.10. The maps of both NTCDA molecules, A (red) and B (blue), contribute to the binding energy region of the HOMO of NTCDA at 2.4 eV as it was observed for the homomolecular CML of NTCDA. Compared to the homomolecular CML of NTCDA both orbitals are shifted to larger binding energies of $E_B = 2.43$ eV (molecule A) and $E_B = 2.45$ eV (molecule B). These binding energies are only slightly lower than the values determined from the corresponding UPS spectrum ($E_B = 2.46$ eV).

The peak in the energy regime of the HOMO of CuPc contains contributions of molecule C and D, but as already assumed by the comparison of the theoretical maps with the measured momentum map, the map of molecule C (green) contributes approximately four times stronger than molecule D (pink). The orbital of molecule C has a binding energy of 1.39 eV and the orbital of molecule D of 1.34 eV. This confirms the SPA-LEED data, which indicate a preferential alignment of the CuPc molecules along the <-110> directions. In comparison, the HOMO of CuPc has a binding energy determined by UPS of 1.38 eV. It can be fitted by a single peak and the binding energy fits to the value determined by orbital tomography, as it is almost identical to the binding

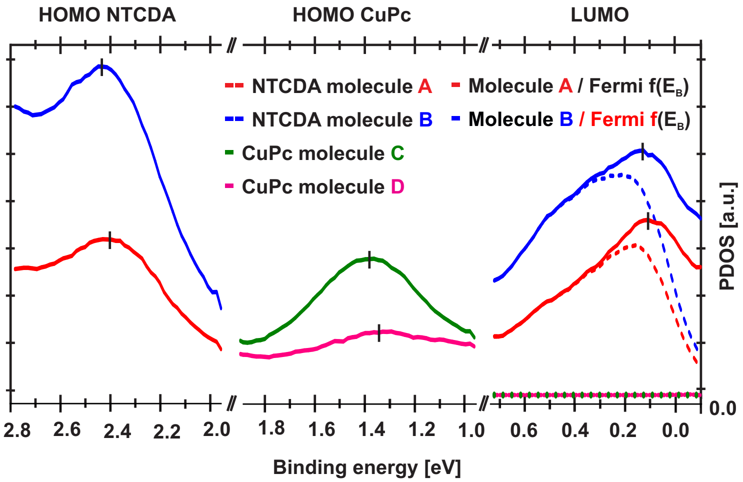

Figure 5.10.: The projected density of states (PDOS) of the HOMO of NTCDA and CuPc and the LUMO for both NTCDA molecules (A and B) as well as for CuPc (C and D) were obtained by the orbital tomography analysis of the ARPES data. The markers sign the position of the maxima of the LUMO and HOMO peaks. The LUMO is divided by the Fermi distribution function at $T_{eff} = 930\ K$.

energy of the HOMO of the more strongly contributing molecule C.

The energy regime at the Fermi level was also quantitatively analysed by orbital tomography. The ARPES data cube was deconvoluted by the four theoretical momentum maps of molecules A-D shown in Fig. 5.9, and that of the pure silver substrate. The resulting PDOS is displayed in the right part of Fig. 5.10. A magnified plot of the PDOS of the stacked system and the pristine CML of NTCDA is in this energy regime is shown in 5.11. The maps of both NTCDA orientations in the stacked layer (red and blue curve) show the same contribution to the LUMO as for the CML of NTCDA (orange and turquoise), and, as expected, the intensity contribution of the PDOS for both CuPc molecules is zero. Therefore it can be concluded that the LUMOs of CuPc are depleted and the complete intensity arises from the two inequivalent NTCDA molecules. This confirms that both organic layer does not interact with each other chemically, i.e. in terms of charge transfer.

Both NTCDA orbitals are shifted downwards by 20 meV to higher binding energies in comparison to the orbitals of the pure CML of NTCDA. The same values were determined by UPS. The shift can be interpreted as a strengthened interaction between the first organic layer with the underlying silver substrate induced by the additional adsorption of CuPc in the second layer. The shift is not significant as the instrumental resolution is around 30 meV, but the LUMOs of both PTCDA molecules in the herringbone structure of PTCDA on Ag(111) also shift to higher binding energies due to the

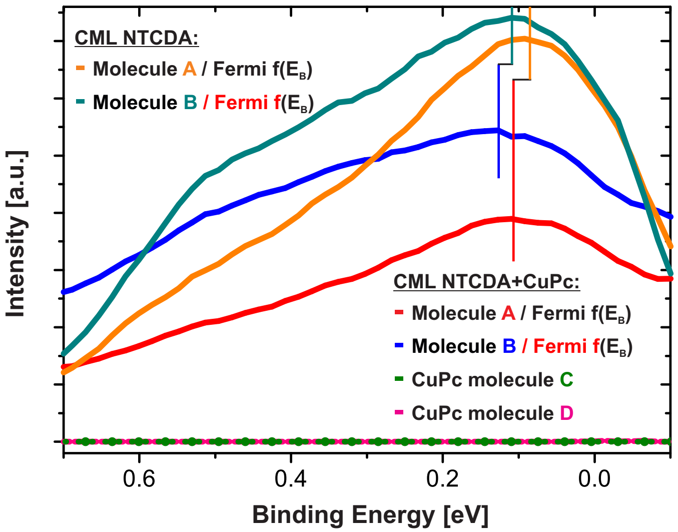

Figure 5.11.: A comparison of the projected density of states (PDOS) in the energy regime of the LUMO of the homomolecular CML of NTCDA and the CML of NTCDA with CuPc on top, obtained by the orbital tomography analysis of the ARPES data. The markers sign the position of the maxima of the LUMOs in both structures. The LUMOs are divided by the Fermi distribution function at $T_{eff} = 930\ K$.

adsorption of CuPc molecules on top. The shift depends on the CuPc coverage, but is in the range of 40 mV as reported for 0.5 ML of CuPc deposited on PTCDA [Sta13]. The smaller shift of the LUMOs of NTCDA seems to be therefore reasonable, as NTCDA is a weaker electron acceptor than PTCDA.

These results agree well with the geometric structure investigations. CuPc molecules grow on PTCDA on Ag(111) in a commensurate structure, but the diffraction pattern of the systems does not change until a complete monolayer of CuPc is deposited. Instead for a monolayer of NTCDA covered with CuPc molecules, broad spots appear already at 0.4 ML CuPc in the diffraction pattern. This indicates that the interaction between the CuPc and NTCDA molecules is stronger than for CuPc and PTCDA on Ag(111).

5.4. NTCDA on a ML of CuPc on Ag(111)

The inverse system of NTCDA on a monolayer of CuPc on Ag(111) has also been investigated by SPA-LEED. The SPA-LEED image of 0.98 ML CuPc on Ag(111) is shown in Fig. 5.12 (a). Afterwards 0.7 ML of NTCDA were deposited on top. The diffraction pattern of the CuPc ML disappeared and instead three diffuse rings arose, as shown in

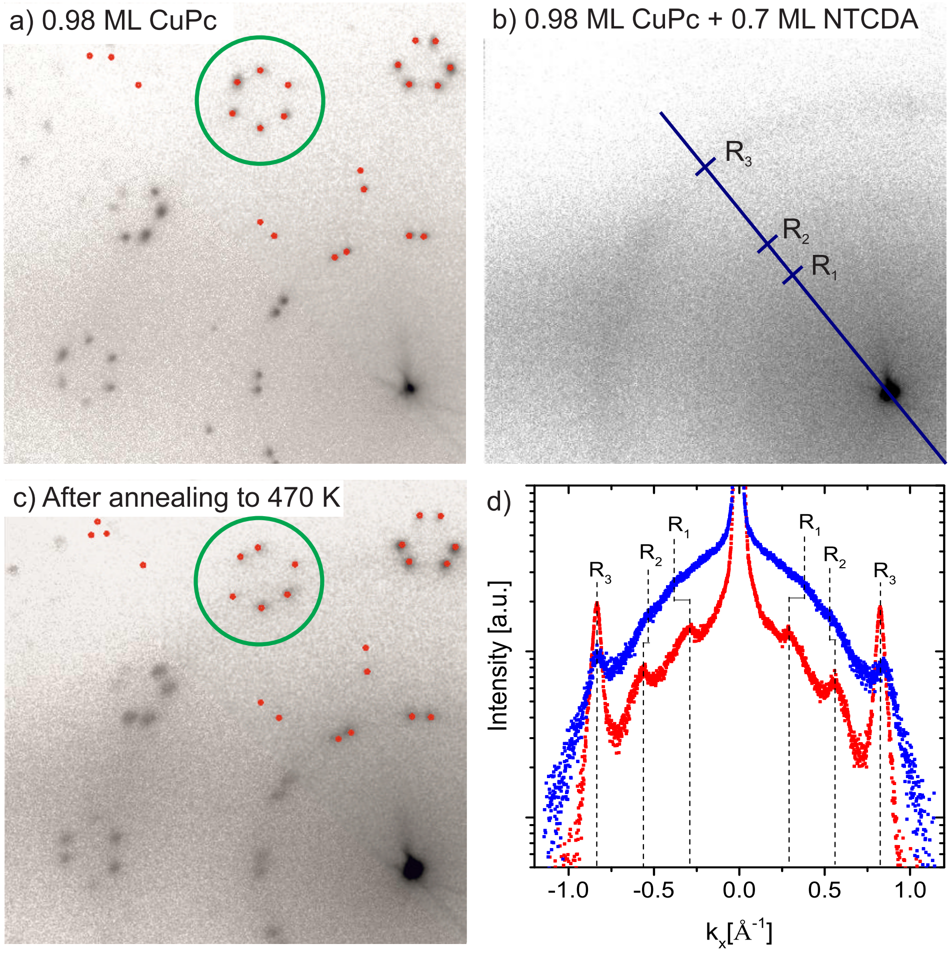
a) 0.98 ML CuPc

b) 0.98 ML CuPc + 0.7 ML NTCDA

c) After annealing to 470 K

Figure 5.12.: (a) SPA-LEED image of 0.98 ML CuPc on an Ag(111) substrate, measured at 27.2 eV. The red spots indicate the simulation of the diffraction pattern. (b) Same sample with additional 0.7 ML NTCDA on top. The blue line indicates the radial line scan direction. (c) The stacked system after annealing to 470 K. The SPA-LEED image shows the diffraction pattern of a closed monolayer of CuPc. (d) Radial line scan through the SPA-LEED image of NTCDA on a monolayer of CuPc on Ag(111) (blue) and CuPc on a relaxed monolayer of NTCDA on Ag(111) (red). The corresponding SPA-LEED images are shown in (b) and Fig. 5.1 (f)

Fig. 5.12 (b). This proofs that NTCDA does not stay on top of the CuPc monolayer, but exchanges with the CuPcs which leads to a diffuse LEED pattern. A radial line scan through the diffuse rings of the SPA-LEED image was recorded and is displayed in blue in Fig. 5.12 (d). The line scan through a SPA-LEED image of the RML of NTCDA with CuPc on top is plotted in red next to it for a better comparison of the systems.

For both systems three rings appear, but the positions in k-space differ slightly. The first ring, is in this system a disk with a radius of R_1 = (0.373 ± 0.005) Å^{-1}, which corresponds to a distance of d_1 = (16.8 ± 0.2) Å in real space. Under the assumption that ring 1 reflects the averaged intermolecular distance between the CuPc molecules which changes continuously with coverage (see [KSS$^+$10]), d_1 corresponds to a CuPc coverage of (0.6 ± 0.1) ML. The disk appears, as the molecules have not only one specific nearest neighbour distance, but have many different distances equal or larger than the determined 16.8 Å.

The third ring R_3 has a radius of (0.840 ± 0.005) Å^{-1}, which reflects a distance d_3 = (7.5 ± 0.2) Å. This value is identical to ring radius of the SPA-LEED image of the RML and CML of NTCDA with CuPc on top. This is clearly visible in Fig. 5.12 (d). It also arises due to intramolecular scattering. The intensity of this ring is only slightly modulated in this stacked system, compared to the inverse systems. A reason could be that CuPc molecules are located in both organic layers and they are probably only preferential aligned in one of the layers. Thus azimuthal randomly aligned molecules contribute to the scattering intensity, which reduces the modulation of the ring.

The intermediate ring is located at R_2 =(0.552 ± 0.005) Å^{-1}. In real space the distance corresponds to d_2 = (11.4 ± 0.2) Å. We believe that this ring represents a prominent intermolecular distance between NTCDA molecules, for the following reasons: A conformation for this assumption is, that the NTCDA molecules are set in a distance of 11.57 Åin the [-110] direction of the relaxed monolayer of NTCDA. This distance is slightly larger as the value determined from the stacked systems, but the NTCDA molecules have in the slightly denser packed so called α_2-phase a distance of 11.07 Å to each other [KSK$^+$08]. Thus it seems to be reasonable that the molecules arrange similarly as in these structures. Additional this intermediate ring appeared for all investigated systems, except the cooled RML of NTCDA with CuPc on top. The ring is rather intense for systems of the RML of NTCDA + CuPc and a ML of CuPc + NTCDA on Ag(111). In both structures NTCDAs are located in the second organic layer. Therefore it is reasonable that they have certain distance to each other, which causes the intermediate ring.

Desorption behaviour

The stacked system of NTCDA on CuPc on Ag(111) was also annealed, to determine whether the molecules form a well ordered mixed structure or NTCDA desorbs from the CuPc layer due to annealing. In Fig. 5.12 (c) a SPA-LEED image of the sample after annealing to 470 K is displayed. The diffuse rings are gone and instead the diffraction pattern of a monolayer of CuPc reappeared. This indicates that the NTCDA molecules desorb upon annealing and CuPc molecules diffuse back to the first layer where they rearranged in a well ordered structure of a CuPc monolayer.

However the diffraction spots are slightly differently arranged in Fig. 5.12 (c) compared to Fig. 5.12 (a), as highlighted by the green circles in both images. This indicates different densely packed CuPc molecules before and after annealing. The diffraction pattern after annealing (c) reflects a higher coverage, namely a complete monolayer of CuPc while the coverage in (a), was only 0.98 ML. Since no additional CuPc molecules were deposited, the more densely packed structure must be caused by NTCDA molecules in the first layer, which occupy some space on the surface. The neighbouring CuPc molecules in the second layer can not hinder the NTCDA molecules to desorb, but the embedding of the NTCDAs between CuPcs in the first organic layer, lead to a stronger bonding of the NTCDA molecules, which enables them to stay during annealing on the sample.

5.5. Comparison of different stacked systems

The results obtained for the different stacked systems consisting of NTCDA and CuPc are summarized in table 5.1 and the findings will be discussed in this section. In addition, these results are discussed in context with the stacked systems consisting of PTCDA and CuPc.

As we have reported in this chapter, neither NTCDA stays on top of monolayer of CuPc nor CuPc remains exclusively on top of a relaxed monolayer of NTCDA. Molecular exchange occurs often between the two organic layers, which indicates that - in general - laterally mixed systems are energetically more stable than stacked systems. In the case of NTCDA on a monolayer of CuPc it seems to be reasonable that the NTCDA molecules penetrate into the CuPc layer, as the repulsive interaction between the CuPc molecules and their high mobility leads to a low stability of the CuPc monolayer [KSS$^+$10], [Sta13]. The not completely densely packed relaxed monolayer of NTCDA allows for the CuPc molecules to penetrate into the first layer as well. We believe the driving force for the exchange is twofold: Firstly the repulsive interaction between the CuPc molecules is reduced, as less CuPc contacts are available, and secondly, the attractive interaction between the NTCDA and CuPc molecules, as it is known from the laterally mixed structures of chapter 4 is rather high. Both effects result in an energy gain of the total potential.

Deposition on the cooled sample the stacked system of CuPc on the relaxed monolayer of NTCDA hinders the CuPc molecules to diffuse into the RML of NTCDA. This experiment has proved that the molecules have to overcome a potential barrier for the exchange, which is possible at room temperature, but the reduced thermal energy of the molecules at 100 K prohibits them to cross this barrier.

For CuPc on a compressed monolayer of NTCDA no exchange of the molecules was found obviously due to the denser packing of this NTCDA layer. The higher density of NTCDA molecules on the substrate in the compressed monolayer leads to an energy gain, although the molecules have to leave their optimum commensurate adsorption sites, which they exhibit in the RML of NTCDA. This causes a higher energy barrier for molecular exchange compared to the RML + CuPc system. The CuPc molecules can not cross the potential barrier at RT and consequently stay on top of the CML of NTCDA.

Real space distance	RML NTCDA + CuPc [Å]	RML NTCDA LT + CuPc [Å]	CML NTCDA + CuPc [Å]	ML CuPc + NTCDA [Å]
Ring 1	22.0	13.5	20.9	16.8
Ring 2	11.2	-	11.0	11.4
Ring 3	7.5	-	7.4	7.5

Table 5.1.: The real space distances determined from the ring radii observed in the SPA-LEED images of all stacked systems of NTCDA and CuPc on Ag(111).

The sample has to be annealed to 470 K until the CuPc molecules have sufficient energy to cross the potential barrier, which subsequently leads to an exchange of CuPcs from the second layer with NTCDA molecules of the CML first layer. The molecules then arrange in a mixed NTCDA-rich phase. 470 K is an astonishingly high temperature, as NTCDA molecules desorb already from the homomolecular CML at 390 K.

The behaviour of stacked systems consisting of PTCDA and CuPc is different. The CuPc molecules stay on top of a closed monolayer of PTCDA on Ag(111) at room temperature and form a commensurate relation between the organic layers [SHK$^+$09].

In a homomolecular monolayer of PTCDA it is not possible to desorb PTCDA from the surface. If the system CuPc/PTCDA/Ag(111) is annealed, CuPc molecules desorb first and PTCDA stays on the sample. Only at a temperature of 575 K some PTCDA molecules desorb and form a laterally mixed structure with the remaining CuPc molecules. Therefore the adsorption of CuPc in the second layer changes the PTCDA-metal interface which allows for a desorption of PTCDA by annealing. The CuPc molecules act as a catalyst as the potential barrier to desorb PTCDA is split in two steps with smaller energy barriers: Firstly the molecular exchange and secondly the desorption from the second layer.

The behaviour is changed for the inverse system where PTCDA is adsorbed on a closed monolayer of CuPc. The PTCDA molecules diffuse into the first layer, exchange with the CuPc molecules and form islands with different rotational domains on the metal surface. This effect is even proven by XSW experiments [Sta13]. Unfortunately, both stacked systems of a CuPc monolayer with either PTCDA or NTCDA on top, were not investigated with LT - deposition of te second molecule. It would be very interesting to investigate whether the CuPc monolayer stays intact or whether the molecules would still exchange.

For the stacked heteromolecular bilayer system of a ML of CuPc on top of a closed monolayer of PTCDA on the Ag(111), a commensurate registry between the two molecular layers and the substrate has been found by Stadtmüller et al. [SSK$^+$12]. In this case the CuPc molecules are rotated 45° to the [-110] direction of the Ag(111) substrate. For submonolayer coverages of CuPc on top of a monolayer of PTCDA, the LEED pattern consists however of a superposition of PTCDA spots and a diffuse ring arising from CuPc. This indicates that the molecules have a random azimuthal alignment in relation to the PTCDA molecules on the silver substrate, as it is known for the homomolecular CuPc structures. This is different for stacked systems of CuPc on either the RML or the CML of NTCDA. The LEED pattern for both systems covered with 0.2-0.5 ML of CuPc, shows broad spots which are arranged on a ring instead of a diffuse ring. Their position in k-space indicates that all CuPc molecules are aligned azimuthally along the <-110> directions of the Ag(111) surface. This result was confirmed by ARPES and orbital tomography.It can be speculated whether CuPc grows with a commensurate registry to the substrate at higher coverages, e.i., when the complete monolayer coverage is reached. At lower coverages investigated here, an azimuthal alignment of CuPcs was only observed for CuPc submonolayers on Ag(111) cooled down to 140 K.

6. Summary

In this work a comprehensive systematic study of different laterally and vertically mixed heteromolecular structures of NTCDA and CuPc adsorbed on Ag(111) was performed. The lateral and electronic properties of the relaxed and compressed monolayer of NTCDA on Ag(111) was initially determined, as this information acted as a basis knowledge for the study of the heteromolecular systems.

The lateral order of the relaxed monolayer (RML) of NTCDA on Ag(111) was studied earlier by SPA-LEED and STM by [KSK$^+$08] and [Fou14]. The molecules form a commensurate unit cell containing two NTCDA molecules, aligned with their long axes in rows parallel to the [-110] direction of the silver substrate in a so-called brick wall structure. The lateral arrangement of the molecules in the 10% more densely packed compressed monolayer (CML) of NTCDA was determined by new room temperature STM measurements in more detail than Stahl et al. [SGS$^+$98]. Two molecules are contained in an incommensurate smaller unit cell, but in a herringbone structure, where they include an angle of 80°. This herringbone-like arrangement is very similar to the homomolecular structure of PTCDA on Ag(111), which seems to occur due to the formation of hydrogen bonds between the oxygen and hydrogen atoms of PTCDA causing an attractive interaction between the molecules. Therefore, when forms the CML of NTCDA, the energy gain from adsorbing additional NTCDA molecules on the surface has to be larger than the energy loss which is caused by leaving the commensurate adsorption sites of the RML of NTCDA. By angle-resolved UPS the electronic properties of both structures were investigated. The resonances determined for the RML of NTCDA could be directly assigned to the LUMO and HOMO. Knowledge about the molecular in-plane orientation in relation to the substrate of the CML of NTCDA allowed to determine the binding energies of the LUMOs of both inequivalent NTCDAs by orbital tomography, which are separated by 20 meV. This indicated a weaker electrostatic potential difference between the both NTCDAs compared to PTCDA, where the LUMOs are split by 170 meV.

The main focus of the work was to investigate laterally mixed structures with different coverage ratios of NTCDA to CuPc on Ag(111), and compare those with heterostructures of PTCDA and CuPc, which were studied earlier by Stadtmüller [Sta13].

Firstly, the lateral structure of the mixed NTCDA-CuPc phases had to be characterized in order to study how the size and shape of the unit cell, caused by different molecular ratios of NTCDA and CuPc, influences the vertical and electronic structure. Five coverage dependent structures were found by SPA-LEED and STM: a NTCDA-rich phase, two different coexisting intermediate (IM1 and IM2) phases with an identical number of molecules and a CuPc-rich phase. An additional intermediate phase appears upon annealing with the same number of molecules as in the non-annealed IM phases. All phases have a surprisingly large unit cell size, which is up to three times larger than for the CuPc-PTCDA heterostructures. Furthermore, in all structures the molecules have a (uni-axial) commensurate registry with the substrate. The in-plane orientation and arrangement of the molecules to each other was determined by STM and indicated that the molecules arrange themselves in such a way that they can form hydrogen bonds between the oxygen and hydrogen atoms of NTCDA and the hydrogen atoms of CuPc, which are assumed to cause the attractive molecular interaction. It seems likely that the small size of the NTCDA molecules is partially responsible for the large unit cells. Only in these arrangements the molecules can at the same time form attractive hydrogen bonds and only few repulsive CuPc-CuPc contacts, while additionally keeping their commensurate adsorption sites. This indicates that the competition between strong molecule-substrate and attractive molecule-molecule interactions leads to the formation of these large unit cells.

The adsorption heights of NTCDA and CuPc were studied by NIXSW for the NTCDA- and CuPc-rich phases at RT and LT. From literature it is known that NTCDA has a lower adsorption height than CuPc in their homomolecular structures. An adsorption height alignment was observed upon mixing for both phases, but at different adsorption heights. NTCDA (CuPc) increases (lowers) its adsorption height in the CuPc-rich phase in comparison to the homomolecular structures. In contrast both molecules lowered their adsorption heights in the NTCDA-rich phase. Upon cooling the lateral order of the structures remained unchanged and the adsorption height alignment of NTCDA and CuPc was still valid, but the adsorption heights of both molecules were reduced by 0.1 Å.

ARPES measurement and consequently orbital tomography revealed for both mixed phases that only the LUMO of NTCDA is (partially) filled, but depopulated for the CuPcs. In addition the LUMO of NTCDA is shifted to higher binding energies compared to its homomolecular structure. This was additionally confirmed by STS measurements on the NTCDA-rich phase at LT. STM images revealed further electronic contrasts of differing strengths for the eight NTCDA molecules. Four NTCDAs have a much brighter contrast than the other four NTCDAs. A possible explanation for the low adsorption heights in the NTCDA-rich phase is therefore that the brighter molecules are located at higher adsorption heights than the other NTCDAs. This can not be distinguished by XSW as the average adsorption height can only determined. By UPS measurements could be obtained that the LUMO of NTCDA is shifted to higher binding energies in the mixed phases upon cooling. This confirms that the lower adsorption heights at low temperatures go along with a stronger binding of the NTCDA molecules to the substrate.

The findings for the NTCDA-CuPc heterostructures fit therefore to the model of charge reorganization for mixed PTCDA-CuPc structures established by Stadtmüller et al., where the electrons are transferred form the donor CuPc via the substrate to the acceptor PTCDA. Additionally, the measurements proved that NTCDA is able to take up the whole charge donated by the CuPc molecules, although it is a weaker charge acceptor compared to PTCDA.

As a second class of systems vertically stacked molecular bilayers of NTCDA and CuPc were studied on Ag(111). CuPc molecules on top of a closed monolayer of NTCDA on Ag(111) were investigated, both on a relaxed monolayer of NTCDA and on a compressed monolayer of NTCDA. In addition the inverse system, NTCDA on a monolayer of CuPc, was studied. Molecular exchange was found for CuPc on the RML of NTCDA and for NTCDA on a ML of CuPc. No molecular exchange was found for CuPc on a CML of NTCDA. The higher packing density of the NTCDAs in the CML hinders the CuPc molecules to diffuse into the first layer, but is possible for the RML where the CuPcs have sufficient space in the first layer to adsorb without a replacement of NTCDA molecules due to the more loosely packing density. This causes a higher energy barrier for molecular exchange on the CML, which the CuPc molecules can not cross at RT. Annealing to 470 K is necessary for the molecules to overcome the potential barrier, which consequently leads to molecular exchange.

Furthermore SPA-LEED measurements revealed that the CuPc molecules arrange in a long range ordered film on top of the compressed NTCDA monolayer. This was not observed for CuPc coverages on pristine Ag(111) below 0.9 ML of CuPc at RT. Fitting of ARPES data by orbital tomography revealed that the CuPcs in the second layer have a prominent azimuthal alignment to the [-110] substrate direction. In addition, the comparison of the PDOS obtained by orbital tomography for the homomolecular CML of NTCDA and the stacked system with CuPc on top demonstrated that the CuPc molecules in the second layer induce a stronger bonding between the NTCDA molecules in the first layer and the surface, as the LUMOs of both NTCDA molecules are shifted to 20 meV higher binding energies in the stacked system. This shift is not significant as for PTCDA in a bilayer system of CuPc on PTCDA on Ag(111). A smaller shift seems however to be reasonable for the weaker electron acceptor NTCDA.

Exchanging PTCDA for the weaker electron acceptor NTCDA facilitates a deeper understanding of the charge reorganization in heteromolecular systems and demonstrates one way for modifying the electronic properties of acceptor-donor contacts at metal substrates. The next step for a systematic study of heteromolecular structures would be to exchange CuPc with a stronger charge donor i.e. SnPc and study the properties of PTCDA-SnPc systems. Gerben van Straaten has already started with these investigations in his Ph.D. project. The second version for the modification of the interaction between the molecules and the substrate would be to use, i.e., an Ag(110) or a Cu(111) crystal leading to a stronger molecule-substrate interaction. Deposition of the same molecules on these substrates could be of interest as it reveals whether the geometric shape of the small NTCDA molecules lead to the formation of large unit cells upon mixing with CuPc or the stronger interaction to the substrate induce the formation of smaller or even less ordered superstructures.

List of Figures

List of Tables

Bibliography

[ABB06] A. Alkauskas, A. Baratoff, and C. Bruder. Site-selective adsorption of naphthalene-tetracarboxylic-dianhydride on Ag (110): First-principles calculations. *Phys. Rev. B*, 73:1–8, 2006.

[Alm06] C. O. Almbladh. Photoemission Beyond the Sudden Approximation. *Journal of Physics*, 35:127–144, 2006.

[Bar61] J. Bardeen. Tunnelling from a many-particle point of view. *Physical Review Letters*, 6(2):57–59, 1961.

[Bay08] P. Bayersdorfer. *SPA-LEED Studie zur Adsorption von metallfreien Phthalocyaninen auf Ag(111) im Bereich kleiner Bedeckungen.* Diploma thesis, Julius-Maimilian-Universität Würzburg, 2008.

[BC64] B. W. Batterman and H. Cole. Dynamical Diffraction of X Rays by Perfect Crystals. *Review of Modern Physics*, 36(3):681–717, 1964.

[BCK05] J. V. Barth, Gi. Costantini, and K. Kern. Engineering atomic and molecular nanostructures at surfaces. *Nature*, 437:671–679, 2005.

[BFS$^+$07] A. Bendounan, F. Forster, A. Schöll, D. Batchelor, J. Ziroff, E. Umbach, and Friedrich Reinert. Electronic structure of 1ML NTCDA/Ag(111) studied by photoemission spectroscopy. *Surface Science*, 601:4013–4017, 2007.

[BLC$^+$10] J. D. Baran, J. A. Larsson, A. A. Cafolla, K. Schulte, and V. R. Dhanak. Theoretical and experimental comparison of SnPc, PbPc, and CoPc adsorption on Ag(111). *Physical Review B*, 81(7), 2010.

[BMW$^+$12] O. Bauer, G. Mercurio, M. Willenbockel, W. Reckien, C. Heinrich Schmitz, B. Fiedler, S. Soubatch, T. Bredow, F. S. Tautz, and M. Sokolowski. Role of functional groups in surface bonding of planar π-conjugated molecules. *Physical Review B*, 86(23):235431 1–11, 2012.

[BRdAHK04] M. Blanco-Rey, P. de Andres, G. Held, and D. A. King. A FORTRAN-90 Low-Energy Electron Diffraction program (LEED90 v1.1). *Computer Physics Communications*, 161:151–165, 2004.

[BRGW82a] G. Binnig, H. Rohrer, Ch. Gerber, and E. Weibel. Surface Studies by Scanning Tunneling Microscopy. *American Physical Society*, 49(1):57–61, 1982.

[BRGW82b] G. Binnig, H. Rohrer, Ch Gerber, and E. Weibel. Tunneling through a controllable vacuum gap. *Applied Physics Letters*, 40(1982):178–180, 1982.

[BWBM03] C. Bobisch, Th. Wagner, A. Bannani, and R. Moeller. Ordered binary monolayer composed of two organic molecules: Copper-phthalocyanine and 3,4,9,10-perylene-tetra-carboxylic-dianhydride on Cu(111). *The Journal of Chemical Physics*, 119(18):9804, 2003.

[CSS+12] M. C. Cottin, J. Schaffert, A. Sonntag, H. Karacuban, R. Möller, and C. A. Bobisch. Supramolecular architecture of organic molecules: PTCDA and CuPc on a Cu(111) substrate. *Applied Surface Science*, 258(6):2196–2200, 2012.

[DGS+07] S. Duhm, A. Gerlach, I. Salzmann, B. Broker, R. Johnson, F. Schreiber, and N. Koch. PTCDA on Au(111), Ag(111) and Cu(111): Correlation of interface charge transfer to bonding distance. *Organic Electronics*, 9:111–118, 2007.

[EBST04] M. Eremtchenko, D. Bauer, J.A. Schaefer, and F.S. Tautz. Structure, bonding, and growth at a metal-organic interface in the weak chemisorption regime: Perylene-Ag(111). *Journal of Materials Research*, 19(7):2028–2039, 2004.

[ECS+07] F. Evangelista, V. Carravetta, G. Stefani, B. Jansik, M. Alagia, S. Stranges, and A. Ruocco. Electronic structure of copper phthalocyanine: an experimental and theoretical study of occupied and unoccupied levels. *The Journal of Chemical Physics*, 126(12):124709 1–11, 2007.

[Ein05] A. Einstein. Über einen die Erzeugung von Verwendung des Licht betreffenden heuristischen Gesichtspunkt. *Ann. Physik*, 332:132–148, 1905.

[ESBG+13] A. El-Sayed, P. Borghetti, E. Goiri, C. Rogero, L. Floreano, G. Lovat, Duncan John Mowbray, Jose Luis Cabellos, Yutaka Wakayama, Angel Rubio, Jose Enrique Ortega, and Dimas G de Oteyza. Understanding energy-level alignment in donor-acceptor/metal interfaces from core-level shifts. *ACS nano*, 7(8):6914–20, 2013.

[Fin99] R. Fink. Substrate-dependent lateral order in naphthalene-tetracarboxylic-dianhydride monolayers. *Physical Review B*, 402(4):20–2826, 1999.

[For97] S. Forrest. Ultrathin Organic Films Grown by Organic Molecular Beam Deposition and Related Techniques. *Chemical Reviews*, 97(6):1793–1896, 1997.

[Fou14] N. Fournier. *STM-based quantum transport through molecular wires.* Ph.d . thesis, RWTH Aachen, 2014.

[GMES$^+$14] E. Goiri, M. Matena, A. El-Sayed, J. Lobo-Checa, P. Borghetti, C. Rogero, B. Detlefs, J. Duvernay, J. E. Ortega, and D. G. De Oteyza. Self-assembly of bicomponent molecular monolayers: Adsorption height changes and their consequences. *Physical Review Letters*, 112:1–5, 2014.

[GSS$^+$05] A. Gerlach, F. Schreiber, S. Sellner, H. Dosch, I. Vartanyants, B. Cowie, T.-L. Lee, and J. Zegenhagen. Adsorption-induced distortion of F16CuPc on Cu(111) and Ag(111): An x-ray standing wave study. *Physical Review B*, 71(20), May 2005.

[HÖ3] S. Hüfner. *Photoelectron Spectroscopy - Principles ans Applications.* Springer Verlag Berlin Heidelberg, 3 edition, 2003.

[Hal88] W. Hallwachs. Über den Einfluss des Lichtes auf electrostatisch geladenen Körper. *Ann. Physik*, 269:269–301, 1888.

[HBL$^+$07] S. K. M. Henze, O. Bauer, T.-L. Lee, M. Sokolowski, and F.S. Tautz. Vertical bonding distances of PTCDA on Au(111) and Ag(111): Relation to the bonding type. *Surface Science*, 601(6):1566–1573, 2007.

[HCL$^+$10] Y. L. Huang, W. Chen, H. Li, M. Jing, J. Pflaum, and A. T. S. Wee. Tunable two-dimensional binary molecular networks. *Small*, 6(1):70–75, 2010.

[Hen82] M. Henzler. Leed studies of surface imperfections. *Applications of Surface Science*, 12:450–469, 1982.

[Her87] H. Hertz. Über den Einfluss des ultravioletten Lichtes auf die elektrische Entladung. *Ann. Physik*, 267:983–1000, 1887.

[HGS$^+$10] M. Häming, M. Greif, C. Sauer, A. Schöll, and F. Reinert. Electronic structure of ultrathin heteromolecular organic-metal interfaces: SnPc/PTCDA/Ag(111) and SnPc/Ag(111). *Physical Review B*, 82(23):1–10, 2010.

[HKC$^+$05] A. Hauschild, K. Karki, B. Cowie, M. Rohlfing, F. Tautz, and M. Sokolowski. Molecular Distortions and Chemical Bonding of a Large π-Conjugated Molecule on a Metal Surface. *Physical Review Letters*, 94(3):036106, 2005.

[HTS$^+$10] A. Hauschild, R. Temirov, S. Soubatch, O. Bauer, A. Schöll, B. C. C. Cowie, T.-L. Lee, F. S. Tautz, and M. Sokolowski. Normal-incidence x-ray standing-wave determination of the adsorption geometry of PTCDA on Ag(111): Comparison of the ordered room-temperature and disordered low-temperature phases. *Physical Review B*, 81(12):125432, 2010.

[HvH99] M. Horn-von Högen. Growth of semiconductor layers studied by spot profile analysing low energy electron diffraction. *Zeitschrift für Kristallographie*, 721:591–629, 1999.

[HWCW11] H. Huang, S. L. Wong, W. Chen, and A.T. S. Wee. LT-STM studies on substrate-dependent self-assembly of small organic molecules. *Journal of Physics D: Applied Physics*, 44:464005, 2011.

[KHT$^+$08] L. Kilian, A. Hauschild, R. Temirov, S. Soubatch, A. Schöll, A. Bendounan, F. Reinert, T.-L. Lee, F. Tautz, M. Sokolowski, and E. Umbach. Role of Intermolecular Interactions on the Electronic and Geometric Structure of a Large π-Conjugated Molecule Adsorbed on a Metal Surface. *Physical Review Letters*, 100(13):1–4, 2008.

[Kie07] T. Kietzke. Recent advances in organic solar cells. *Advances in OptoElectronics*, 2007.

[Kle13] C. Kleimann. *Adsorption of (hetero-) organic Phthalocyanine and PTCDA thin films on Ag(111).* Ph.d. theis, RWTH Aachen, 2013.

[Koc09] M. Kochler. *Hochauflösende Photoelektronenspektroskopie an dünnen CuPc-Filmen auf Edelmetall (111) -Oberflächen.* Diploma thesis, Julius-Maximiian-Universität Würzburg, 2009.

[KSK$^+$08] L. Kilian, U. Stahl, I. Kossev, M. Sokolowski, R. Fink, and E. Umbach. The commensurate-to-incommensurate phase transition of an organic monolayer: A high resolution LEED analysis of the superstructures of NTCDA on Ag(111). *Surface Science*, 602(14):2427–2434, 2008.

[KSK$^+$11] I. Kröger, B. Stadtmüller, C. Kleimann, P. Rajput, and C. Kumpf. Normal-incidence x-ray standing-wave study of copper phthalocyanine submonolayers on Cu(111) and Au(111). *Physical Review B*, 83(19):1–9, 2011.

[KSS$^+$10] I. Kröger, B. Stadtmüller, C. Stadler, J. Ziroff, M. Kochler, A. Stahl, F. Pollinger, T.-L. Lee, J. Zegenhagen, F. Reinert, and C. Kumpf. Submonolayer growth of copper-phthalocyanine on Ag(111). *New Journal of Physics*, 12, 2010.

[KTA03] H. Koezuka, A. Tsumura, and T. Ando. Field-effect transistor with polythiophene thin films. *Synthtic Metals*, 18(1-3):699–704, 2003.

[KTH$^+$06] A. Kraft, R. Temirov, S. Henze, S. Soubatch, M. Rohlfing, and F. Tautz. Lateral adsorption geometry and site-specific electronic structure of a large organic chemisorbate on a metal surface. *Physical Review B*, 74(4):041402, 2006.

[KUS04] L. Kilian, E. Umbach, and M. Sokolowski. Molecular beam epitaxy of organic films investigated by high resolution low energy electron diffraction (SPA-LEED): 3,4,9,10-perylenetetracarboxylicacid-dianhydride (PTCDA) on Ag(111). *Surface Science*, 573(3):359–378, 2004.

[KUS06] L. Kilian, E. Umbach, and M. Sokolowski. A refined structural analysis of the PTCDA monolayer on the reconstructed Au(111) surface-Rigid or distorted carpet? *Surface Science*, 600(13):2633–2643, 2006.

[KWW$^+$11] G. Kichin, C. Weiss, C. Wagner, F. S. Tautz, and R. Temirov. Single molecule and single atom sensors for atomic resolution imaging of chemically complex surfaces. *Journal of the American Chemical Society*, 133(42):16847–16851, 2011.

[LH02] M. Lackinger and M. Hietschold. Determining adsorption geometry of individual tin - phthalocyanine molecules on Ag (111) - a STM study at submonolayer coverage. *Surface Science*, 520, 2002.

[Mer12] G. Mercurio. *Study of Molecule-Metal Interfaces by Means of the Normal Incidence X-ray Standing Wave Technique.* Ph.d. thesis, RWTH Aachen, 2012.

[MTSH$^+$01] S. Mannsfeld, M. Toerker, T. Schmitz-Hübsch, F. Sellam, T. Fritz, and K. Leo. Combined LEED and STM study of PTCDA growth on reconstructed Au(111) and Au(100) single crystals. *Organic Electronics*, 2(3-4):121–134, December 2001.

[NRGR$^+$06] N. Nicoara, E. Román, J. M. Gómez-Rodríguez, J. A. Martín-Gago, and J. Méndez. Scanning tunneling and photoemission spectroscopies at the PTCDA/Au(111) interface. *Organic Electronics*, 7(5):287–294, 2006.

[Ohn94] M. Ohno. Theoretical Studies of Core Ionization, Excitation and Deexcitation of Adsorbates. *Molecular Engineering*, 4:61–86, 1994.

[PKDR13] P. Puschnig, G. Koller, C. Draxl, and M. G. Ramsey. *Small Organic Molecules on Surfaces - Fundamentals and Applications.* Springer Verlag, 2013.

[PRU$^+$11] P. Puschnig, E.-M. Reinisch, T. Ules, G. Koller, S. Soubatch, M. Ostler, L. Romaner, F. Tautz, C. Ambrosch-Draxl, and M. Ramsey. Orbital tomography: Deconvoluting photoemission spectra of organic molecules. *Physical Review B*, 84(23):1–8, 2011.

[RTT07] M. Rohlfing, R. Temirov, and F. S. Tautz. Adsorption structure and scanning tunneling data of a prototype organic-inorganic interface: PTCDA on Ag(111). *Physical Review B*, 76(11):115421, 2007.

[SGP$^+$14] B. Stadtmüller, M. Gruenewald, J. Peuker, R. Forker, T. Fritz, and C. Kumpf. Molecular Exchange in a Heteromolecular PTCDA/CuPc Bilayer Film on Ag(111). *The Journal Phys Chemistry C*, 118:28592–28602, 2014.

[SGS$^+$98] U. Stahl, D. Gador, A. Soukopp, R. Fink, and E. Umbach. Coverage-dependent superstructures in chemisorbed NTCDA monolayers: a combined LEED and STM study. *Surface Science*, 414(3):423–434, 1998.

[SHK$^+$09] C. Stadler, S. Hansen, I. Kröger, C. Kumpf, and E. Umbach. Tuning intermolecular interaction in long-range-ordered submonolayer organic films. *Nature Physics*, 5(2):153–158, 2009.

[SHS$^+$07] C. Stadler, S. Hansen, A. Schöll, T.-L. Lee, J. Zegenhagen, C. Kumpf, and E Umbach. Molecular distortion of NTCDA upon adsorption on Ag(111): a normal incidence x-ray standing wave study. *New Journal of Physics*, 9, 2007.

[SHS$^+$15] B. Stadtmüller, C. Henneke, S. Soubatch, F S. Tautz, and C. Kumpf. Tailoring metal-organic hybrid interfaces: heteromolecular structures with varying stoichiometry on Ag(111). *New Journal of Physics*, 17(2):023046, 2015.

[SKRK11] B. Stadtmüller, I. Kröger, F. Reinert, and C. Kumpf. Submonolayer growth of CuPc on noble metal surfaces. *Physical Review B*, 83:1–10, 2011.

[SKZ$^+$10] A. Schöll, L. Kilian, Y. Zou, J. Ziroff, S. Hame, F. Reinert, E. Umbach, and R. H. Fink. Disordering of an organic overlayer on a metal surface upon cooling. *Science (New York, N.Y.)*, 329:303–305, 2010.

[SLW$^+$14] B. Stadtmüller, D. Lüftner, M. Willenbockel, E. M. Reinisch, T. Sueyoshi, G. Koller, S. Soubatch, M. G. Ramsey, P. Puschnig, F. S. Tautz, and C. Kumpf. Unexpected interplay of bonding height and energy level alignment at heteromolecular hybrid interfaces. *Nature communications*, 5:3685, 2014.

[SPGE98] R. Strohmaier, J. Petersen, B. Gompf, and W. Eisenmenger. A systematic STM study of planar aromatic molecules on inorganic substrates. *Surface Science*, 418:91–104, 1998.

[SPL$^+$99] R. Schlaf, B. A. Parkinson, P. A. Lee, K. W. Nebesny, and N. R. Armstrong. HOMO/LUMO Alignment at PTCDA/ZnPc and PTCDA/ClInPc Heterointerfaces Determined by Combined UPS and XPS Measurements. *The Journal of Physical Chemistry B*, 103(15):2984–2992, 1999.

[SSB+14] B. Stadtmüller, S. Schröder, F. C. Bocquet, C. Henneke, C. Kleimann, S. Soubatch, M. Willenbockel, B. Detlefs, J. Zegenhagen, T.-L. Lee, F. S. Tautz, and C. Kumpf. Adsorption height alignment at heteromolecular hybrid interfaces. *Physical Review B*, 89:1614071–1614076, 2014.

[SSHT+01] F. Sellam, T. Schmitz-Hübsch, M. Toerker, S. Mannsfeld, H. Proehl, T. Fritz, K Leo, C Simpson, and K. Müllen. LEED and STM investigations of organic - organic heterostructures grown by molecular beam epitaxy. *Surface Science*, 478:113–121, 2001.

[SSK+12] B. Stadtmüller, T. Sueyoshi, G. Kichin, I. Kröger, S. Soubatch, R. Temirov, F. S. Tautz, and C. Kumpf. Commensurate registry and chemisorption at a hetero-organic interface. *Physical Review Letters*, 108:1–5, 2012.

[Sta02] J. Stanzel. *Untersuchung von NTCDA auf Ag(111) mit Hilfe der Absorption in stehenden Röntgenwellenfeldern.* Diploma thesis, Julius-Maximilian Universität Würzburg, 2002.

[Sta09] C. Stadler. *Strukturuntersuchungen organischer Monolagen auf Ag(111).* Ph.d. thesis, Julius-Maximilian-Universität Würzburg, 2009.

[Sta13] B. Stadtmüller. *Study of intermolecular interactions in hetero-organic thin films.* Ph.d. thesis, RWTH Aachen, 2013.

[SW71] M. E. Straumanis and C. L. Woodward. Lattice parameters and thermal expansion coefficients of Al, Ag and Mo at low temperatures. Comparison with dilatometric data. *Acta Crystallographica Section A*, 27(6):549–551, 1971.

[SWG+01] M. Stöhr, T. Wagner, M. Gabriel, B. Weyers, and R. Möller. Binary Molecular Layers of C 60 and Copper Phthalocyanine on Au (111): Self-Organized Nanostructuring. *Advanced Functional Materials*, 11(3):175–178, 2001.

[SWR+12] B. Stadtmüller, M. Willenbockel, E. M. Reinisch, T. Ules, F. C. Bocquet, S. Soubatch, P. Puschnig, G. Koller, M. G. Ramsey, F. S. Tautz, and C. Kumpf. Orbital tomography for highly symmetric adsorbate systems. *EPL*, 100(2):26008 p1–p6, 2012.

[SWS+15] B. Stadtmüller, M. Willenbockel, S. Schröder, C. Kleimann, E. M. Reinisch, T. Ules, B. Detlefs, S. Soubatch, P. Puschnig, J. Zegenhagen, M.G. Ramsey, F. S. Tautz, and C. Kumpf. Modification of the PTCDA-Ag (111) bond by the formation of a hetero-organic bilayer film with CuPc. *Phys. Rev. B*, 2015.

[SZS+04] A. Schöll, Y. Zou, T. Schmidt, R. Fink, and E. Umbach. High-Resolution Photoemission Study of Different NTCDA Monolayers on Ag(111): Bonding and Screening Influences on the Line Shapes. *J. Phys. Chem. B*, 108(38):14741–14748, 2004.

[Tau07] F. S. Tautz. Structure and bonding of large aromatic molecules on noble metal surfaces: The example of PTCDA. *Progress in Surface Science*, 82:479–520, 2007.

[TH85] J. Tersoff and D R Hamann. Theory of scanning tunneling microscopy. *Physical Review B*, 31(2), 1985.

[THS09] M. Ternes, A. J. Heinrich, and W.-D. Schneider. Spectroscopic manifestations of the Kondo effect on single adatoms. *Journal of Physics Condensed Matter*, 21, 2009.

[TV87] C. W. Tang and S. A. Vanslyke. Organic electroluminescent diodes. *Applied Physics Letters*, 51:913–915, 1987.

[USF96] E Umbach, M Sokolowski, and R Fink. Substrate-interaction, long-range order, and epitaxy of large organic adsorbates. *Applied Physics A*, 63:565–576, 1996.

[vHWC86] M. A. van Hove, W. H. Weinberg, and C.-M. Chan. *Low-energy electron diffraction, experiment, theory, and surface structure determination.* Springer Verlag, Berlin, Heidelberg, New York, London, Paris, Tokyo, 1986.

[Woo98] D. P. Woodruff. Normal X-Ray Standing Wave Determination of Adsorbate Structures. *Science*, 57:1–60, 1998.

[WSS+13] M. Willenbockel, B. Stadtmüller, K. Schönauer, F. C. Bocquet, D. Lüftner, E. M. Reinisch, T. Ules, G. Koller, C. Kumpf, S. Soubatch, P. Puschnig, M. G. Ramsey, and F. S. Tautz. Energy offsets within a molecular monolayer: the influence of the molecular environment. *New Journal of Physics*, 15(3), 2013.

[YHJ03] S. Yim, S. Heutz, and T. Jones. Influence of intermolecular interactions on the structure of phthalocyanine layers in molecular thin film heterostructures. *Physical Review B*, 67:1–8, 2003.

[YSF05] F. Yang, M. Shtein, and S. R. Forrest. Controlled growth of a molecular bulk heterojunction photovoltaic cell. *Nature Materials*, 4:37–41, 2005.

[Zeg93] J. Zegenhagen. Surface structure determination using x-ray standing waves. *Reports on Progress in Physics*, 18:199–271, 1993.

[ZHK+12] J. Ziroff, S. Hame, M. Kochler, A. Bendounan, A. Schöll, and F. Reinert. Low-energy scale excitations in the spectral function of organic monolayer systems. *Physical Review B*, 85(16):161404, 2012.

Acknowledgement

This work would not have been possible without the assistance and contribution of many people. I therefore would like to thank:

- my supervisor Prof. Christian Kumpf for stimulating discussions, his sense of humour and the warm, open and productive working atmosphere.
- Benjamin Stadtmüller for his help and patience in introducing me to all the relevant experimental and analysis tools. In each "emergency" Benjamin is the person of choice, even just for drinking a beer in Aachen.
- Caroline Henneke for scientific discussions, solving vacuum problems and for shortening our daily bus trips to Jülich by interesting conversations. I especially want to thank her for our superb shared holidays, her instigation of a "Stammtisch" in Aachen and the introduction to her wonderful friends, which made settling down in Aachen much smoother.
- my colleague and boyfriend Matthew Green for correcting all of the charming English errors in my thesis and for constantly spreading his good mood and his optimism around. In particular I thank him for his special Scottish wake-up program, including running to the train station and seeing the train doors close - luckily often from the right side.
- my master's student Markus Franke for his help in the lab during STM experiments and with all kind of LaTeX problems. He and Philipp Leinen always provided a warm and joyful working atmosphere in our office. I especially appreciated that they accepted a low room temperature and that they were willing to regularly open the window to let fresh air inside (in contrast to Norman Fournier).
- Dr. Sergey Subach, Simon Weiß, Dr. Francois Bocquet, Hannes Offenbacher, Georg Koller, Gerben van Straaten, Kathrin Schönauer and Martin Willenbockel for their support during many beamtimes at the Bessy II and Diamond Light source.
- Kathrin Schönauer, Sergey Subach and Taner Esat for supporting me during LT-STM/STS measurements. My special thanks goes to Taner who spent his whole weekend before Christmas assisting me.
- Dr. Tien-Lin Lee and Dave McCue for their great support during all beamtimes at the Diamond Light Source. In particular Tien-Lin who always appeared in less

than ten minutes at the beamline, even after emergency calls at three o‘clock in the night.

- Dr. Christoph Kleimann for introducing me to all information regarding the SPA-LEED chamber.
- Christa Elsässer for assisting me with room temperature STM experiments, and in particular for solving all kind of mechanical and electronic problems.
- Prof. Peter Puschnig and Daniel Lüftner from Graz University for supporting our ARPES measurements with theoretical maps enabling us to perform orbital tomography.
- Dr. Marcus Blab, Richard Spiegelberg and Dr. Stefan Korte for their assistance in solving all kind of electronic problems. I especially enjoyed our weekly meetings running around the Forschungszentrum, but less our exhausting trips to the top of the Sophienhöhe.
- Prof. Stefan Tautz for giving me the possibility to work in PGI-3.
- all members of the PGI-3 for the nice working atmosphere and Claudia Klamandt, the secretary of the ICS-7, who was always a great help.
- my parents Ute and Christian who have always been there for me in the form of Fitline products and Vitamin D tablets to aid me against the harmful radiation of the decommissioned nuclear reactor but most of all for helping me to realize my dreams.
- my sisters, Anja and Sarah, and their boyfriends, Thomas and Stefan, who always supported me in the last few years through exciting and wonderful trips and journeys and for welcoming me with open arms in Mannheim and Hamburg.

Band / Volume 130
High-Throughput Live-Cell Imaging for Investigations of Cellular Heterogeneity in *Corynebacterium glutamicum*
S. Helfrich (2016), xvi, 217 pp
ISBN: 978-3-95806-167-5

Band / Volume 131
Laser-Induced Ultrafast Electron- and Spin-Dynamics in the Electronic Band Structure of Co(001)
M. A. Plötzing (2016), ii, 109, XXXIV pp
ISBN: 978-3-95806-168-2

Band / Volume 132
Robot-Assisted Phenotyping of Genome-Reduced *Corynebacterium glutamicum* Strain Libraries to Draft a Chassis Organism
S. Unthan (2016), 122 pp
ISBN: 978-3-95806-169-9

Band / Volume 133
Characterization of amino acid ammonia lyases & aminomutases for the production of chiral α- and β-amino acids
A. Dreßen (2016), ix, 112 pp
ISBN: 978-3-95806-176-7

Band/Volume 134
7th Georgian-German School and Workshop in Basic Science
Kacharava, A. (Ed.) erscheint nur als CD (2016)
ISBN 978-3-95806-179-8

Band / Volume 135
Crystal growth and scattering studies on two ferrites
S. Adiga (2016), iv, 150 pp
ISBN: 978-3-95806-183-5

Band / Volume 136
Manipulating the Structural and Electronic Properties of Epitaxial $NaNbO_3$ Films via Strain and Stoichiometry
B. Cai (2016), VI, 114 pp
ISBN: 978-3-95806-185-9

Band / Volume 137
Surface Potential of Metallic Surfaces and Self-Assembling Organic Monolayers in Various Electrolytes
J. Wang (2016), ii, 58 pp
ISBN: 978-3-95806-188-0

Schriften des Forschungszentrums Jülich
Reihe Schlüsseltechnologien / Key Technologies

Band / Volume 138
Ab initio investigation of hybrid molecular-metallic interfaces as a tool to design surface magnetic properties for molecular spintronics
R. Friedrich (2016), 277 pp
ISBN: 978-3-95806-194-1

Band / Volume 139
Topological Matter - Topological Insulators, Skyrmions and Majoranas
Lecture Notes of the 48th IFF Spring School 2017
27 March – 07 April 2017, Jülich, Germany
ed. by S. Blügel, Y. Mokrousov, T. Schäpers, Y. Ando (2017), ca 1000 pp
ISBN: 978-3-95806-202-3

Band / Volume 140
In situ studies of the growth and oxidation of complex metal oxides by pulsed laser deposition
C. Xu (2017), iv, 159 pp
ISBN: 978-3-95806-204-7

Band / Volume 141
Intrinsic and extrinsic spin-orbit torques from first principles
G. Géranton (2017), 122 pp
ISBN: 978-3-95806-213-9

Band / Volume 142
Magnetic Proximity Effects in Nanoparticle Composite Systems and Macrocrystals
G. Wilbs (2017), III, 230 pp
ISBN: 978-3-95806-233-7

Band / Volume 143
Etablierung eines Systems aus Cysteinmutanten der Phosphoglycerat-Kinase für Entfaltungsstudien mit Einzelmolekül-FRET
A. Schöne (2017), 137 pp
ISBN: 978-3-95806-237-5

Band / Volume 144
Structural and electronic characterization of hetero-organic NTCDA-CuPc adsorbate systems on Ag(111)
S. Schröder (2017), vi, 154 pp
ISBN: 978-3-95806-239-9

Weitere ***Schriften des Verlags im Forschungszentrum Jülich*** unter
http://wwwzb1.fz-juelich.de/verlagextern1/index.asp

Schlüsseltechnologien /
Key Technologies
Band / Volume 144
ISBN 978-3-95806-239-9

JÜLICH
FORSCHUNGSZENTRUM